

Background Oriented Schlieren Technique for Flow Visualisation in Shock Tunnels

Thesis by

Dwishen Ramanah, B.E (Hons)

Submitted for the Degree of
Master of Philosophy

Centre for Hypersonics
The University of Queensland
St Lucia, Brisbane
AUSTRALIA

2007

(Submitted January 2007)

The degree is conferred when the thesis has been accepted by UQ Library

© 2007

Dwishen Ramanah, B.E (Hons)

All Rights Reserved

Statement of Originality

The work presented in this thesis is to the best of my knowledge and belief, original, except as acknowledged in the text. The material has not been submitted either in whole or in part, for a degree at this or any university.

Dwishen Ramanah

List of Publications

Journal Article

Ramanah, D., Raghunath, S., Mee, D. J., Roesgen, T. and Jacobs, P.A., “Background Oriented Schlieren for Flow Visualisation in Hypersonic Impulse Facilities,” *Shock Waves*, Vol.17, No.1-2, 2007, pp. 1-151.

Conference Papers

Ramanah, D., Mee, D.J. “Scramjet flow visualisation using Background Oriented Schlieren in hypersonic impulse facilities”, *14th AIAA/AHI Space Planes and Hypersonic Systems and Technologies Conference*, Canberra, Nov 2006, Paper AIAA-2006-8004.

McGilvray, M., Morgan, R., Jacobs, P., Ramanah, D. “Boundary Layer Transition in an Expansion Tube at a Low Enthalpy Operating Condition,” *45th AIAA Aerospace Sciences Meeting and Exhibit*, Reno, Jan 2007, Paper AIAA-2007-1328.

Abstract

The Background Oriented Schlieren (BOS) technique is a method that has been developed recently for easily and inexpensively visualizing density gradient variations in compressible flows. In this thesis, the applications of this technique in the Drummond tunnel and the T4 free-piston reflected shock tunnel are presented. The BOS technique was first tested in the Drummond tunnel then used during four test campaigns to qualitatively visualize the flow over scramjet models and components of scramjets in the T4 shock tunnel. The results demonstrate that a simple optical arrangement, that does not need high quality windows in the test section and model, can be used to detect the locations of shock waves, expansion fans and shear layers. At present, the resolution and quality of the images is not as high as can be achieved using conventional schlieren techniques.

Acknowledgements

I would like to extend my thanks to my supervisors, Associate Professor David Mee and Dr. Peter Jacobs for their guidance and support during this project.

I would also like to thank my fellow postgraduates and the Centre for Hypersonics staffs in particular to Mr. Katsuyoshi Tanimizu, Ms. Samantha Coras, Mr. James Turner for allowing me to test the BOS system during their experiments and to Mr. Sreekanth Raghunath and Mr. Dhananjay Gangurde for their help with the BOS experiments. Thanks also to Dr. Tim McIntyre for his guidance on optics and to Professor Thomas Rösger and Dr. Alex Liberzon at ETH, Zurich for their assistance with the BOS-processing algorithms.

I also express many thanks to my family in Mauritius and my friends in Australia for their endless support. I will never have achieved this without their encouragement.

This project was supported through an Australian Research Council Discovery Project Grant (DP0452374) and an External Support Enabling Grant and The University of Queensland Graduate School Research Travel Award.

Contents

Statement of Originality	iii
List of Publications	iv
Abstract	v
Acknowledgements	vi
List of Figures	xi
List of Tables	xvi
Nomenclature	xvii
1 Introduction	1
1.1 Motivation	1
1.1.1 Introducing the Background Oriented Schlieren	2
2 Flow Visualisation Techniques / Literature Survey	4
2.1 Introduction	4
2.2 Density Effects on Optics	5
2.2.1 The Gladstone-Dale Constant	5
2.3 Shadowgraphy	7
2.3.1 Shadowgraphy Applications	9
2.4 Schlieren Imaging	14
2.4.1 Schlieren Applications	15
2.5 Interferometry	18

2.5.1	Holographic Interferometry	18
2.6	Recent Imaging Technologies for Flow visualisation	22
2.6.1	BOS Principles	22
2.6.2	BOS experiments	24
3	PIV Evaluations and Background oriented Schlieren	27
3.1	Introduction	27
3.2	Particle Tracking Techniques (PIV, PTV, LSV)	28
3.3	Theory of the Background Oriented Schlieren	30
3.3.1	Estimating the shift between the flow off and flow on images due to vibration	31
3.3.2	Evaluating the displacement of the background pattern due to density gradients	33
3.3.2.1	Statistical analysis in PIV	34
3.3.2.2	The Fourier Domain	35
3.3.2.3	Correlation peak search	37
3.3.2.4	Gaussian peak-fit for sub-pixel accuracy	38
3.4	Schlieren-like image of the density field	41
3.4.1	Conclusion	41
4	Experimental Details	42
4.1	Introduction	42
4.2	The Drummond Shock tunnel	44
4.2.1	Models tested in the Drummond tunnel	46
4.2.2	Tunnel Instrumentation	47
4.3	T4 shock tunnel	48
4.3.1	Force Measurement on Scramjet model	48
4.3.2	Materials testing in the T4 Shock Tunnel	49
4.3.3	Flow inside a scramjet duct with leading edge fuel Injection	51
4.3.4	Visualizing the flow at the intake of a REST inlet	52
4.4	The BOS arrangement	53
4.4.1	The Background mask	53
4.4.2	Digital Image recording	55

4.4.3	The Background Illumination	57
5	Experimental Results	59
5.1	Introduction	59
5.2	The Drummond tunnel operations and tests conditions	61
5.3	Triggering the camera and strobe within the test time	64
5.3.1	Capturing a flow image for a shutter exposure of 1.0 ms	65
5.3.2	Capturing a flow image for a shutter exposure of 10 μ s	66
5.4	The BOS results in the Drummond tunnel	68
5.4.1	Visualizing the Flow over a 20° half angle sharp cone	68
5.4.2	Visualizing the flow over the Muses-C capsule	74
5.4.3	Visualizing the flow over the Muses-C capsule	79
5.5	The sensitivity of BOS for visualizing compressible flows	82
5.6	BOS results in the T4 shock tunnel	86
5.6.1	Using BOS to visualize a scramjet model intake	86
5.6.2	Material tests results in the T4 shock tunnel	92
5.6.3	Visualizing the flow in a scramjet duct	96
5.6.4	Visualizing the flow at the intake of a Mach 8 scramjet	101
5.6.5	Range of conditions for the BOS technique in T4	103
6	Conclusion and Recommendations	104
6.1	Conclusions	104
6.2	Recommendations	104
	Bibliography	106
A	Quantitative Evaluation of Density Fields using BOS	112
A.1	Introduction	112
A.2	Density Evaluation	113
A.2.1	Integrating with a Poisson solver	114
A.2.2	Finite Difference Approximation	115
B	Python Implementation of the BOS Algorithms	118
B.1	Introduction	118

B.2	The BOSGUI Program	119
B.2.1	The Numerical Python Package (NumPy)	119
B.2.2	The Python Imaging Library (PIL)	119
B.2.3	The <i>Estimate coarse shift</i> module	120
B.2.4	Evaluating vector displacements	122
B.2.5	The ' <i>simplepiv</i> ' module	122
B.2.6	The ' <i>slidesum</i> ' module	124
B.2.7	The ' <i>gausspeak</i> ' module	127
C	Acquiring the Images and Post-Processing using the BOSGUI Program	129
C.1	Introduction	129
C.2	Acquiring the Reference and Flow images	130
C.2.1	The Camera software settings	130
C.2.2	The Delay/Pulse Generator settings	133
C.2.3	The Reference Image	133
C.2.4	The Flow Image	134
C.3	Using the BOSGUI program	135
C.3.1	Estimating un-due disturbances between the reference and flow images	136
C.3.2	Evaluating the horizontal and vertical displacements due to density gradients	138
D	BOSQUI.py Code	141
E	makerounddotmask.m Code	153

List of Figures

2.1	Schematic of a shadowgraph system (Smits and Lim, 2000)	7
2.2	Deflection of light rays through glass (a) constant density field, (b) constant density gradient, (c) constant second derivative of density (d) variable second derivative of density (Merzkirch, 1987)	8
2.3	Shadowgraphs of bow shocks (a) Shadow formation by a bow shock (Smits, 2000) (b) Bow shock around a sphere in $M = 1.7$ flow (Merzkirch, 1974)	9
2.4	Shadowgraph arrangement attached to T4 shock tunnel (Gardner, 2000)	10
2.5	Sketch of model showing intake shock	10
2.6	Shadowgraph images at the intake (a) Combustion suppressed (fuel into nitrogen) (b) Fuel into air case (Gardner, 2000)	11
2.7	Shadowgraph images of the upstream section of the combustion chamber (a) with fuel but without combustion (b) with fuel and combustion (Gardner, 2000)	12
2.8	Boundary layer transition on a pencil model (Carlton, 1958)	13
2.9	Schematic view of a typical schlieren imaging system (Smits and Lim, 2000)	14
2.10	Horizontal knife-edge schlieren photograph of the flow field around a sphere at hypersonic speed (Merzkirch, 1987)	15
2.11	Schlieren setup (Lamar, 2001)	16
2.12	T-38 aircraft flying at Mach 1.1 (Weinstein et al., 1997)	17
2.13	Mach-Zehnder Interferometer (Smits and Lim, 2000)	18
2.14	Holographic interferograms (Wegener et al, 1996)	19
2.15	Holographic interferometry layout (McIntyre, 2005)	20
2.16	Flow left to right over flat plate (McIntyre, 2005)	20
2.17	Optical path for BOS measurement (Venkatakrisnan and Meier, 2004)	23
2.18	Joint work by NASA Ames & DLR to visualize vortex shedding of helicopter blades in hover flight (a) BOS image (b) Displacement field (Raffel et al, 1998)	25

2.19	Oblique shock wave on a cone-cylinder model at Mach 2.0 (Venkatakrisnan and Meier, 2004)	26
3.1	Flow chart of temperature calculation using BOS (Jensen, 2003)	30
3.2	Schematic of an oblique shock	32
3.3	Evaluation of the noise shifts from cross-correlation data	33
3.4	Conceptual arrangement for displacement vector estimate (Raffel et al, 1998)	34
3.5	Implementation of cross-correlation using fast Fourier transforms	36
3.6	The maximum correlation value on the correlation plane (open dot) and four surrounding correlation values (full dots) (Westerweel, 1993)	39
4.1	Diagram of the Drummond tunnel (Craddock, 1999)	44
4.2	Schematic x-t wave diagram showing the shock and expansion processes in the Drummond reflected shock tunnel (Craddock, 1999)	45
4.3	Models tested in the Drummond Tunnel	46
4.4	Schematic of the T4 shock tunnel prior to refurbishment in 2000	48
4.5	Scramjet CAD model showing forebody and cowls (CAD Image: Mr Katsuyoshi Tanimizu)	49
4.6	Flat plate mounted in T4 test section	50
4.7	SLS wedge to be mounted at trailing edge of the steel plate	50
4.8	Scramjet duct with one sidewall off to take a photo	51
4.9	Mach 8 scramjet engine on bench	52
4.10	Regions of the model where visualisation was used	52
4.11	The optical setup for BOS experiments	53
4.12	Matlab output of randomly distributed dots of size 0.3 mm	54
4.13	Negative image of Fig 4.10, printed on transparency	55
4.14	The Scorpion SCOR20S0 (Courtesy: Point Grey Research Inc.) Size: 50 mm X 50 mm X 40 mm Weight: 125 grams	56
4.15	Nikon 100-300 mm, f/5.6-32 Zoom lens	57
4.16	Xenon stroboscope	57
5.1	x-t plot calculated using L1d for a viscous simulation	61
5.2	Pressure change due to shock wave	62
5.3	The delay generator connections to the camera and light source	64
5.4	Timing of the trigger signals for a 1.0 ms shutter exposure or above	65
5.5	Timing of the trigger signals for a 10 μ s shutter exposure	67

5.6	Cone model in the Drummond Tunnel test section, camera-560 mm away from test section with background pattern on the tunnel window	68
5.7	Absolute difference between the reference and corrected flow image	69
5.8	Arrows showing density gradient vectors for a search window size = 32 x32 and step size = 4 pixels	70
5.9	Arrows showing density gradient vectors for a search window size = 32 x 32 and step size = 16 pixels	71
5.10	Histogram showing the distribution of the horizontal displacement vectors	71
5.11	Histogram showing the distribution of the vertical displacement vectors	72
5.12	Vertical knife-edge, window size = 32 x 32, step size = 4 pixels	73
5.13	Horizontal knife-edge, window size = 32 x 32, step size = 4 pixels	74
5.14	Muses-C model mounted in the Drummond test section, camera-560 mm away from test section, background pattern attached to tunnel window	75
5.15	Absolute difference image between the reference and the corrected flow image	75
5.16	Density gradient vectors obtained with a correlation window size of 32 pixels and a step size of 12 pixels	76
5.17	Density gradient vectors obtained with a correlation window size of 32 pixels and step size of 4 pixels	76
5.18	Vertical knife-edge generated using vectors from a cross-correlation window size of 32 x 32 pixels and a step size of 4 pixels	77
5.19	Horizontal knife-edge generated using vectors from a cross-correlation window size of 32 x 32 pixels and a step size of 4 pixels	78
5.20	Cropped portion of the Muses-C flow image showing thin saturated layer	78
5.21	Sphere-cone mounted in the Drummond test section	79
5.22	Absolute difference between reference and flow image	80
5.23	Density gradient vectors in the bow shock layer, window size 36 x 36 and step size 4 pixels	80
5.24	Vertical knife edge schlieren	81
5.25	Horizontal knife edge schlieren	81
5.26	Optical path of a light beam through a constant density gradient region	83
5.27	Increased sensitivity of the BOS system	84
5.28	Increased sensitivity of the BOS system	85

5.29	Light source placed on one side of the tunnel and mounted on the optics table	87
5.30	The camera and lens mounted on the optic table next to T4 opposite to the light source	87
5.31	Scramjet Model shot 8768, $p_s = 33.8$ MPa, $h_s = 2.54$ MJ/kg, $M_\infty = 8.3$, $p_\infty = 2.1$ kPa, $U_\infty = 2.2$ km/s, $T_\infty = 173$ K	88
5.32	Drag data and TTL to trigger camera	88
5.33	Shot 8772, $p_s = 31.7$ MPa, $h_s = 6.0$ MJ/kg, $M_\infty = 7.2$, $p_\infty = 2.9$ kPa, $U_\infty = 3.2$ km/s, $T_\infty = 505$ K	89
5.34	Shot 8776, $p_s = 18.7$ MPa, $h_s = 7.9$ MJ/kg, $M_\infty = 6.8$, $p_\infty = 1.9$ kPa, $U_\infty = 3.6$ km/s, $T_\infty = 707$ K	90
5.35	BOS system focussed at the intake region of the scaled scramjet model	90
5.36	Horizontal knife-edge schlieren image	91
5.37	Shot 8770, $p_s = 36.9$ MPa, $h_s = 2.6$ MJ/kg, $M_\infty = 8.2$, $p_\infty = 2.36$ kPa, $U_\infty = 2.2$ km/s, $T_\infty = 180$ K, shutter exposure = 1.0 ms	92
5.38	Shot 9058, flat plate at 0° AOA, $p_s = 21.7$ MPa, $h_s = 4.0$ MJ/kg, $M_\infty = 7.2$, $p_\infty = 2.3$ kPa, $U_\infty = 2.6$ km/s, $T_\infty = 348$ K, shutter exposure = 40 μ s	92
5.39	Gradient vector image, shot 9058, search window size = 16 x 16 pixels, step size = 4 pixels	93
5.40	Horizontal knife-edge schlieren	93
5.41	Vertical knife-edge schlieren	94
5.42	Shot 9057, flat plate at 10° AOA, $p_s = 21.9$ MPa, $h_s = 3.5$ MJ/kg, $M_\infty = 6.7$, $p_\infty = 4.0$ kPa, $U_\infty = 2.5$ km/s, $T_\infty = 351$ K, shutter exposure = 1.07 ms	95
5.43	Density gradient vectors obtained using a cross-correlation window size of 32 x 32 pixels and a search size of 4 pixels	95
5.44	Horizontal knife-edge schlieren image	96
5.45	Shot 9066, $p_s = 42$ MPa, $h_s = 3.4$ MJ/kg, $M_\infty = 7.9$, $p_\infty = 3.0$ kPa, $U_\infty = 2.5$ km/s, $T_\infty = 255$ K, shutter exposure = 40 μ s	97
5.46	Horizontal knife- edge BOS image	97
5.47	Shot 9086, $p_s = 26.9$ MPa, $h_s = 3.8$ MJ/kg, $M_\infty = 7.4$, $p_\infty = 2.5$ kPa, $U_\infty = 2.6$ km/s, $T_\infty = 320$ K, shutter exposure = 30 μ s	98
5.48	Horizontal knife-edge BOS image, shot 9086	98

5.49	Flow Hologram, shot 9167, $p_s = 30.7$ MPa, $h_s = 4.3$ MJ/kg, $M_\infty = 7.3$, $p_\infty = 2.6$ kPa, $U_\infty = 2.8$ km/s, $T_\infty = 363$ K	99
5.50	Fuel into N ₂ , injected at the leading edge, shot 9085, $p_s = 27.4$ MPa, $h_s = 3.8$ MJ/kg, $M_\infty = 7.5$, $p_\infty = 2.4$ kPa, $T_\infty = 313$ K, shutter exposure = 30 μ s	100
5.51	Shot 9077 flow image, fuel injected in air at leading edge, $p_s = 21.5$ MPa, $h_s = 3.3$ MJ/kg, $M_\infty = 7.7$, $p_\infty = 1.8$ kPa, $T_\infty = 254.4$ K, shutter exposure = 40 μ s	101
5.52	Vertical knife edge schlieren, s9214	101
5.53	Vertical knife-edge schlieren, s9219, $p_s = 13.5$ MPa, $h_s = 3.1$ MJ/kg, $M_\infty = 6.6$, $p_\infty = 3.5$ kPa, $T_\infty = 318$ K, $U_\infty = 2.4$ km/s, shutter exposure = 10 μ s	102
5.54	Vertical knife-edge schlieren, s9223. , $p_s = 13.7$ MPa, $h_s = 2.34$ MJ/kg, $M_\infty = 7.0$, $p_\infty = 3.4$ kPa, $T_\infty = 215$ K, $U_\infty = 2.1$ km/s, shutter exposure = 10 μ s	102
B.1	Assigning values according to the pixel intensities (Jain, 1989)	120
B.2	Surface plot of the correlation map	121
B.3	Setting the boundaries for the correlation procedure	124
C.1	Format and frame rate settings	130
C.2	Switching ON the external trigger mode	131
C.3	Brightness, Exposure and Shutter exposure settings	132
C.4	Register <i>614H</i> settings	133
C.5	The BOS image processing program main menu	135
C.6	Cone model in the Drummond Tunnel test section	136
C.7	The required actions to process the two images	136
C.8	Choosing a sample box window outside a undisturbed region	137
C.9	Absolute difference image between the reference and corrected flow images	137
C.10	Plot of the vector displacement for an interrogation window size of 32 pixels and step size 12 pixels	138
C.11	Histogram representing the distribution of vertical displacement vectors	139
C.12	Horizontal knife-edge schlieren	139
C.13	Vertical knife-edge schlieren	140
C.14	Colour Schlieren Image	140

List of Tables

2.1	Gladstone-Dale constants for different gases (Merzkirch, 1987)	6
5.1	Stagnation condition at the end of the shock tube	63
5.2	Free-stream conditions at nozzle exit plane	63
5.3	Average vector values in the selected region	85
5.4	T4 test conditions and shutter times for the BOS technique	103

Nomenclature

a	: sample window in reference image for PIV cross correlation
A	: region of a BOS reference image where no disturbance is expected to occur
b	: sample window in flow image for PIV cross correlation
B	: region of a BOS flow image where density variation is expected to occur
c	: speed of light (m/s)
C	: width of correlation window for shift detection (pixels)
c_o	: speed of light in a vacuum (m/s)
d	: displacement estimate (pixels)
d^*	: size of light source
D	: height of correlation window for shift detection (pixels)
e	: electric charge (C)
E	: electric field strength (NC ⁻¹)
F	: constant for Gaussian peak fit curve
f_1	: lens 1 focal length (m)
f_i	: oscillator strength
h	: enthalpy (J/kg)
I	: light intensity
l	: distance of the observation plane from an optical disturbance region
L	: Loschmidt number
m^*	: molecular weight (kg)
m	: mass (kg)
M	: width of correlation window (pixels)
M	: Mach number
n	: index of refraction
N	: height of correlation window (pixels)
N^*	: molecular number density (m ⁻³)

p	: pressure (Pa)
p^*	: dipole moment (Cm)
Q	: constant for Gaussian peak fit curve
R	: radius of cone (m)
t	: time (s)
T	: temperature (K)
u	: horizontal displacement vector
U	: velocity (m/s)
v	: vertical displacement vector
W	: density gradient region or optical path length
x	: Distance in the horizontal direction on image plane (m)
y	: Distance in the vertical direction on image plane (m)
Z_B	: Distance between camera lens and background plane (m)
Z_D	: Distance between background plane and density gradient region (m)
Z_i	: Distance between camera lens and image plane (m)

Greek

α	: electronic polarizability ($C \cdot m^2 \cdot V^{-1}$)
δ	: shock stand-off distance (m)
ε	: angle of deflection of a light ray (rad)
γ	: integration limits in equation 2.9
ρ	: density ($kg \cdot m^{-3}$)
K	: Gladstone-Dale constant
λ	: wavelength of light (m)
Λ	: Sinc function sample rate
ν	: frequency of an electric field strength (Hz)
ν_i	: resonant frequency (Hz)
Φ	: interferogram phase

Subscripts and Superscripts

∞	: free-stream condition
e	: electron

<i>int</i>	: interpolated
<i>p</i>	: peak
<i>s</i>	: nozzle-supply condition
<i>sh</i>	: shifted
<i>T</i>	: transpose

Abbreviations

A/D	: Analog to Digital
AOA	: Angle of Attack
bpp	: bits per pixel
BOS	: Background Oriented Schlieren
CAD	: Computer Aided Design
CCD	: Charged-Coupled Devices
CFD	: Computational Fluid Dynamics
<i>corr</i>	: correlation coefficient
<i>Cov</i>	: Covariance
<i>DFT</i>	: Direct Fourier Transform
<i>DFT⁻¹</i>	: Inverse Fourier Transform
ESTC:	: Equilibrium Shock Tube Condition Code
ETH	: Eidgenoessische Technische Hochschule (The Swiss Federal Institute of Technology)
F-18	: Boeing F/A 18 Hornet strike fighter jet
FFT	: Fast Fourier Transform
L1D	: Lagrangian one-Dimensional
LSV	: Laser Speckle Velocimetry
Mb_cns	: Multi-block cell-centred navier stokes code
Nd:YAG	: Neodymium-Doped Yttrium Aluminium Garnet
NENZF	: Non-Equilibrium Nozzle Flow code
NumPy	: Numerical Python package
PIL	: Python Imaging Library
PIV	: Particle Image Velocimetry
PTV	: Particle Tracking Velocimetry

PLIF	: Planar Laser Induced Fluorescence
REST	: Rectangular-to-Elliptical Shape Transition
SR-71	: Lockheed Martin reconnaissance aircraft (Blackbird)
TFG	: Thin Film Gauge
TTL	: Transistor-transistor Logic
T4	: T4 shock tunnel
T-38	: Northrop Grumman Talon Supersonic Jet
UQ	: University of Queensland
UPWT	: Langley Unitary Plan Wind Tunnel
<i>Var</i>	: Variance
X1	: X1 expansion tube
X2	: X2 expansion tube
X3	: X3 expansion tube
2-D	: two-dimensional

This thesis is dedicated to my family who resides in Mauritius

“Everything should be made as simple as possible, but not simpler.”

Albert Einstein (March 14, 1879 – April 12, 1955)

CHAPTER 1

Introduction

1.1 Motivation

In Fluid Mechanics, it is critically important to see the patterns produced by flowing fluids, in order to understand them. Most fluids, such as air and water are transparent. Thus their flow patterns are invisible to us without some special methods to make them visible.

Flow visualisation is the art of making these patterns visible. In experimental fluid dynamics, flows are visualised by three methods: surface flow visualisation, particle tracer methods, and optical methods. Surface flow visualisation reveals the flow streamlines as the solid surface is approached. Colored oil applied to the surface of a wind tunnel model is one example of this technique. The oil responds to the surface shear stress and forms a pattern. Particles, such as smoke, can be added to a flow to trace the fluid motion. We can illuminate the particles with a sheet of laser light in order to visualise a slice of a complicated fluid flow pattern. Assuming that the particles faithfully follow the streamlines of the flow, we cannot only visualise the flow but also measure its velocity using a method known as particle image velocimetry. Finally, some flows reveal their patterns by way of changes in their optical refractive index. These are visualised by optical methods known as the shadowgraph, schlieren, interferometry and more recently, the Background Oriented Schlieren (BOS) technique.

The aim of this thesis is to develop the BOS visualisation technique for use in hypersonics impulse facilities using a simple optical setup. Recently developed digital cameras capable of capturing images at small shutter times will be used. These cameras suit the economic regime of research undertaken within the hypersonics group at The University of Queensland (UQ). The BOS system was recently applied for the first time to a small-reflected shock tunnel (Raghunath et al., 2005). The primary goal of the present study is to see if the technique could be useful for visualizing flows typical of

scramjet conditions in the large T4 free-piston reflected shock tunnel (Stalker and Morgan, 1988) and to determine the range of conditions at which the technique can be implemented. One of the main differences between the previous small shock tunnel tests and the T4 tests is the potential for significant flow luminosity in the higher enthalpy facility.

It is sometimes important to probe the flow using visualisation systems in a scramjet duct to confirm the locations of shock waves, expansion fans, shear layers and to seek evidence of combustion or to determine the flow properties. The flow luminosity due to the combustion can be overcome using optical filters and laser illumination. The use of such a system can however lead to a complex setup of lenses and mirrors.

Another disadvantage of laser based photography techniques in shock tunnels is the requirement for optical quality glass. This glass type is needed for both the test section of the tunnel and the windows at the sides of the model if the flow inside a model is to be visualised. The rupture of the diaphragm in a shock tunnel can result in small fragments of diaphragm material sweeping past the model in the test section. This can lead to damage of the glass in the windows in the model and tunnel sidewalls and they must be replaced. The BOS technique does not require a complex optical setup and high quality windows.

1.1.1 Introducing the Background Oriented Schlieren technique

The Background Oriented Schlieren (BOS) system is a simple and effective flow visualisation technique that has been applied to flow visualisation in a range of applications (Richard and Raffel, 2001; Meier, 2002; Klinge et al., 2003; Venkatakrishnan and Meier, 2004). A BOS system uses a digital camera to record two images of a pattern located behind the flow of interest. One photograph is taken when there is no flow and another with flow. The differences between the images are used to infer differences in the refractive index of the medium between the camera and the pattern. The system requires only a light source, a background pattern, a camera and windows in the test section and a model. The windows do not necessarily have to be of high optical quality since only the differences between two images are needed to infer the refractive index variations. While the optical arrangement is much simpler in a BOS system than in a conventional schlieren system, the complexity of the processing of the

images is increased. Developments of image analysis made in the field of particle image velocimetry are used in this thesis to analyse the images.

Flow Visualisation Techniques / Literature Survey

2.1 Introduction

This chapter is divided into five sections. In the first section, a brief review of how gas densities and other associated variables affect the optical light path is presented. The second and third sections outline the application of the two most commonly used visualisation tools, shadowgraphy and schlieren. These sections also explain how these imaging techniques can be adapted to visualise qualitatively and, in some cases, quantitatively regions of varying density.

The fourth section comprises of a brief overview of the interferometry visualisation and holographic interferometry techniques as applied to the Centre's shock and expansion tunnels. This is a laser-based measurement technique that can be used for a range of high temperature and/or high velocity flow environments. This technique has been used to obtain two-dimensional images of the flow through the scramjet duct in the T4 reflected shock tunnel. The holographic interferometry technique is also used to measure density and visualise flows around re-entry bodies and hypervelocity vehicles in UQ's free piston driven expansion tubes. An overview of the results achieved in those facilities is presented.

The last section of this chapter briefly describes the theory behind the recently developed technique for flow visualisation, Background Oriented Schlieren (BOS). Various aerodynamics research laboratories have implemented this technique because of its simple arrangement. This section will review some BOS experiments. A theoretical background of this technique is given in Chapter 3.

2.2 Effects of regions of varying density gradients on optics

2.2 Effects of regions of varying density on optics

The shadowgraphic, schlieren and interferometric visualisation techniques are based on the fact that the speed of light is different in regions of different density. The speed of light is at its maximum when it passes through a vacuum. The index of refraction, n , of a medium is defined as the ratio of the speed of light in a vacuum, c_o , to that in the medium, c , as

$$n = \frac{c_o}{c} . \quad (2.1)$$

Different visualisation techniques respond to either the level of the refractive index, the refractive index gradient or the second derivative of the refractive index.

Large and rapid changes of density can occur in compressible flows. Rays of light passing through regions of changing density are refracted by the inhomogeneous distribution of the refractive index in that region in two ways. Firstly, the light is deflected from its original path and, secondly, the phase of the disturbed light wave is shifted relative to that of an undisturbed light ray. These phenomena can be used to visualise the flow field qualitatively and to perform quantitative density measurements. For this, an exact knowledge of the relation between density and refractive index is important and is discussed next.

2.2.1 The Gladstone-Dale constant

The Gladstone Dale constant (Merzkirch 1987; Goldstein 1983) can be used to relate the refractive index of a medium to its density. This constant depends on the characteristics of the gas in the medium and weakly on the frequency of light used. The Gladstone-Dale equation is derived using the electromagnetic theory and is expressed as

$$n - 1 = K \rho . \quad (2.2)$$

where K is the Gladstone Dale constant and ρ , the density of the medium. The Gladstone-dale constants for various gases are given in Table 2.1.

Gas	K (cm ³ /g)	Wavelength λ (μm)	Temperature T (K)
He	0.196	0.633	295
Ne	0.075	0.633	295
Ar	0.157	0.633	295
Kr	0.115	0.633	295
Xe	0.119	0.633	295
H ₂	1.550	0.633	273
O ₂	0.190	0.589	273
N ₂	0.238	0.589	273
CO ₂	0.229	0.589	273
NO	0.221	0.633	295
H ₂ O	0.310	0.633	273
CF ₄	0.122	0.633	302
CH ₄	0.617	0.633	295
SF ₆	0.113	0.633	295

Table 2.1. Gladstone-Dale constants for different gases (Merzkirch, 1987).

2.3 Shadowgraphy

The shadowgraphic visualisation technique is one of the simplest methods to investigate flows with varying density. Dvroak, a co-worker of Ernst Mach, analysed this tool in the 1880's. Fig. 2.1 shows a typical arrangement of such a system. A simple shadowgraphy system can be implemented using parallel light rays. The light rays are passed through the test field under investigation and the shadow produced on a vertical image plane is recorded. The sharpness of the image depends upon the size of the light source. The light source has to be small in order not to produce a blurred image.

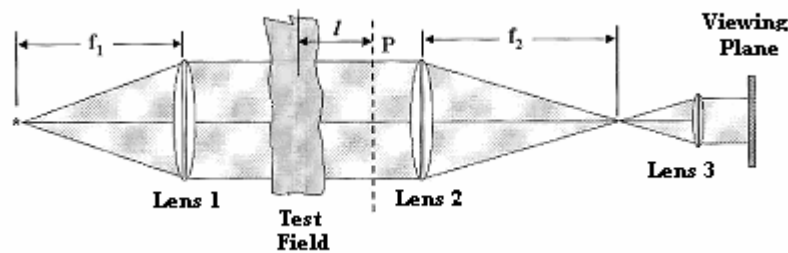


Fig. 2.1. Schematic of a shadowgraph system (Smits and Lim, 2000).

The blur in the image is given by $\frac{\ell d^*}{f_1}$, where f_1 is the lens or mirror focal length, d^* is the size of the source, and ℓ is the distance of the observation plane from the optical disturbance region (Smits and Lim, 2000). A second spherical lens (lens 2 shown in Fig. 2.1) and lens 3 are used to reduce the size of the image, a configuration, which is used in most laboratory wind tunnels. Lenses 2 and 3 are not required for large-scale visualisation, but a much larger photographic plate would be required in its absence because the image would then be full scale.

When passing through the test field, the individual light rays are refracted and bent away from their original path. Merzkirch (1987) provides an analogy of refraction of light rays in density-stratified regions by using a transparent plate of homogeneous material. In this experiment, Merzkirch (1987) used glass plates of different geometries but of constant thickness. This analogy of deflection of light rays was done to determine to which density field shadowgraphy would be sensitive. In order to derive visible information about the flow, the light ray should get refracted in such a way that, on the image plane, regions of varying light intensity could be identified. These regions would

be characterized by a non-uniform illumination. The four cases analysed to determine which density field would cause such non-uniformity were:

(a) A field of constant density – The beam was unaffected thus the recording plane was uniformly illuminated. (Fig. 2.2a).

(b) A fluid field with $\frac{\partial n}{\partial y} = const$ – A glass wedge with plane surfaces. (Fig. 2.2b).

The recording plane was uniformly illuminated.

(c) A fluid field with $\frac{\partial^2 n}{\partial y^2} = const$ – A spherical or cylindrical face wedge. (Fig. 2.2c). The illumination was less bright but still uniform.

(d) A fluid field with $\frac{\partial^2 n}{\partial y^2} \neq const$ – A curved surface wedge. (Fig. 2.2d). The

illumination on the recording plane was non-uniform. Hence regions of shades of grey can be identified and flow information could be derived.

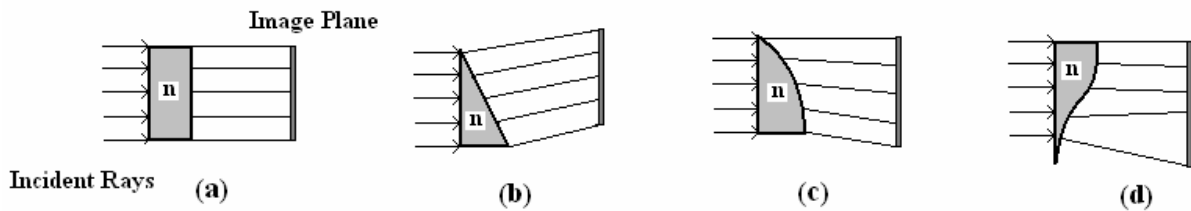


Fig. 2.2. Deflection of light rays through glass (a) constant density field, (b) constant density gradient, (c) constant second derivative of density (d) variable second derivative of density (Merzkirch, 1987).

Shadowgraphy is not suitable for quantitative measurement due to the fact that one needs to perform a double integration of the intensity distribution in the image plane to derive density data. This intensity distribution expressed in grey shades usually cannot be evaluated precisely enough for the amplified errors introduced by the double integration to be small.

Fig. 2.3(a) illustrates the non-uniform light pattern observed on the image plane through a bow shock. As the light waves traverse the curved bow shock, they are deflected from their original paths and curve towards the denser flow region downstream of the shock wave. This causes the formation of dark bands on the observation plane.

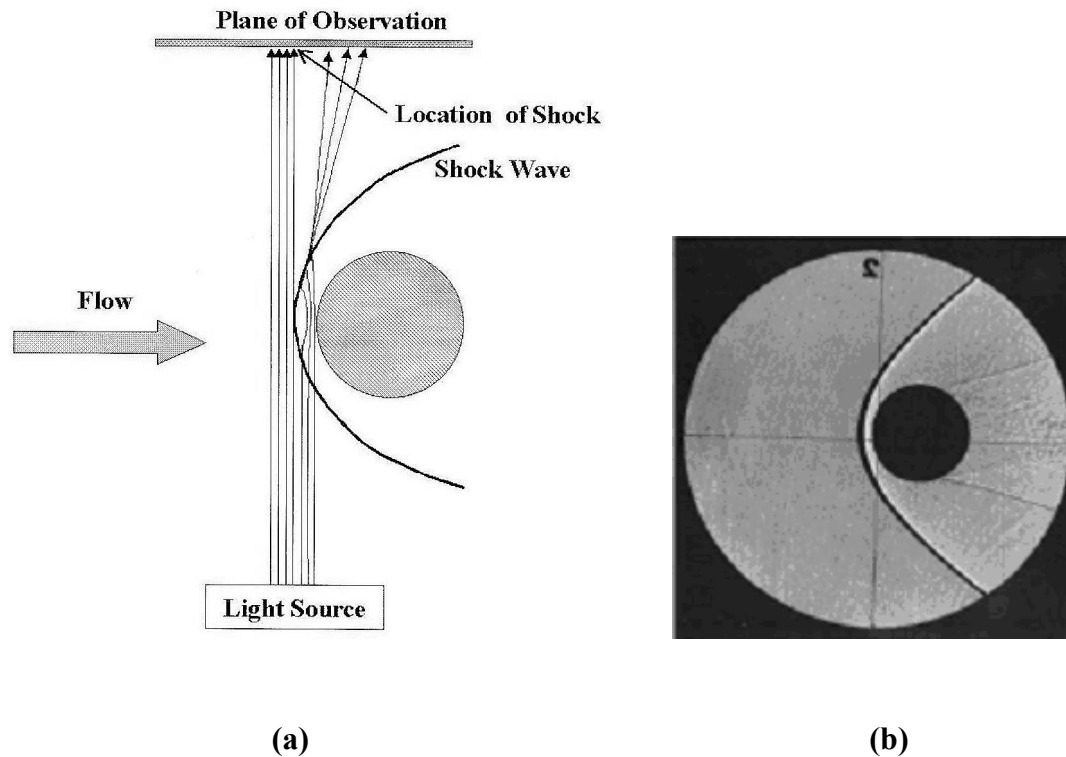


Fig. 2.3. Shadowgraphs of bow shocks (a) Shadow formation by a bow shock (Smits and Lim, 2000) (b) Bow shock around a sphere in $M = 1.7$ flow (Merzkirch, 1987).

However, shadowgraphy is suitable for an immediate investigation of flow fields with varying density. A few shadowgraphy experiments for boundary layer and shockwave visualisation are discussed next.

2.3.1 Shadowgraphy applications

In this section, a synopsis of two shadowgraph experiments is given. Firstly, the shadowgraphy system was used to provide evidence of combustion in a supersonic ramjet (scramjet) engine and secondly, an experiment to detect the transition from laminar to turbulent flow within the boundary layer on a pencil model is discussed.

Gardner (2000) developed a shadowgraphy system during his master of engineering thesis work at The University of Queensland. The system consisted of a single pass arrangement as shown in Fig 2.4, and was used to analyze the flow at the intake of a 2-D scramjet model in the T4 shock tunnel. The scramjet intake and combustion chamber were fitted with 10 mm float glass sidewalls and a 250 μ s pulse from a ruby laser (694 nm) illuminated the flow. The laser system was set up first to visualise the intake and secondly to visualise the combustion chamber. The overall aim of the experiment was to

investigate the reduction of viscous drag by shortening the length of the combustion chamber of a scramjet engine. For this, fuel was injected through portholes on the intake upstream of the combustion chamber. This would allow the fuel to mix upstream of the combustor.

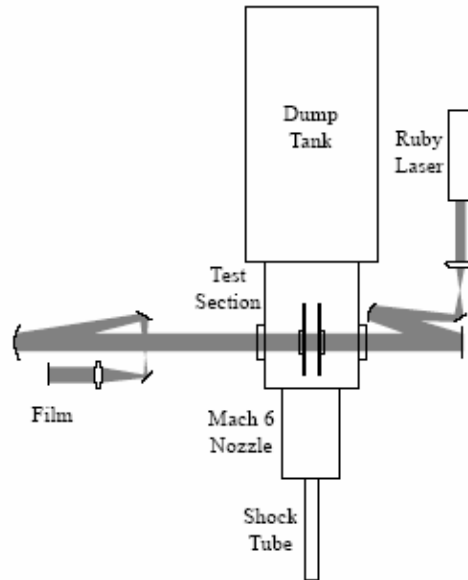


Fig. 2.4. Shadowgraph arrangement attached to T4 shock tunnel (Gardner, 2000).

The shadowgraph technique was used to identify the locations of shock waves in the intake and to estimate the Mach number for combustion and no-combustion cases. A sketch of the model showing the intake shock is illustrated in Fig 2.5.

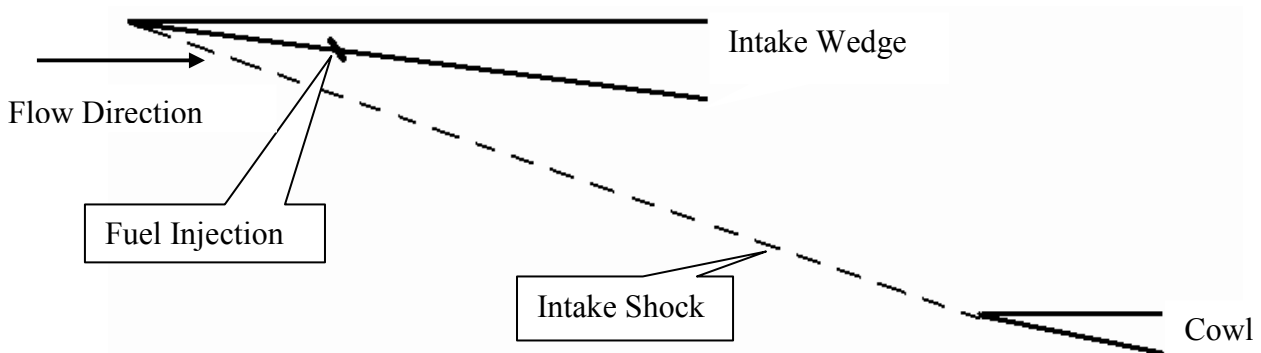


Fig. 2.5. Sketch of model showing intake shock.

The shadowgraph images did not show evidence of combustion occurring in the intake of the scramjet model. The shock angles were identical for two cases where combustion was suppressed by injecting fuel into nitrogen (Fig 2.6a) and fuel into air (Fig 2.6b).

2.3 Shadowgraphy

The shadowgraphs also indicated that the combustion chamber remained unchoked for both cases. This information was used to confirm that the inlet injection did not lead to choking at that condition.

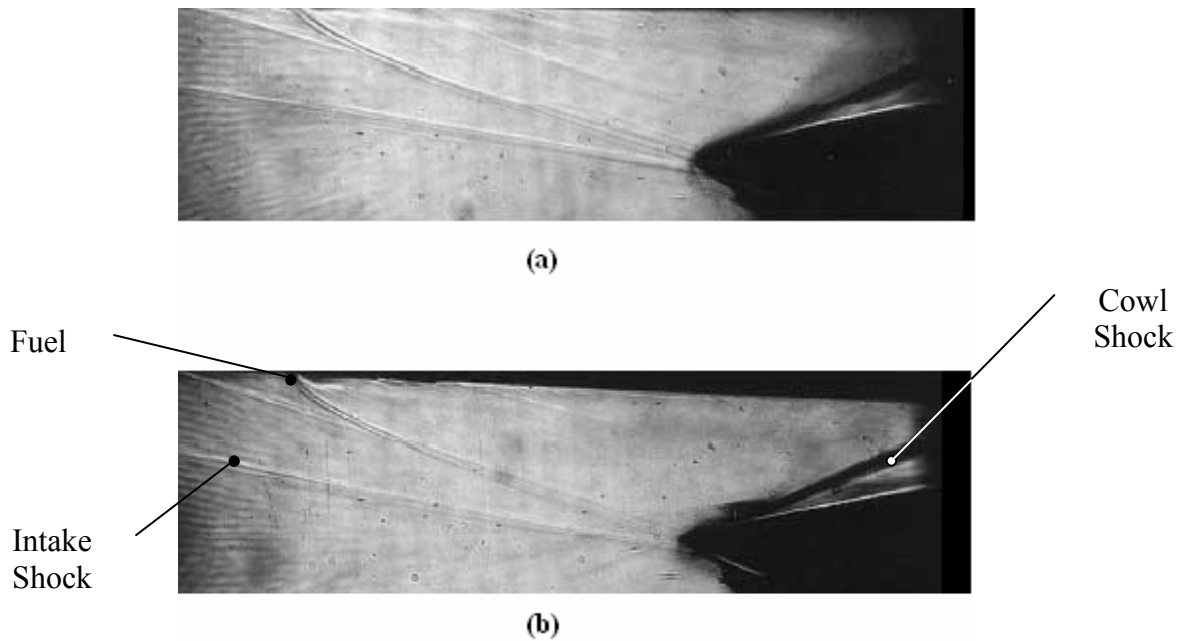


Fig. 2.6. Shadowgraph images at the intake (a) Combustion suppressed (fuel into nitrogen) (b) Fuel into air case (Gardner, 2000).

The next step in the experimental program was to determine whether combustion occurred in the combustion chamber. For this, the shadowgraph system was set up to visualise the flow in the combustion chamber of the model. Evidence of combustion occurring in the burner was identified by analysis of the shadowgraphy images. Differences in shock positions, as illustrated in Fig 2.7, were observed and were attributed to a change in Mach number due to heat release associated with the combustion of the fuel. Shadowgraphy was shown to be a useful tool for the scramjet flow analysis but the extraction of quantitative density information was not attempted.



(a)



(b)

Fig. 2.7. Shadowgraph images of the upstream section of the combustion chamber (a) with fuel but without combustion (b) with fuel and combustion (Gardner, 2000).

Carlton (1958) used a conventional shadowgraphic visualisation system to demonstrate the formation, spread and turbulent burst geometry of spots in a transitional boundary layer on a pencil model at Mach 2.2. Light reflecting from a collimated mirror was passed through the tunnel windows and allowed to fall on a photographic plate.

The study was made using spark shadowgraphs of small gun-launched models in free flight through still air and through a countercurrent supersonic air stream. Three techniques were employed to assess the accuracy of the burst profiles. Direct measurement using a drafting scale with the aid of a magnifying glass was first used to try to retrieve information from the shadowgraph negatives. The second technique was to magnify the negatives about eight times to obtain images such as the burst profile image shown in Fig. 2.8. The third variation involved accounting for the effects of diffraction and refraction by noting the difference between the apparent body diameter and the known body diameter. The body axis is located on the shadowgraph from symmetry. Measurements were then made from the axis to the outer profile of the burst and the true body radius was subtracted. It was anticipated that this method would be most accurate. However, large differences in the amount of refraction occurring in the boundary layers of the bodies of different diameter were found.

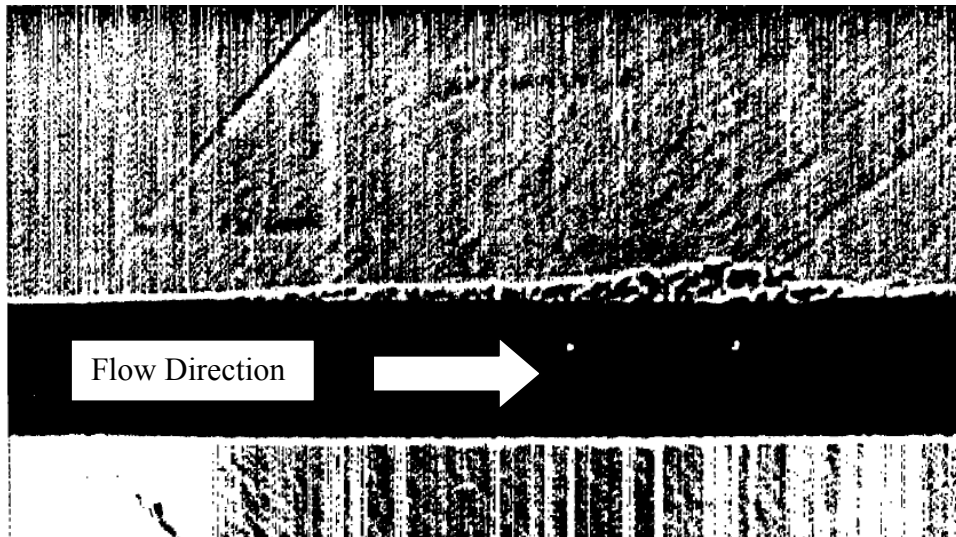


Fig. 2.8. Boundary layer transition on a pencil model (Carlton, 1958).

On the pencil model however, the correction to the apparent body radius was almost equal to the width of the diffraction fringe and appeared to be comparable with the visible portion of the burst.

This experiment showed the appropriateness of shadowgraphy to visualise a boundary layer growth. A quantitative approach was not adopted in this experiment.

2.4 Schlieren Imaging

Schlieren imaging is only possible if gradients or boundaries across which the density changes are present in the flow. The gradients deflect the paths of light rays passing in the vicinity of or through these gradients (Settles, 2001). The implementation of a schlieren technique was originally described by Teopler in 1864 and recent reviews are given by Merzkirch (1987) and Settles (2001). One principal limitation is the field size, which is set by the diameter of the optical field elements used. Also, schlieren techniques usually give only a qualitative visualisation of the density variation in the flow.

Similar to shadowgraphy, a simple schlieren system can be setup by using parallel-collimated light beam that is passed through the flow field. The technique essentially consists of a point light source, either a laser or spark with a circular or slit aperture that is placed at the focal point of lens 1 (Fig. 2.9). The collimated light passes through the test region and lens 2 (Fig 2.9) focuses the light on the image plane. A knife-edge is located at the focal plane of lens 2 and is positioned to cut off part of the light as seen on the image plane, hence the intensity of light illuminating the photographic plate will be reduced. The light going through a region of disturbance will be deflected by angle ε , and the shifted distance Δs , which is perpendicular to the knife-edge, is given by

$$\Delta s = f_2 \tan \varepsilon , \quad (2.8)$$

where f_2 is the focal length of lens 2. Merzkirch (1987) shows that the relative intensity change at the image plane can be written as

$$\frac{\Delta I}{I} = \frac{Kf_2}{s} \int_{y_1}^{y_2} \frac{1}{n} \frac{\partial n}{\partial y} dz , \quad (2.9)$$

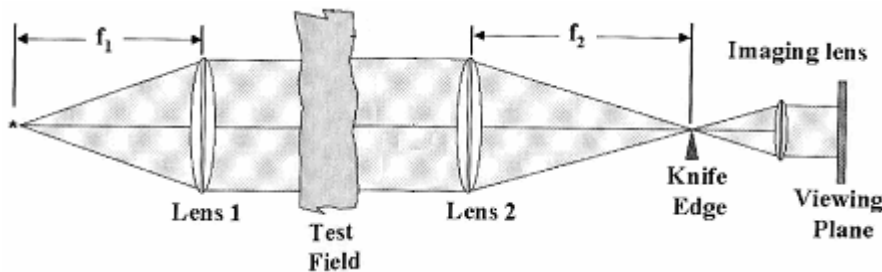


Fig. 2.9. Schematic view of a typical schlieren imaging system (Smits and Lim, 2000).

where γ_1 and γ_2 are the z coordinates at which the light ray enters and leaves the test region and s is the reduced height of the light source image. The contrast on the photographic film increases as the ratio $(\frac{s}{f_2})$ decreases.

There have been several attempts at extracting quantitative information from schlieren images. One simple technique involves analysing schlieren curves of equal photographic density. This technique, known as an isodensity tracer technique, was used for analysing high-speed images. Another technique of evaluating schlieren images quantitatively was by integrating the distribution of the deflection angles, $\varepsilon(x,y)$, to calculate the density distribution, $\rho(x,y)$. However, the common problem encountered was that the intensity, I , at any point (x,y) on the image plane was influenced by the characteristics of the photographic plate material and the developing process (Merzkirch, 1987).

2.4.1 Schlieren Applications

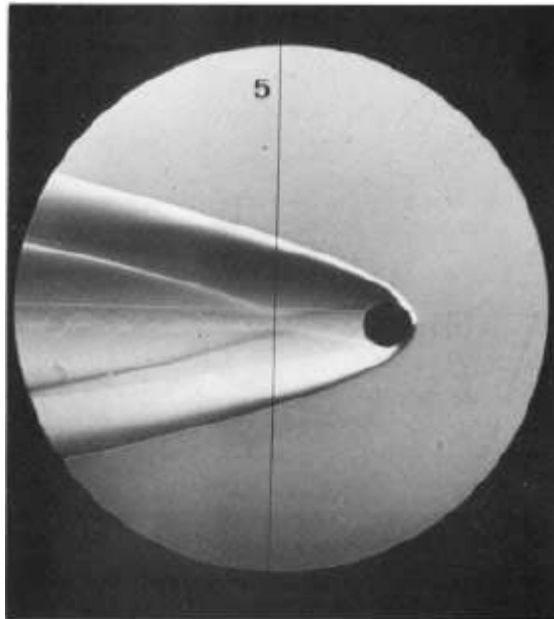


Fig. 2.10. Horizontal knife-edge schlieren photograph of the flow field around a sphere at hypersonic speed (Merzkirch, 1987).

Fig. 2.9 shows an example of a horizontal knife-edge schlieren photograph for the flow field around a sphere at hypersonic speed. The density gradients are visible and noted by the reverse in intensity levels as gradients change sign from top to bottom of the image.

2.4 Schlieren Imaging

Lamar (2001) demonstrated an example of a schlieren experiment that was setup in a wind tunnel. This is a typical system that would be set up for flow visualisation in a supersonic wind tunnel. Lamar's implementation consisted of a laser illumination and schlieren imaging techniques to observe shock waves generated around a wind-tunnel model in the Langley Unitary Plan Wind Tunnel (UPWT) at the NASA Langley Research Centre. Each test section of the UPWT test section was equipped with a single-pass, off-axis schlieren system, schematically shown in Fig 2.11. The system consisted of a light source, two spherical mirrors, knife edge, optical beam splitter, still camera, flat mirror, video camera, and image screen (Lamar 2001). This experimental arrangement was elaborate and, hence, time consuming to set up.

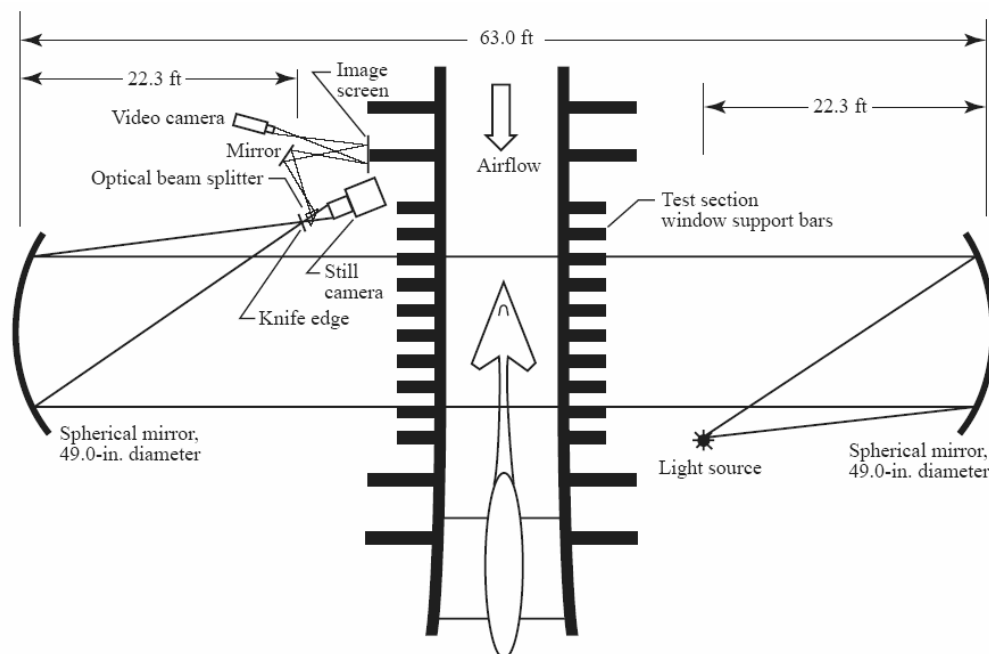


Fig. 2.11. Schlieren setup (Lamar, 2001).

Still photographs were acquired using a 70 mm Hasselblad camera. The images were scanned and processed using standard photographic software to achieve a greater detail for analysis of the shock shapes in the flow field. Large plates giving high-resolution images were used and hence fine details of flow structures could be viewed by zooming in on regions of interest.

Making use of digital recording technology would simplify the procedures involved to post-process and extract useful information from schlieren images. The resolution of such digital images is however limited by the size of the image sensor.

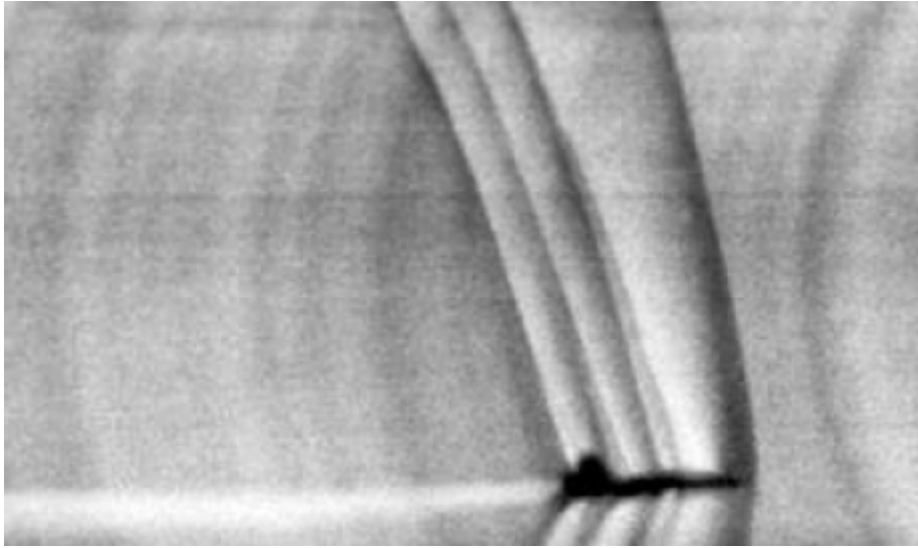


Fig. 2.12. T-38 aircraft flying at Mach 1.1 (Weinstein et al., 1997).

Under unusual lighting conditions, Weinstein et al. (1997) describe another application of the schlieren technique that can be used for large-scale flow fields. A system was used to visualise shock wave structures around a T-38 aircraft flying at Mach 1.1 from NASA Langley Research Centre to NASA Wallops test facility (Fig 2.12). The density changes across the strong shock waves were large enough to be directly visible by gross refraction. However, the experiment was only successful with particular lighting and background conditions dependent on the humidity of air. The appropriate condition for visualisation was rarely encountered. The experiment consisted of a high-resolution telescope with focusing capabilities and a streak camera. The telescope was focussed on the sun. A neutral filter was used to cut the sun intensity to a suitable level. Luminosity effects experienced in UQ's impulse facilities at high enthalpy conditions can be dealt with similarly. Weinstein's technique was also used successfully to visualise sonic booms of the F-18 and SR-71 aircraft flown from the NASA Dryden Flight Research Centre.

2.5 Interferometry

The interferometer is used to directly visualise the density (or index of refraction) field in a compressible flow. As discussed in section 2.1, both the phase and the path of the light beam change as a result of light propagating through a region of varying density. While shadowgraphy and schlieren techniques rely on the light deflection, the interferometry technique is used to evaluate the phase changes of the beam.

The Mach-Zehnder interferometer was the earliest use of the interferometry technique. The interferometer, as shown in Fig 2.13, consisted of a beam splitter, coherent light source, mirrors and a recording image system. The beam splitter separated the incident collimated beam into a reference and an object beam. Parallel fringes would appear on the image plane when a small intersection angle is introduced between the two beams. The fringes appeared deformed on the image plane with the light beam passing through a disturbed flow.

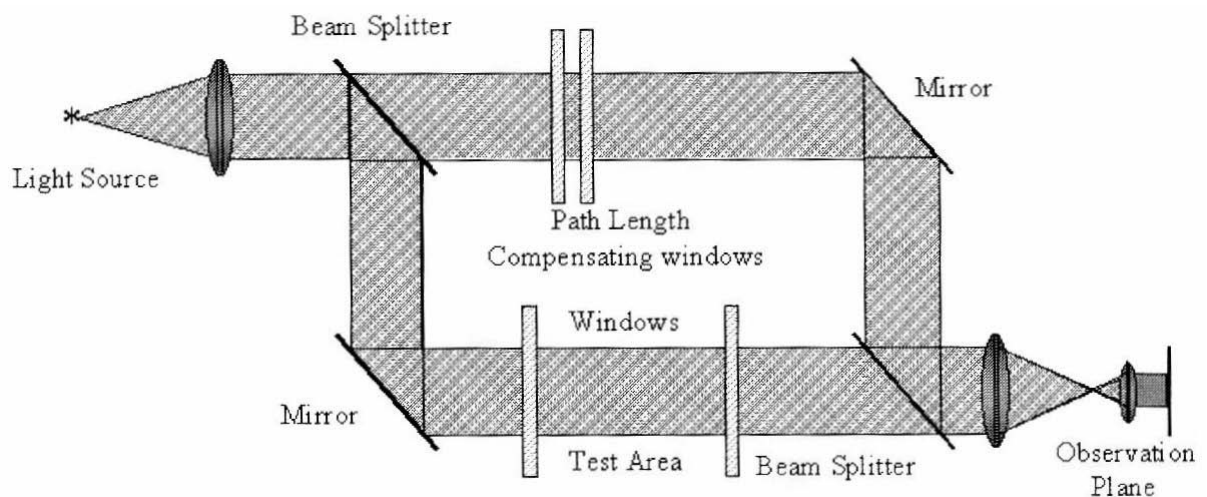


Fig. 2.13. Mach-Zehnder Interferometer (Smits and Lim, 2000).

2.5.1 Holographic Interferometry

The difference between Mach-Zehnder interferometry and holographic interferometry is that in the former two light beams emitted at the same time are spatially separated and then recombined to interfere, while in holographic interferometry the separation is temporal: two light beams following essentially the same optical path but at different times are recombined to interfere.

Holographic interferometry has been used in the study of the supersonic flow over scramjet models in the T4 shock tunnel and over re-entry aero-bodies in the X1, X2 and X3 superorbital expansion tunnels since early 1996.

Wegener et al. (1996) reports the use of the double exposure method in which two exposures were made on the same plate at short time intervals apart to visualise and analyse the shocks in the X1 super orbital tunnel operating at a total enthalpy of 86 MJ/kg. A wedge and a cylindrical model were tested and the results achieved are illustrated in Fig 2.14.

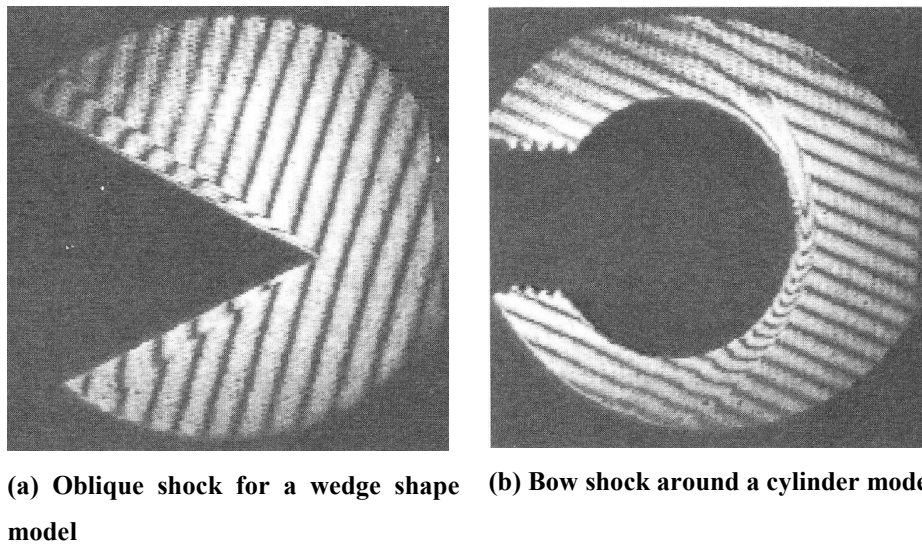


Fig. 2.14. Holographic interferograms (Wegener et al., 1996).

The density change across the oblique shock could be calculated from the measurement of the shock angle in the interferograms and using the expressions relating the densities, the flow Mach number and the model geometry. However, the shock stand off distance for the cylinder model did not give good agreement with the blunt body prediction given by Hornung (1972). This correlation was developed under the assumption of a 2-D flow that would not be valid for the small aspect ratio cylindrical model used.

Note that holographic interferometry can also be used to quantitatively evaluate the density field.

More recently, holographic interferometry was used for the study of the flow on the inlet of a scramjet engine (McIntyre et al., 2005). The experiment was conducted in the T4 reflected shock tunnel with a flat plate model at a slight angle of incidence to the

free stream mounted in the test section. A schematic diagram of the optical system used is shown in Fig 2.15.

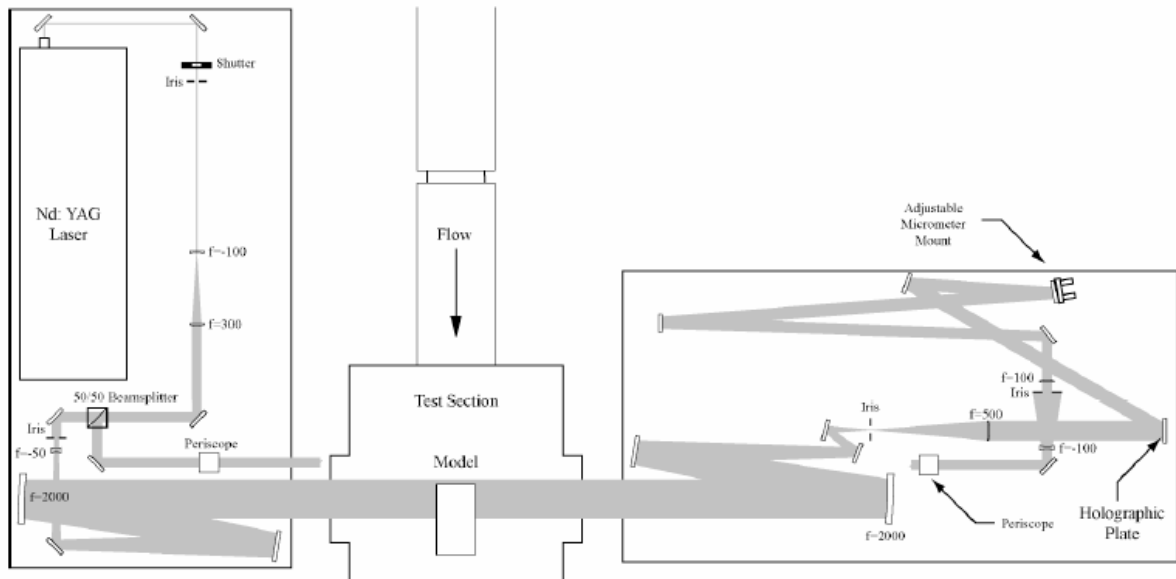


Fig. 2.15. Holographic interferometry layout (McIntyre et al., 2005).

An Nd:YAG laser of pulse width duration of 10 ns was used to generate a beam of light at 532 nm. Two holograms were recorded - one prior to the shot and the second during the test time. Bishop et al. (2001) describes a fast Fourier transform process that was used to determine the phase change $\Delta\Phi$ of the reconstructed interferograms. The density changes associated with the shock waves and shear layers were characterised by the fringe shifts in the interferograms as shown in Fig 2.16. The large fringe shift at the top of the image is caused by the shock wave from the tip of the flat plate. A small bow shock caused by the injection of fuel into the flow can be seen. The fuel layer is also visible.

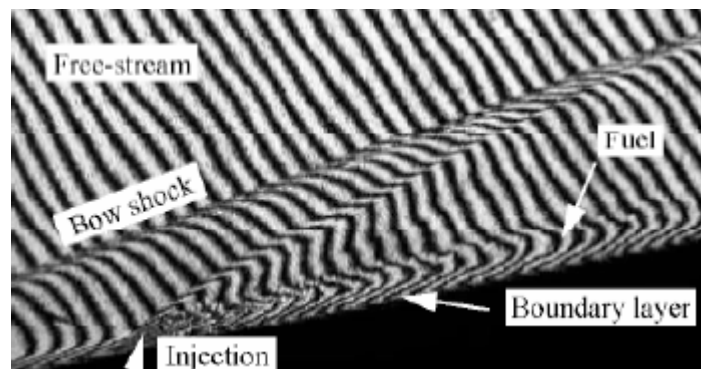


Fig. 2.16. Flow left to right over flat plate (McIntyre et al., 2005).

McIntyre (2005) presents the relationship between the phase change, $\Delta\Phi$, which is related to the summation of the Gladstone-Dale constant and the density change to i species in the flow,

$$\Delta\phi = \frac{2\pi W \sum K_i \Delta\rho_i}{\lambda}. \quad (2.10)$$

Here λ is the wavelength of the light. Using this expression, the compressible flow shock equations and the shock angle measured from the interferograms, the Mach number and flow density were calculated.

2.6 Recent Imaging Technologies for Flow visualisation

The development of digital imaging cameras at relatively low cost has brought about new techniques for non-intrusive flow visualisation techniques. One of these is the Background Oriented Schlieren (BOS) technique proposed by Meier (2002). This technique uses similar analysis techniques to those used in Particle Image Velocimetry (PIV) to extract flow information. In PIV, two images of a particle-seeded flow are recorded at a specified time interval apart. A laser or spark light is used to illuminate the particles, while a CCD camera is used to take the two images. The digital images recorded contain data about the flow and sensitive image processing techniques are used to extract this information. The information of interest in PIV is by how much the particles are displaced between the two consecutive images. This is typically evaluated using correlation algorithms.

In compressible flow aerodynamics, variations in flow properties occur due to the formation of shock waves around slender and blunted bodies, in other regions of more gradual compression, in regions of expansion and in regions dominated by viscous flows. The density varies in those regions. Flow investigation techniques, such as holographic interferometry and, more recently, BOS systems, have been introduced to use these density variations to visualise the flow.

2.6.1 BOS Principles

The BOS visualisation system makes use of a background dot pattern instead of the tracer particles used in conventional PIV. This technique is attractive because it makes use of simple optics. One other advantage of using the BOS method is its bi-directional sensitivity (Meier, 2002). The system is comprised of a high intensity light source, either pulsed or continuous, an unstructured pattern to be placed behind the flow field and an electronic camera to take the images of the flow field. In a simple realization of BOS, an unstructured dot pattern located in the background of a flow of interest is digitally photographed. The density gradients present in regions of inhomogeneities induce some distortion in the image recorded by the camera, compared to that recorded when there is an undisturbed field present between the camera and the background pattern. A photograph of the undistorted background pattern is taken as an additional

recording, so that a comparison of the two images can be used to derive information about density variations in the flow field under consideration.

The schematic in Fig. 2.17 illustrates the basic principle of operation of the BOS technique. The light rays are deflected through angle ε as they pass through regions of density gradients. The dotted line in Fig 2.17 represents a light ray passing through a region with no variation in density gradient. In the presence of a field with varying density gradient, the camera sees the same point at a distance Δy on the image plane, displaced from the original point. This displacement is calculated by cross-correlating the small windows in the two images. In this thesis, a novel, computationally inexpensive technique developed by Rösgen (2003) called the ‘sliding-template’ is used to search for the displacement vectors. This technique is essentially a search window that moves around the two images simultaneously to calculate a correlation map for each sub-window. The correlation map is evaluated using Fast-Fourier transforms and statistical operations. The peak value and its location on the map correspond to the maximum vector displacement and its position within that sub-window. A further step can be included to integrate these vector displacements using the Gladstone Dale equation to obtain flow density information.

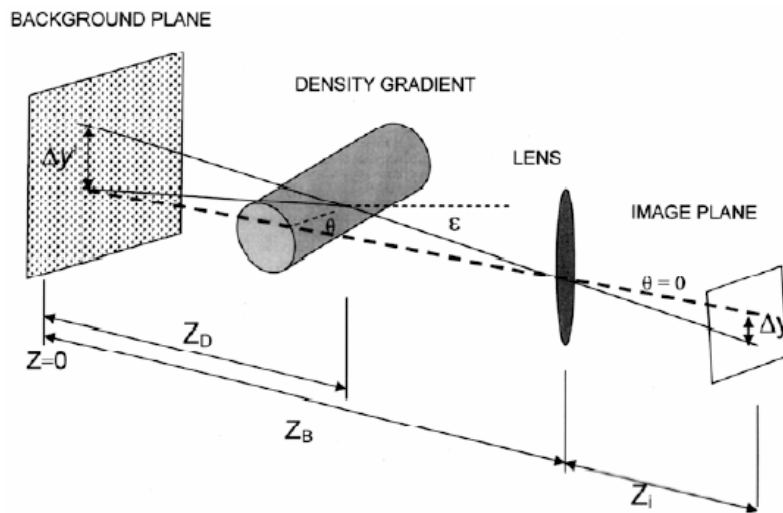


Fig. 2.17. Optical path for BOS measurement (Venkatakrishnan and Meier, 2004).

As discussed in section 2.2.1, the Gladstone Dale equation (Merzkirch 1987; Goldstein 1983) gives a relationship between the refractive index of a medium and its density. If n represents the refractive index and ρ is the density of the fluid in the medium, the relation between them is given by

2.6 Recent Imaging Technologies for Flow visualisation

$$n - 1 = K \rho, \quad (2.4)$$

where K is the Gladstone Dale constant. The Gladstone Dale constant depends on the characteristics of the gas in the medium and weakly on the frequency of light used. Knowing the relationship between the fluid density and its refractive index, the problem of how a light ray is disturbed in an inhomogeneous refractive field was investigated by Merzkirch (1987). Physical phenomena like diffraction and dispersion are disregarded in this analysis.

Dalziel et al. (2000) discussed the sensitivity of the technique in terms of varying distances between the background pattern, the inhomogeneous flow field and the camera. They outlined how an increase in distance Z_D , shown in Fig. 2.17, enhances the sensitivity of the system, while the distance $Z_B - Z_i$ is adjusted to maintain focus of the image. The distance $Z_B - Z_i$ can also be kept fixed when using a large focal length lens to project only the background image onto the CCD chip of the camera. However, to eliminate effects due to perspective distortions, the camera has to be placed as far away from the test section as possible. Part of the experimental program in this thesis will be focussed on assessing these ideas argued by Dalziel et al. (2000)

2.6.2 BOS experiments

Richard and Raffel (2001) performed feasibility tests for large-scale BOS aerodynamic investigations of the blade tip vortices of a helicopter in hover flight. The airfield grass was used as the unstructured background pattern and the helicopter was positioned about 100 m away from the grass. A progressive scan CCD camera with a resolution of 1280 by 1024 pixels was used and the exposure time was set to 200 μ s.

The vortex between the two blades can be identified in the displacement vector field plot (Fig. 2.18b). The interrogation size window used was 20 x 20 pixels. This experiment demonstrated the capability of using BOS without the need of an artificially generated background. Further tests using a two-camera configuration were proposed to acquire three-dimensional data such as position and orientation of the vortices. These results remained predominantly qualitative and no comparisons with theory or measurements were made.

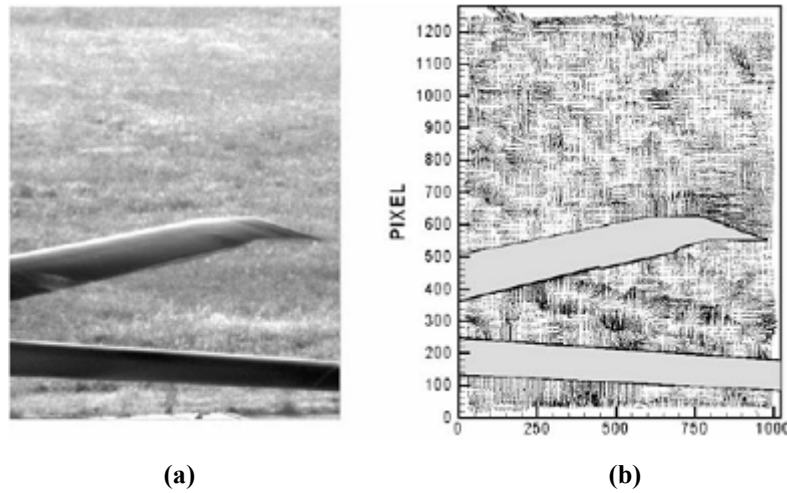


Fig.2.18. Joint work by NASA Ames & DLR to visualise vortex shedding of helicopter blades in hover flight (a) BOS image (b) Displacement field (Raffel et al, 1998).

Venkatakrishnan and Meier (2004) describe an attempt to quantifying the density field using the BOS technique. The model used was a 15° (semi-apex angle) cone-cylinder in a Mach 2 flow. This configuration would make it easy to validate BOS results against cone charts. The BOS images were analysed using a cross-correlation algorithm and a Gaussian sub-pixel interpolation method was used to evaluate the displacement to sub-pixel accuracy. The author formulated an equation relating the particle displacement, Δy , to the beam deflection angle, ε ,

$$\varepsilon = \frac{\Delta y Z_B}{Z_D f}, \quad (2.5)$$

where f is the focal length of the camera lens. Z_D and Z_B are the distances from the background pattern to the region containing the density gradient and the camera lens respectively.

The vectors of image displacement from Venkatakrishnan and Meier (2004) for a cone-cylinder model at Mach 2.0 are shown in Fig 2.19(a). The displacements between the surface and the shock are clearly visible so that the forebody shock wave can be identified. A region of expansion towards the rear of the cone can also be seen but the origin of the expansion appears to be upstream of the corner, not at the corner as would be expected. This may be because the black region indicating the model has been located incorrectly. Venkatakrishnan and Meier (2004) then calculated the line-of-sight integrated density field by solving the Poisson equation. Since their flow field was axisymmetric, they used a back-projection technique to determine the density field around the cone-cylinder model. The result is shown in Fig 2.19(b). The shock angles

2.6 Recent Imaging Technologies for Flow visualisation

were measured from the BOS images and were validated using cone charts and isentropic flow relations.

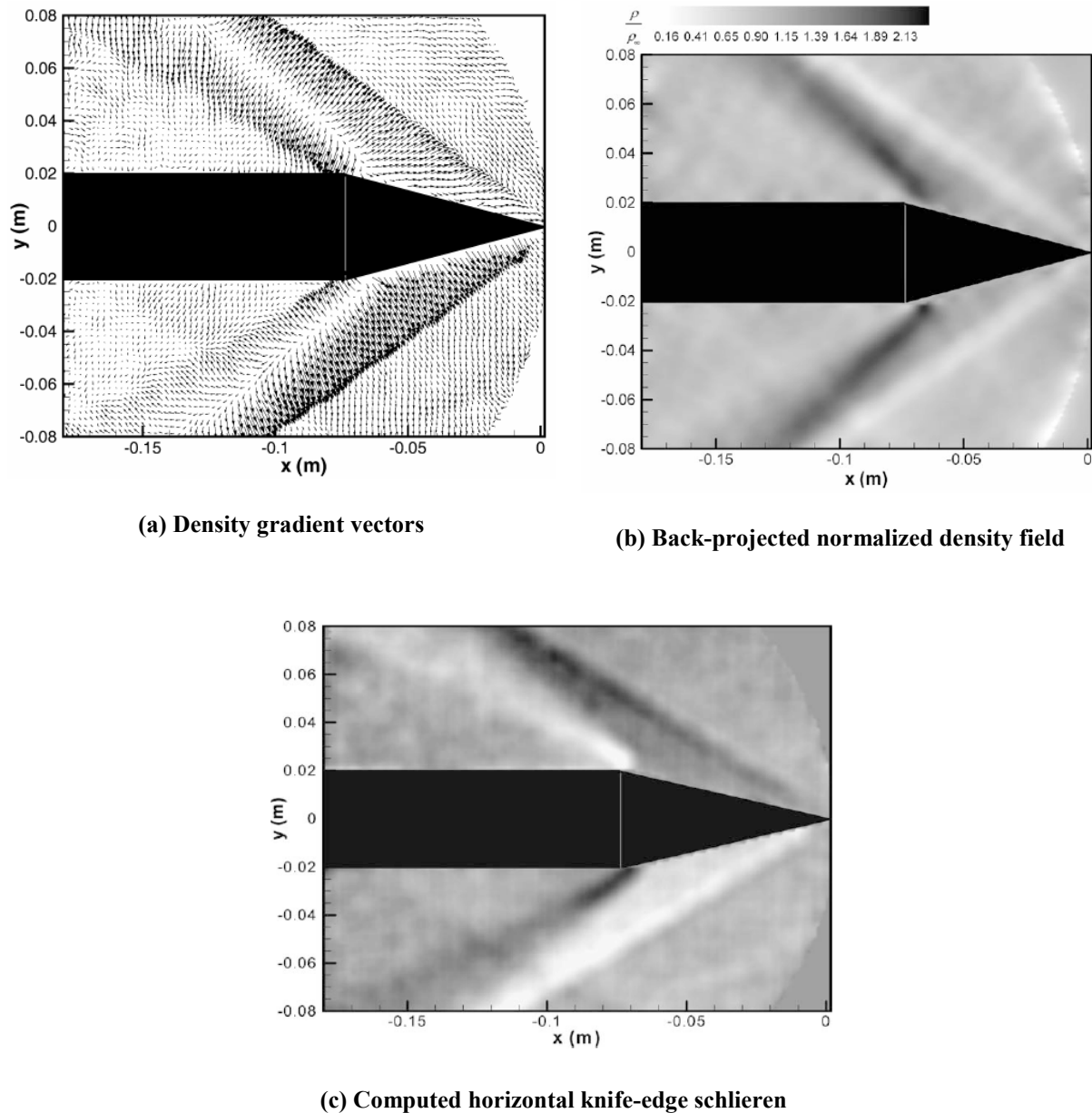


Fig. 2.19. Oblique shock wave on a cone-cylinder model at Mach 2.0 (Venkatakrishnan and Meier, 2004).

Venkatakrishnan and Meier (2004) then took the density field and produced a schlieren image by computing the first derivative of the density field in a desired direction. An example for the gradient of density in the vertical direction (producing a “horizontal knife edge” schlieren image) is shown in Fig 2.19(c). The resulting image is not as clear as a conventional schlieren image, but it does show the major features in the flow.

PIV Evaluation and Background Oriented Schlieren

3.1 Introduction

The image processing for Background Oriented Schlieren flow visualisation is comprised of two main components:

- the calculation of displacement vectors from a flow and a no-flow image, and
- using the displacement vectors to generate schlieren type images or to use a qualitative analysis to determine the density field.

This chapter describes the PIV style image processing technique used to analyse the two images. It is appropriate to briefly summarize particle tracking techniques since much of the analysis used in BOS is based on techniques developed for particle tracking. Therefore, a synopsis of some velocimetry techniques is given in section 3.2. This is followed by an introduction to the BOS technique and the statistical theory on which the PIV image processing relies. The uncertainties associated with PIV measurement due to noise or introduced during the interrogation and cross-correlation procedures are examined. The results of the PIV procedure are estimates of the magnitudes and directions of the displacement of the background pattern i.e. displacement vectors that represent the field of the refractive index gradient or density gradient.

3.2 Particle Tracking Techniques (PIV, PTV, LSV)

PIV was developed primarily for measurement of velocity fields in experimental fluid mechanics studies (Adrian, 1991). PIV is used to obtain the velocity of particles seeded into a fluid flow and has been applied to a diverse range of flows including water dynamics, aerodynamics, air-conditioning systems, acoustics, blood circulation and boundary layer turbulence. PIV measurements result in a 2-D velocity vector map of a flow field at an instant in time by acquiring and processing two images of particles seeded in the fluid. It is based on the assumption that the speed of the seeded particle is equal to the speed of the flow. The displacement of particles found between the two images divided by the time interval between when the images were captured is used to calculate the flow speed. The particle velocity represents the fluid velocity, provided the seeded particles satisfy certain criteria, which are discussed next.

The tracer particles seeded into the flow have to follow the flow faithfully because the velocity of a particle is assumed to be identical to the local flow velocity. Also, the particles should not alter the flow and should not interact with each other. This introduces the requirement for small particles and high intensity illumination such as a powerful-pulsed laser. For most experiments the desired seeding particles are non-toxic, non-corrosive, non-abrasive, non-volatile and chemically inert. A wide variety of seeding particles is available for velocimetry experiments (Melling, 1997), which makes the technique very accessible. Olive oil and alcohol droplets are most commonly used in wind tunnels for flow visualisation.

For high-speed flows, a powerful seeding generator is required to maintain an adequate concentration of tracer particles in the fast-moving flow. Flows such as those in shock tunnels are difficult to seed uniformly.

Oil is most usually used for tracer particles in Particle Tracking Velocimetry (PTV), Laser Speckle Velocimetry (LSV) and Particle Image Velocimetry (PIV). In PTV, there is a low density of seeded particles in the flow and the displacement of the individual seeded particles is found from the two images. This is possible because there are large distinct distances between the particles in the two images. The particle image pairs that correspond to the same tracer particle in the flow can then be identified. However, using this technique, the flow velocity cannot be determined at any arbitrary position in

PIV Evaluation and Background Oriented Schlieren

the flow field because tracer particles can be missing in that area. Another shortcoming of this technique is that the spatial resolution of the method is not usually suitable for investigating complicated flow structures such as expansion waves, shock interactions and boundary layer development.

In PIV, the test region is densely seeded with tracer particles so that one can still distinguish individual particles but tracking them individually is not possible. However, the flow is seeded densely enough to enable the velocity to be determined at any point in the field, hence allowing high spatial resolution to be achieved. In PIV, images of a group of particles are analysed by auto-correlation or cross correlation analysis methods, depending on the image acquisition modes. The auto-correlation scheme works in a one-frame, two-exposure mode while cross-correlation needs two frames that are exposed only once each. The whole flow field image is divided into smaller areas (sub-windows) that can be analysed individually to give flow information.

With the LSV technique, the flow is very densely seeded so that the particles overlap and form a random interference pattern or speckles upon illumination. Statistical analysis of a group of particles of the dense particles or speckle pattern reveals the most probable particle or speckle displacement. Small particle sizes are favourable in LSV to improve flow tracking, but PIV requires the particles to be suitably large to improve light scattering, hence achieving better resolution.

3.3 Principles of the Background Oriented Schlieren

Richard and Raffel (2001) proposed and demonstrated the Background Oriented Schlieren (BOS) technique, which uses a background dot pattern and PIV image processing techniques. Today BOS is finding wide-ranging applications as a non-intrusive yet simple technique for investigation of compressible flow phenomenon. For BOS analysis, one image is captured prior to the experiment (the reference image), and one is taken during the test when the flow is established in the tunnel test section (the distorted image).

The BOS method developed primarily by Meier (2002) has some similarities with the "synthetic schlieren" system developed by Dalziel et al. (2000). However, they are different. BOS relies on the distortion of a background pattern while synthetic schlieren involves matching a real background grid with a synthetic one in the camera.

The technique can be used to measure certain properties of the flow, such as density and temperature. Jensen (2003) gives a detailed description of the mathematical principle of BOS as a tool to measure 2-D temperature fields of cryogenic gas flows. These measurements were undertaken in a heavy gas tunnel at the Institute of Fluid Dynamics, ETH (Zurich). This method is much simpler to set up than conventional schlieren systems and uses sensitive correlation algorithms together with high performance digital acquisition systems and digital image processing. The schematic in Fig 3.1 illustrates the processes involved to extract a 2-D temperature field from two images captured with a short inter-frame delay.

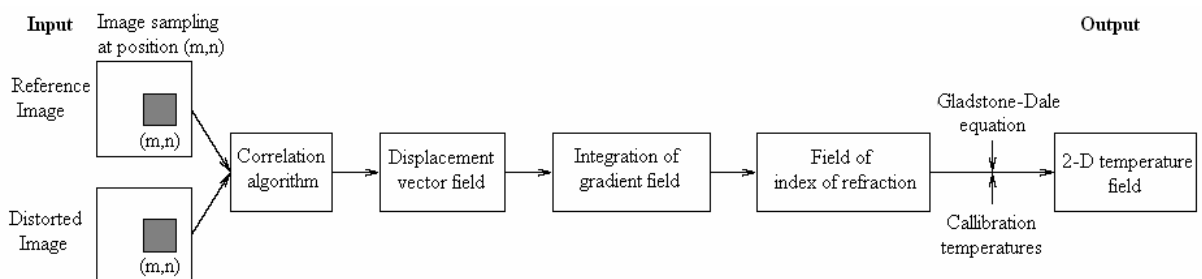


Fig 3.1 Flow chart of temperature calibration using BOS (Jensen, 2003).

Using the ideal gas laws, the field of refractive index and the Gladstone-dale constant for a particular gas, Jensen (2003) quantitatively described a 2-D temperature field of

the cryogenic flow. A constant pressure had to be assumed so that the temperature field could be inferred from the field of refractive index measured using the BOS system. For calibration, thermocouples were placed in the flow to determine the temperature at specific points.

The BOS system requires analysis of the two images. Image processing tools, such as the Matlab image Processing toolbox or Python Imaging Library (PIL), can be used to read the images, and represent them in terms of pixel values in a matrix, the size of which depends upon the resolution of the CCD imaging device. For instance, a camera capable of capturing images at a resolution of 1200 x 1600 corresponds to an array of 1200 x 1600 locations. At each pixel location, a colour image will have a Red, Green and Blue value, hence an array size of 1200 x 1600 x 3. Images converted to grey scale result in a 1200 x 1600 array bearing a value ranging from 0 to 255 for 8 bits depth. A black pixel has value zero while a white pixel has value 255. The differences in the pixel values between the reference and the flow image provide data on the behaviour of the flow. This difference can be assumed to be the amount by which the image was displaced due to the flow. Using cross-correlation algorithms, the vector displacement at each pixel location in an image can be evaluated. This is explained in section 3.2.2. However, the effects of vibration in an experiment need to be corrected before correlating a subset of the images to detect displacement vectors. This is described next.

3.3.1 Estimating the shift between the flow off and flow on images due to vibration

Vibration of the tunnel or camera movements can cause changes in the background images between the flow and no-flow images. These differences are usually small and are not detectable with the naked eye. In the analysis, a displacement detected in subsets of the two images at locations where no displacement is expected indicates that there has been some distortion or movement. An example of such a region is labelled as A in Fig. 3.1, which shows the flow past a conical model in a supersonic flow.

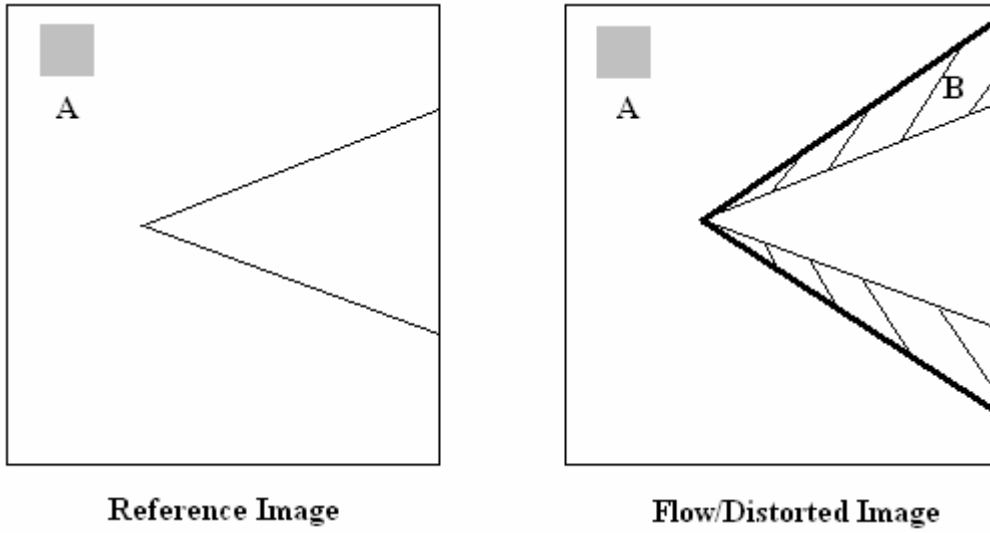


Fig. 3.2. Schematic of an oblique shock.

Region A is well outside the region where density changes due to the presence of the test model would be expected. For the conical model in Fig. 3.2, density variations in the flow image would be expected only near the cone (for example in region B). To identify whether there is noise due to vibration of the camera or tunnel, the small region A is compared between the no-flow and flow images using an FFT based cross-correlation algorithm. Using the coordinates of the location of the peak value, (x_p, y_p) in the cross-correlation evaluation, the displacements or shifts, x_{sh} and y_{sh} , between the images can be identified. This is illustrated in Fig. 3.3 where the size of the window A is $C \times D$. The dimensions C and D must be at least larger than the displacement of the undistorted background pattern between the flow and no flow images in the x and y directions, respectively.

The shifts in the horizontal and vertical directions are evaluated as follows,

$$x_{sh} = x_p - \frac{C}{2}, \text{ and} \quad (3.1)$$

$$y_{sh} = y_p - \frac{D}{2}. \quad (3.2)$$

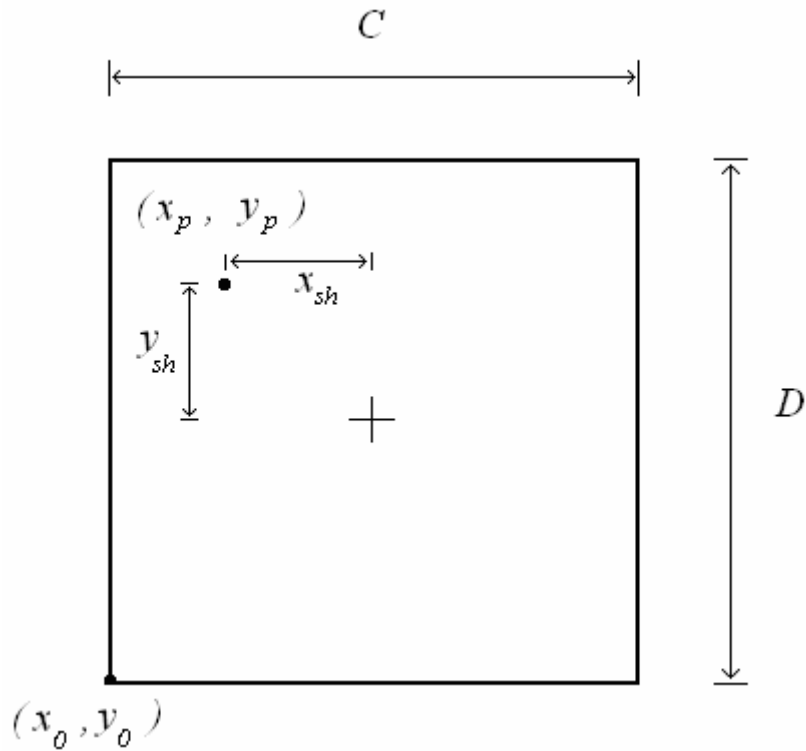


Fig. 3.3. Evaluation of the noise shifts from cross-correlation data.

3.3.2 Evaluating the displacement of the background pattern due to density gradients

This section describes the next step in the BOS evaluation whereby displacement vectors are estimated from the corrected images. As outlined in section 3.1, a statistical approach is required to analyse the images because of the proximity and randomness of the dots. The five main steps in the process of obtaining a displacement field estimate are:

1. Converting the image files to numeric arrays.
2. Filtering the data using a 2-D median filter.
3. Cropping a sub-window, or sliding window, that will move throughout the entire image.
4. Computing the cross-correlation function or correlation map for each window using 2D-FFT, as described in Fig 3.5.
5. Determining the correlation peak and its location on the correlation map.
6. Resolving displacements to a sub-pixel accuracy using a Gaussian peak-fitting scheme.

3.3 Principles of the Background Oriented Schlieren

7. Calculating the displacement vectors and assigning the values in matrices, x , y , u and v .

3.3.2.1 Statistical analysis in PIV

In this section, the mathematical background of statistical PIV is explained. This procedure leads to the calculation of the displacement vectors from the flow and no-flow images. The FFT-based procedure to detect the displacement of the background dot pattern that is employed here is similar to that used to detect for the displacement due to vibration that is described in section 3.3.1. Other techniques such a PIV and LSV, as outlined in section 3.2, use a similar approach, whereby the displacements of groups of particles, are used to determine the velocity field. These displacement vectors are found by cross correlating two sub-windows, one from the reference image and the other from the distorted image.

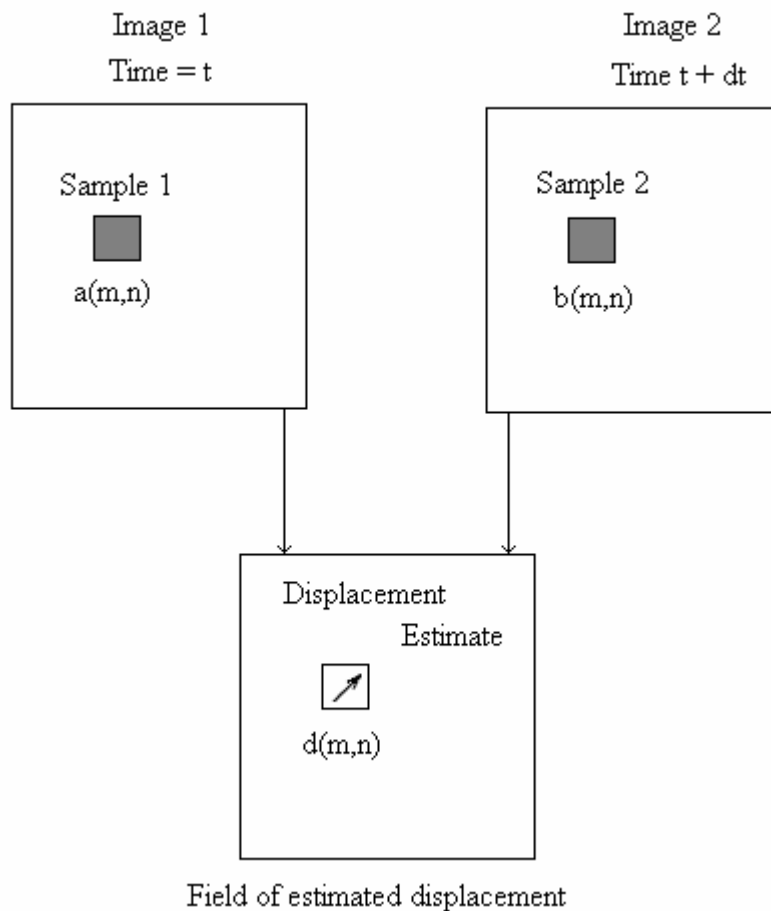


Fig. 3.4. Conceptual arrangement for displacement vector estimate (Raffel et al., 1998).

The two sub-windows or interrogation windows are of the same size and are at the same location in both images as shown schematically in Fig 3.4. The sub-window is moved throughout the image and a cross-correlation at each location is used to determine the magnitude of the displacement between the flow and no flow images for each sub-window. The cross-correlation function is effectively a pattern-matching routine, which determines by how much the flow image must be displaced to cause it to line up with the no flow image. This process is repeated at each grid point within the image, resulting in a map of displacement vector. The computational time required to evaluate the x and y displacements depends on the size of the correlation window

Correlation schemes are based on the idea of either maximizing or minimizing a function that describes the relationship or inconsistency between two sub-windows $a_{i,j}$ and $b_{k,l}$ where i, j, k and l are used to specify integer indices of arrays and vectors. For a least squares approach, the correlation coefficient is minimized while for the cross-correlation analysis, the function, $corr_{k,l}$ is maximized. Jensen (2003) gives a good description of the cross-correlation method, which is summarised here. The cross-correlation coefficient, $corr_{k,l}$ (Bronstein and Semendjajew, 1991) is given by

$$corr_{k,l} = \frac{Cov(a_{i,j}, b_{i+k,j+l})}{\sqrt{Var(a_{i,j})Var(b_{i+k,j+l})}}, \quad (3.3)$$

with the covariance given by

$$Cov(a_{i,j}, b_{k,l}) = \frac{1}{(M-1)(N-1)} \sum_{m=0}^{M-1} \sum_{n=0}^{N-1} (a_{i+m,j+n} - \bar{a}_{i,j})(b_{k+m,l+n} - \bar{b}_{k,l}), \quad (3.4)$$

variance given by

$$Var(a_{i,j}) = Cov(a_{i,j}, a_{i,j}). \quad (3.5)$$

and the mean value of the interrogation region given by

$$\bar{a}_{i,j} = \frac{1}{M \cdot N} \sum_{m=1}^M \sum_{n=1}^N a_{i+m,j+n}. \quad (3.6)$$

M and N are the height and width of an image, respectively,

3.3.2.2 The Fourier Domain

The direct calculation of the cross-correlation coefficient $corr_{k,l}$ given in section 3.3.2.1 is an expensive and time consuming procedure. Fast Fourier Transform (FFT) techniques are used instead to correlate the large image matrices for large images.

3.3 Principles of the Background Oriented Schlieren

Evaluating the correlation using the fast Fourier Transform is significantly more efficient than the direct calculation. Each FFT involves $N^2 \log_2 N$ calculations, for an interrogation area size $N \times N$. In real space, at least $2M^2 N^2$ calculations are required to obtain each vector. One restriction of the FFT however is that the size of the input data (i.e. the interrogation area) must be a power of two (Raffel et al., 1998). The Fourier transform in discrete form (DFT) for a 2-D image $i(k, l)$ is given as (Jain, 1989)

$$DFT[i(k, l)] = I\left(\frac{m}{M}, \frac{n}{N}\right) = \sum_{k=0}^{M-1} \sum_{l=0}^{N-1} i(k, l) e^{-j2\pi\left(\frac{mk}{M} + \frac{nl}{N}\right)} \quad (3.7)$$

$$(m, n) = (0, 0) \dots (M-1, N-1)$$

and the inverse transform as

$$DFT^{-1}\left[I\left(\frac{m}{M}, \frac{n}{N}\right)\right] = i(k, l) = \frac{1}{MN} \sum_{m=0}^{M-1} \sum_{n=0}^{N-1} I\left(\frac{m}{M}, \frac{n}{N}\right) e^{j2\pi\left(\frac{mk}{M} + \frac{nl}{N}\right)} \quad (3.8)$$

$$(k, l) = (0, 0) \dots (M-1, N-1),$$

where $j = \sqrt{-1}$. To obtain the correlation in the Fourier space, each of the interrogation areas is Fourier transformed. These Fourier transforms are then multiplied together, and the product is inverse Fourier transformed to produce the cross-correlation data as illustrated in Fig 3.5. The multiplication of the inverse Fourier transforms, which is equivalent to a correlation in real space, is described in the Wiener-Khintchine theorem for power spectrum (Couch, 2001).

Input

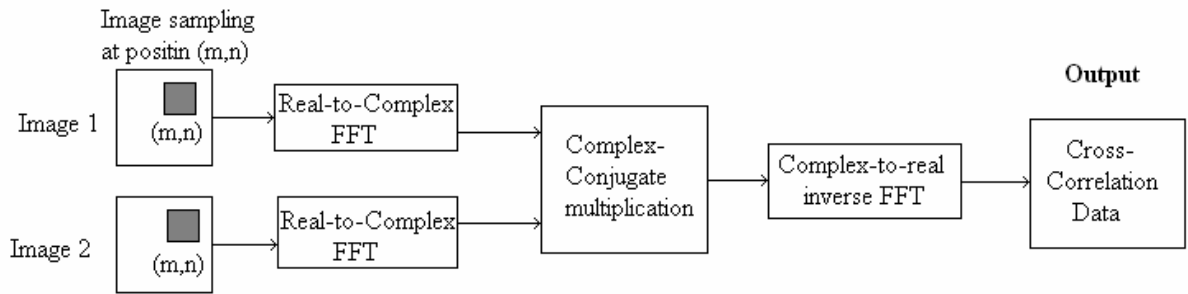


Fig. 3.5. Implementation of cross-correlation using fast Fourier transforms.

The correlation of the two images can then be written with the correlation theorem as

$$corr(s, t) = \sum_{k=0}^{M-1} \sum_{l=0}^{N-1} i_1^*(k, l) i_2(s+k, t+l) = DFT^{-1}\left[I_1^*\left(\frac{m}{M}, \frac{n}{N}\right) I_2\left(\frac{m}{M}, \frac{n}{N}\right)\right], \quad (3.9)$$

where I_1^* is the complex conjugate of the reference image, $i_1(k, l)$, and $i_2(k, l)$ is the flow image data. M and N are the sizes of the interrogation window in pixels.

3.3.2.3 Correlation peak search

The correlation plane consists of a series of peaks, one of which is significantly higher than the others. The location of a principal peak in a particular interrogation area indicates the best estimate of the average particle displacement within that area. Since the input data applied to the FFT correlation algorithm are assumed to be periodic, the correlation data itself is also periodic in the correlation plane. A peak corresponding to a displacement Δx_{true} of greater than $\frac{N}{2}$, where N is the length of a set of data containing displacements, will be ‘wrapped around’ and mapped to a new position $\Delta x_{measured}$ such that $\Delta x_{measured} = \Delta x_{true} - N$. The correlation function is then said to be *aliased*, and the displacement peak will not result in a displacement vector that accurately represents the density gradient in the flow. In PIV, the solution to this problem is to either increase the size of the interrogation area or reduce the illumination time delay (Raffel et al., 1998). In BOS, the corresponding solutions are to either increase the size of the interrogation area or to reduce the sensitivity of the BOS system.

One approach to prevent the overlapping of real data in the image centres is to surround the image data with zeros. This method is known as *zero padding*. However this method does not perform well because the sudden change between recorded pixel values and these zero values introduce high frequency noise, which deteriorates the cross-correlation signal. Removing the mean value of the interrogation area pixels and performing a normalised correlation can avoid the overlapping problem. This is the method adopted in this thesis.

The *sinc* function algorithm (Rösgen, 2003) is a method for finding the true position of the correlation peak. This peak search function is an efficient method for the computation of the subpixel-accurate correlation peak position without introducing systematic errors due to the periodicity of the data. The direct summation formula is

$$corr_{int}(x, y) = \sum_{M=0}^{M-1} \sum_{n=0}^{N-1} corr(m\Lambda, n\Lambda) \sin c(x - m\Lambda) \sin c(y - n\Lambda) \quad (3.10)$$

where $c_{int}(x, y)$ is the interpolated result and $corr(m\Lambda, n\Lambda)$ is the correlation map sampled with a rate Λ (Oppenheim and Schaffer, 1975, Brigham, 1974). The *cardinal sine* or *sinc* functions are defined as

3.3 Principles of the Background Oriented Schlieren

$$\sin c(x - m\Lambda) = \frac{\sin(x - m\Lambda)}{x - m\Lambda} \quad (3.11)$$

and

$$\sin c(y - n\Lambda) = \frac{\sin(y - n\Lambda)}{y - n\Lambda}. \quad (3.12)$$

This approach however is inappropriate at the edge of the image data interval because the interpolation becomes increasingly inaccurate due to missing data points. Rösgen (2003) employs an FFT-based computation to solve the cross-correlation by assuming a periodic data set. This method is not employed in this thesis but instead a Gaussian fit is used to fit the correlation peaks to obtain a subpixel accurate estimate of the displacement.

3.3.2.4 Gaussian peak-fit for sub-pixel accuracy

Raffel et al. (1998) point out that fitting the correlation peak to some function is the most fundamental procedure in a PIV evaluation. Known robust correlation peak fitting methods are the centroid or centre of mass, the parabolic and the Gaussian methods. The Gaussian-fit three-point estimator is the most widely used procedure for PIV evaluations. This is described next.

Referring to the correlation theorem given in section 3.2.2.2, the location of the discrete peak in the correlation distribution $corr(s, t)$ gives the mean particle displacement within i_j . To achieve sub-pixel accuracy of this mean particle displacement, a smooth curve is fitted to three points in the vicinity of the discrete peak, here a Gaussian curve. The Gaussian peak fit is defined as

$$f(x) = Q \exp\left[-\frac{(x_0 - x)^2}{F}\right], \quad (3.13)$$

where Q and F are constants.

Four surrounding values in the neighbourhood of the discrete peak (s_p, t_p) are extracted from the correlation data, as illustrated in Fig. 3.6. The Gaussian function is fitted to three points in each direction, which corresponds to the component displacement

vectors, Δx and Δy . The open dot (s_p, t_p) represents the location of the peak correlation value while the filled dots are the surrounding correlation values.

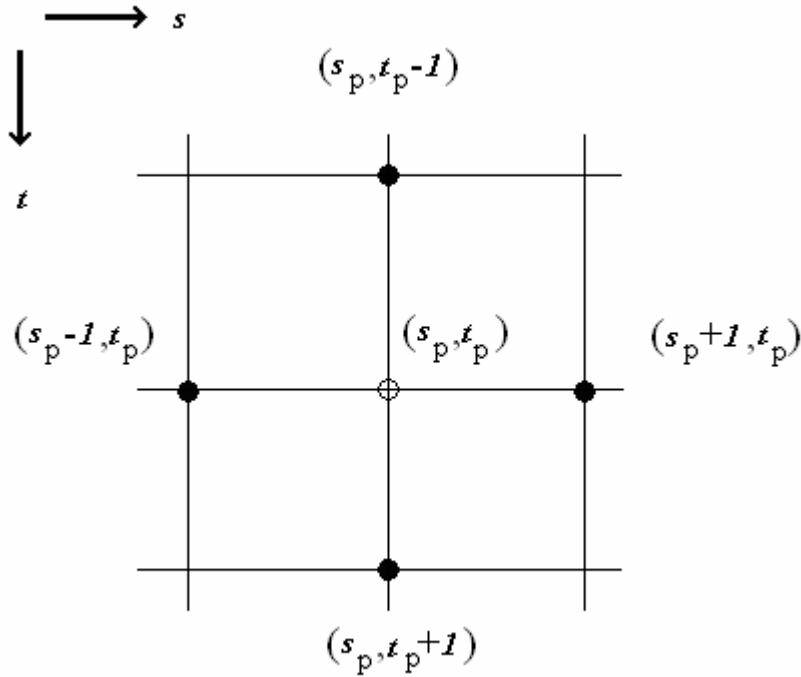


Fig. 3.6. The maximum correlation value on the correlation plane (open dot) and four surrounding correlation values (full dots) (Westerweel, 1993).

Using the function $corr(s,t)$, that describes the correlation plane, the peak location and the surrounding points, the vector displacement in the *horizontal* direction using the Gaussian sub-pixel curve fit can be calculated as follows (Westerweel, 1993),

$$\Delta x = s_p + \frac{\ln corr(s_p - 1, t_p) - \ln corr(s_p + 1, t_p)}{2 \ln corr(s_p - 1, t_p) - 4 \ln corr(s_p, t_p) + 2 \ln corr(s_p + 1, t_p)} \quad (3.14)$$

and for the vertical direction,

$$\Delta y = t_p + \frac{\ln corr(s_p, t_p - 1) - \ln corr(s_p, t_p + 1)}{2 \ln corr(s_p, t_p - 1) - 4 \ln corr(s_p, t_p) + 2 \ln corr(s_p, t_p + 1)}. \quad (3.15)$$

Westerweel (1993) makes a qualitative comparison between the three types of three-point estimators and outlines their performances and robustness. The centroid method works best with broad correlation peaks while the parabolic fit does not need any previous knowledge about the correlated plane. For the parabolic fit method, a parabola

3.3 Principles of the Background Oriented Schlieren

is exactly fitted to three points and the maximum of the parabola defines the correlation peak. The Gaussian fit however, takes into account the shape of the correlation plane by considering the fact that the image covariance function is approximately a Gaussian curve. This peak fit procedure shows better performance and is used here. However, several papers point out the bias towards discrete values introduced in this sub-pixel interpolation scheme (Raffel et al., 1998, Fincham and Spedding, 1997, Christensen, 2004). This problem is referred to, as the *peak locking error* and the *Sinc* function discussed in 3.2.2.3, can overcome this difficulty. Other schemes exist, such as the iterative grid refinement methods proposed by Lecordier *et al* (1999), the continuous window shifting method of Wereley and Gui (2002), the central difference image correction method (Gui and Seiner, 2004) and the peak anti-aliasing, spline transformed interrogation scheme (Fincham and Delerce, 2000). However, most of these schemes involve significant processing time. Chen and Katz (2005) proposed a correlation map method that can solve the *peak-locking* problem.

The methods described in this section can be used to provide very accurate estimates of the density gradient field. The density gradient estimates can be used to obtain a quantitative measure of the density field. This can be achieved by integrating the gradient vectors along the light path length.

The density gradient vector results can also be used to generate schlieren images. Appropriate grey levels are assigned to each pixel of the schlieren image according to the associated density gradient vector. This is described in section 3.4.

3.4 Schlieren-like image of the density field

Schlieren gives a qualitative visualisation of the flow field. Using the density gradient vectors determined using the techniques described in section 3.3, schlieren images can be generated computationally. Venkatakrishnan and Meier integrated the vertical gradient vectors to obtain a horizontal knife-edge schlieren image for the flow around a pencil-cone model. This is described in section 2.6.2. An alternative method to produce schlieren images of either horizontal or vertical knife-edge orientations is possible by generating filled contour plots of the component vectors. A filled contour plot of the vertical displacement vectors can represent a horizontal knife-edge schlieren image while a filled contour of the horizontal displacement vectors can represent a vertical knife-edge schlieren image. To achieve a high white-grey contrast, the contour levels between which to generate the contour plot can be determined by plotting histograms showing the frequency distribution of the vertical and horizontal displacement vectors in the flow field. To the authors' knowledge, this method was not attempted before. Results are presented in Chapter 5.

3.4.1 Conclusion

The image processing algorithms described in this chapter have been implemented in a Python programming platform. Details of the implementation are given in Appendix A. A user manual for the package developed at The University of Queensland, describing how to acquire two images using the camera software and how to process the images using the Python program, is given in Appendix B.

Experimental details

4.1 Introduction

The experiments for the present investigation were conducted in the low enthalpy Drummond shock tunnel and the T4 free piston reflected shock tunnel at the Division of Mechanical Engineering of The University of Queensland. The Background Oriented Schlieren system, described in Chapters 2 and 3, was shown to be an easy way to qualitatively and quantitatively investigate aerodynamic flows. The flow characteristics in hypervelocity facilities can be studied with this technique and its implementation is described here.

In the first series of tests, the applicability of the BOS technique to analyse flows over an axi-symmetric 20° sharp cone, a model of the Muces-C re-entry body (Kawaguchi et al., 1999) and a 5° blunt cone were tested in Drummond shock tunnel. It is possible to perform several shots in one day using this facility. The test section is also easily accessible and the models can be changed rapidly. These benefits were put to use to perform further tests in a second series of experiments targeted towards analysing the sensitivity of BOS and determining the arrangements necessary for visualisation in flows typical of those used in scramjet studies. The 20° sharp cone was used in a sensitivity study and ways of increasing the sensitivity were investigated. Once BOS was thoroughly investigated and the image- processing program fully developed, the technique was implemented in a higher enthalpy facility, the T4 shock tunnel.

The T4 tunnel has specific scheduled experimental campaigns. The tunnel is used mainly for scramjet research. A specific campaign for BOS visualisation in this tunnel was not planned since the facility was fully booked. However, the technique was applied when there was an appropriate model in the tunnel. The models tested had either

no sidewalls or glass sidewalls so that light from the source can pass through the density-changing region of interest in the test section to the camera. During this thesis, there were four campaigns in T4 with appropriate models for BOS visualisation. Firstly, BOS was used to visualise the flow over an axis-symmetric scaled scramjet model used in a force balance experiment. Secondly, the technique was tested for the flow over a 2-D flat-plate, in a test for new aerospace material subjected to the high temperatures within a shock layer. The BOS system was set up in T4 in a third test campaign to visualise the flow over a flat plate from which hydrogen was injected close to its leading edge. Lastly, the technique was used to visualise the intake region of a scramjet inlet. Brief overviews of these projects are given in section 4.3.

Following this is a description of the two facilities and an explanation of the reflected shock phenomena observed in the Drummond tube. The initiation of the shock in the shock tube is different for the two facilities. The Drummond tube uses a piercer mechanism to rupture an aluminium diaphragm, while in T4 a piston compresses the driver gas in the compression tube to burst a steel diaphragm. However, the principle of shock propagation and reflection in T4 shock is similar to that in the Drummond tunnel. Sections 4.2 and 4.2 in this chapter are devoted to the description of the facilities.

4.2 The Drummond Shock tunnel

The Drummond tunnel is a relatively low enthalpy hypervelocity flow facility, operating up to a maximum enthalpy of 3.0 MJ/kg and total temperatures in the nozzle supply region limited to 2500 K. It has a fixed length high- pressure driver. The layout of the Drummond tunnel is shown in Fig 4.1. The tunnel has been mainly used to develop instrumentation and to study phenomena that appear in larger facilities. It is inexpensive to operate. The glass windows at the test section make the facility suitable for optical flow diagnosis. As such, many laser-based investigation for flow visualisation were done using this facility in the past. For the current research, the BOS technique was first tested through a series of experiments in the Drummond tunnel before moving to the larger T4 facility.

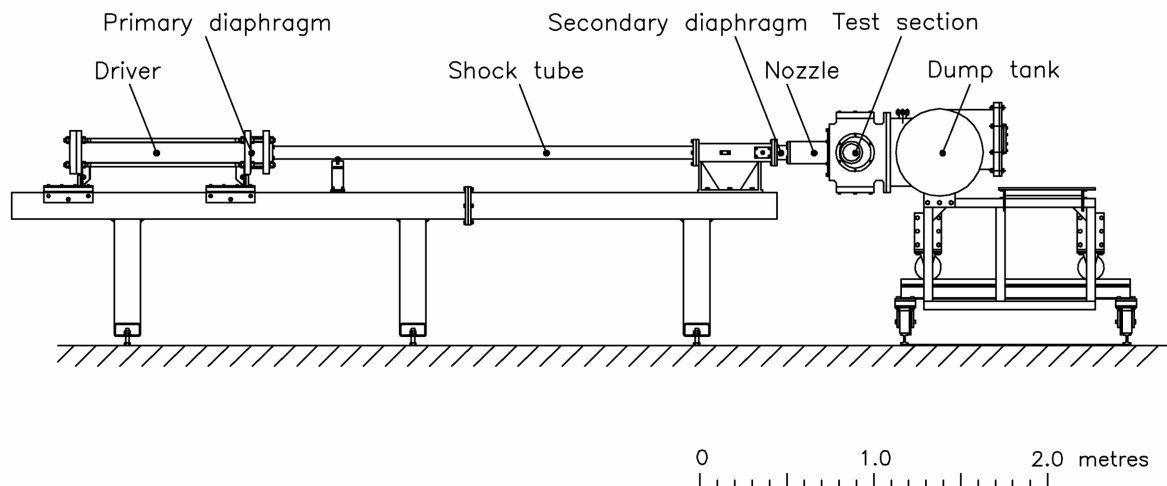


Fig. 4.1. Diagram of the Drummond tunnel (Craddock, 1999).

The tunnel is made up of a driver tube, a shock tube section of 65 mm internal diameter, a nozzle, a test section region and the dump tank. An 8° conical nozzle block with two throat inserts, nominally Mach 4 and 7 were made for this facility (Austin et al., 1997). The driver and the shock tube are separated by an aluminium diaphragm, usually referred to as the *primary* diaphragm. The driver section is kept at high pressure while the shock tube section contains a low-pressure test gas. The whole facility is evacuated to a low pressure before each test. The shock tube pressure usually ranges between 3 and 5 torr prior to filling with the test gas.

A cellophane *secondary* diaphragm, placed at the nozzle throat, separates the shock tube from the dump tank. This prevents the test gas from flowing into the dump tank when

filling the shock tube. The shock wave is initiated by bursting the primary diaphragm. The Drummond tunnel is designed so that a piercer, actuated when the pressure in the driver is in the range of 3 to 4 MPa, initiates the bursting of the diaphragm (Craddock, 1998). However, for the current experiments, instead of the piercer mechanism, the driver pressure was increased until the stress limit of the diaphragm was reached and the diaphragm ruptured. At that point, a shock wave propagates into the shock tube section. This shock wave, referred to as the *primary shock*, rapidly compresses and accelerates the low-pressure test gas. Behind the shock wave is the boundary between the driver gas and the test gas, referred to as the *contact surface*. The area of the nozzle throat is small relative to the area of the shock tube so that the primary shock wave reflects from the end of the shock tube. The reflected shock causes the gas to stagnate forming a reservoir of high pressure and temperature gas. This then ruptures the cellophane diaphragm and the test gas expands through the nozzle throat and into the dump tank. This process is illustrated by an (x,t) wave diagram in Fig. 4.2. For a particular tunnel condition, an (x,t) wave diagram can be generated using the program L1d (Jacobs, 1998).

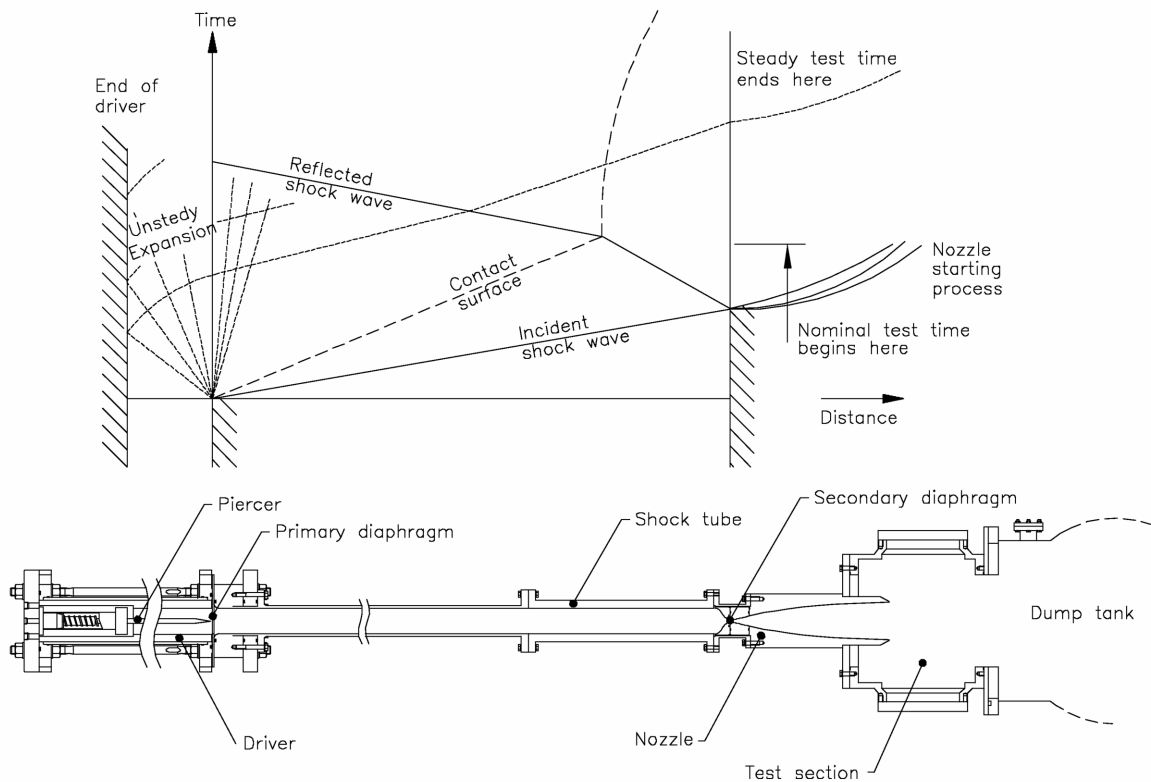


Fig. 4.2. Schematic $x-t$ wave diagram showing the shock and expansion processes in the Drummond reflected shock tunnel (Craddock, 1999).

4.2 The Drummond Shock tunnel

An (x,t) wave diagram, corresponding to the conditions used for the tests in the Drummond tunnel, is presented in section 5.2.

The steady test time ends with the arrival of the reflected expansion from the end of the driver or from an under or over tailoring wave. For a tailored mode of operation, the reflected shock passes through the contact surface without any wave reflections and the nozzle supply pressure remains steady as the contact surface slowly moves towards the nozzle throat. The test time can be reduced due to the interaction of the reflected shock wave and the shock tube boundary layer through the contamination of the test gas slug with the driver gas (Stalker and Crane, 1978).

4.2.1 Models tested in the Drummond tunnel

The sharp and blunted cones and the Muses-C model shown in Fig 4.3 were used to test the feasibility of the BOS technique in the Drummond tunnel.



Fig. 4.3. Models tested in the Drummond Tunnel.

The models tested were not fabricated specifically for the purpose of this study. The 5° spherically blunted nose cone was used by Porter (1996) to study the effects of nose bluntness on the aerodynamic drag on a slender cone. The diameter of the nose tip was 38 mm and the semi-angle θ of the cone was 5° . The Muses-C model is a scaled version

of a Japanese aeroshell. It is a 45° spherical blunted cone. It was renamed *Hayabusa* and its primary mission was to study the near-Earth asteroid, *Itokawa*. The spacecraft was launched in May 2005 and is scheduled to re-enter the earth's atmosphere and land in the Australian outback desert by June 2010. A model of the Muses-C capsule was manufactured at The University of Queensland to study the effects of the atmospheric re-entry heating. The experiments were undertaken in the X1 expansion tunnel and data was verified using the computational fluid dynamics tool, Mb_cns (Jacobs, 1996). The CFD study demonstrated an interesting shockwave shape structure detached to this model and the BOS system is used here to visualise this shockwave in the Drummond tunnel. The sharp 20° half angle cone was 40 mm in height and the base diameter was 29 mm. It was used to assess the sensitivity of the BOS system.

4.2.2 Tunnel Instrumentation

The Drummond tunnel is a small facility compared to the T4 tunnel. Two sensors, a thin-film gauge (TFG) and a pressure transducer, are used to measure the shock speed. The thin film heat transfer gauge (TFG) is mounted flush with the wall of the Drummond tube and is located 295 ± 1 mm from the nozzle end of the shock tube. The TFG consists of a thin platinum film painted onto quartz substrate. A current of approximately 200 mA is passed through the film. The film has a resistance of approximately 50Ω . Once the primary shock wave passes the TFG, heat transfer from the hot, shock-compressed gas causes the surface temperature of the quartz to increase. This causes an increase in resistance of the platinum film and hence a higher voltage drop across the sensor. The time at which this voltage response occurs is noted and is used to calculate the speed of the shock. The pressure transducer is a PCB model 112-A22 piezoelectric sensor. It is mounted flush in the shock tube wall, 75 ± 1 mm from the end of the tube. The pressure transducer is used to obtain another time measurement at which the primary shock wave passes the location of the gauge. The shock speed can be determined from the time difference between the arrivals of the shock at the two sensor locations. The pressure in the nozzle supply region is also measured using the PCB pressure transducer.

4.3 T4 shock tunnel

T4 is a free piston-driven, reflected shock tunnel commonly known as a Stalker tube. The facility consists of a 26 m long compression tube of 230 mm internal diameter and a 10 m long, 76 mm internal diameter shock tube. A diagram of T4 is shown in Fig 4.4. T4 is an impulse-type facility and can produce flows at Mach numbers between 4 and 10 and nozzle supply enthalpies ranging between 2.5 and 15 MJ/kg. The primary diaphragm used in this facility is a mild steel sheet with thickness ranging between 1 and 6 mm. This diaphragm separates the compression tube from the shock tube.

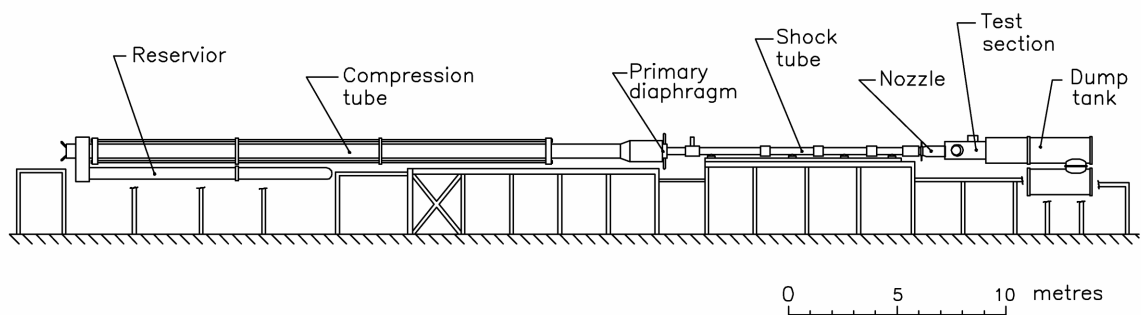


Fig. 4.4. Schematic of the T4 shock tunnel prior to refurbishment in 2000.

Similar to the Drummond tube arrangement, a mylar sheet, placed at the nozzle throat, separates the shock tube from the test section and dump tank prior to firing the tunnel. An 87.5 kg piston is used to raise the pressure in the compression tube to burst the primary diaphragm. High pressure air is released from the reservoir to the space behind the piston. The piston then accelerates freely down the compression tube, compressing the driver gas until the diaphragm ruptures. The reflected shock process is similar to that in the Drummond tunnel. However, to calculate the tunnel conditions, reacting gas mixture processes have to be considered and the Equilibrium Shock Tube Condition (ESTC) (McIntosh, 1968) and the Non-Equilibrium Nozzle Flow (NENZF) (Lordi, 1966) codes are used for this purpose.

4.3.1 Force Measurement on Scramjet model

As discussed in section 4.1, the BOS system was tested in T4 when suitable models were being tested. The experiment that will be described next forms part of Mr Katsuyoshi Tanimizu's Ph.D project. A quasi-axisymmetric scramjet model, as shown in Fig 4.5, was tested to measure the drag of a complete scramjet vehicle in an unfuelled

condition with an aim to model the flow around and through the model and then to investigate a re-design of the thrust nozzle to increase the performance of the vehicle. The model was mounted on a stress wave force balance so that the vehicle's drag could be measured. This force measurement system was developed by Sanderson and Simmons (1991) for T4 shock tunnel applications.

The goal of the flow visualisation tests was to confirm that the intake ducts remained unchoked during the tests. A choked intake decreases the mass flow passing through the combustors and increases the drag. The BOS system was found to be quick and easy to set up compared with other visualisation techniques, such as interferometry.

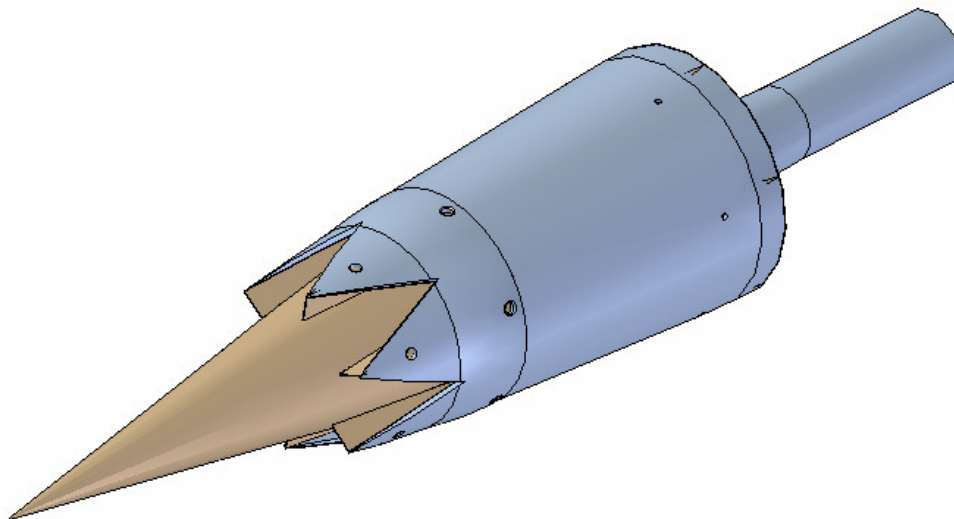


Fig.4.5. Scramjet CAD model showing forebody and cowls (CAD Image: Mr Katsuyoshi Tanimizu).

4.3.2 Materials testing in the T4 Shock Tunnel

BOS was used in T4 during a test campaign by Mr James Turner to determine if models made by sintering a thermoplastic powder material instead of being machined from steel could withstand typical aerodynamic forces and heating loads at scramjet-type test conditions in the T4 shock tunnel. A layered manufacturing process called Selective Laser Sintering or SLS (Nelson et al., 1995) was used to make thin wedges, one of which is shown in Fig 4.7. These were mounted perpendicular to the surface, at the trailing edge of the 250 mm by 150 mm steel flat plate shown in Fig 4.6. The plate was

4.3 T4 Shock tunnel

tested at 0° and 10° angles of attack at free-stream Mach numbers between 6 and 8. A Pitot probe was attached below the plate. This arrangement provided a simple geometry, with both planar and axisymmetric regions of flow, to test the suitability of BOS in the tunnel. The BOS system was setup to focus on the leading edge of the plate and the Pitot probe.



Fig.4.6. Flat plate mounted in T4 test section.



Fig. 4.7. SLS wedge to be mounted at trailing edge of the steel plate.

4.3.3 Flow inside a scramjet duct with leading edge fuel injection

In the third test campaign by Ms Samantha Coras, BOS was set up in T4 to visualise the flow over a flat plate from which hydrogen was injected close to its leading edge. The model consisted of a flat plate set at an angle of attack of 27.1° to the free-stream and an expansion corner at the trailing edge, which would turn the flow through 40° . The model had sidewalls to prevent leakage from the sides of the plate.

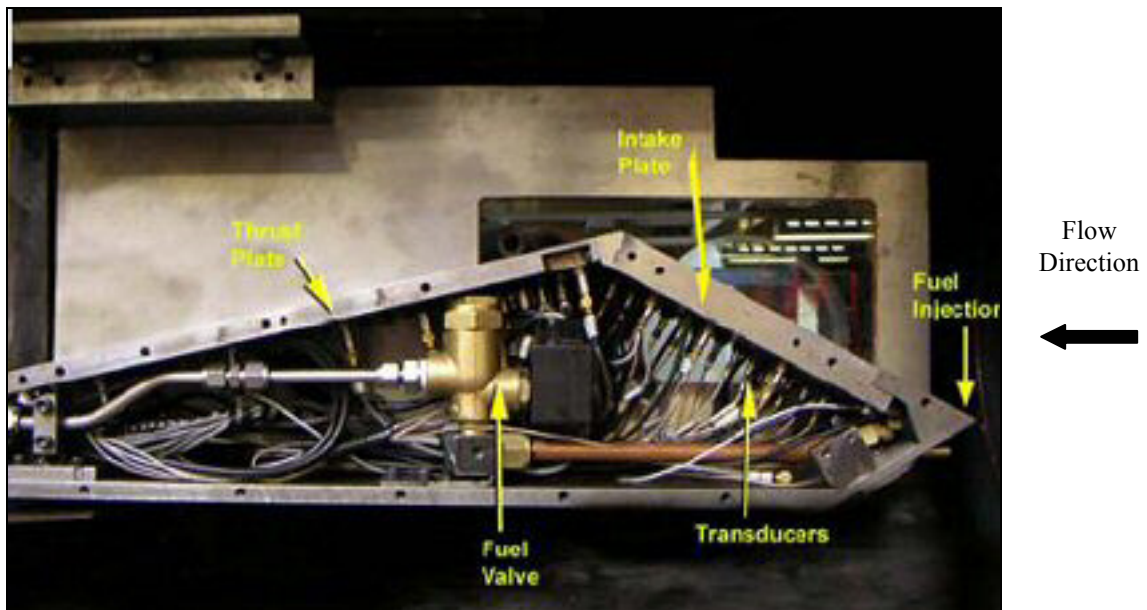


Fig. 4.8. Scramjet duct with one sidewall off to take a photo.

Glass windows were mounted in the sides of the plate to visualise the flow on the compression surface mainly. In Fig. 4.8, one of the side walls was removed. This experiment was devised to investigate fundamental aspects of an external combustion scramjet engine with fuel injected 13 mm from the leading edge. Evidence of fuel combustion was sought from pressure transducers and heat transfer gauges mounted flush to the surface of the plate. For this experimental campaign, BOS visualisation, holographic interferometry and flow luminosity visualisation were used. The interferometric and BOS images were directly compared. For these tests, the region of the flow that could be visualised using BOS in a single shot was limited by the size of the area of the background pattern that could be illuminated by the light source used.

4.3.4 Visualizing the flow at the intake of a REST inlet

A Mach 8 Rectangular-to-Elliptical Shape Transition (REST) inlet with elliptical scramjet combustor was being tested in another test campaign in T4. The BOS system was tested in this campaign by Mr James Turner to visualise the intake region of the engine. Fig. 4.9 shows the model before being placed in the T4 test section.



Fig. 4.9. Mach 8 scramjet engine on bench.

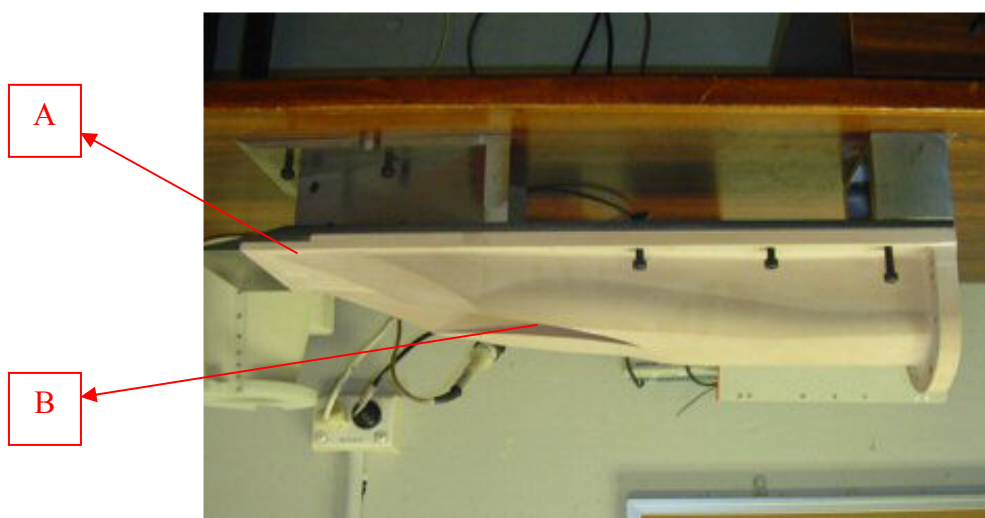


Fig. 4.10. Regions of the model where visualisation was used.

The regions A and B of the model (see Fig. 4.10) were visualised during two separate shots. Fig 4.10 does not show the elliptical combustor.

4.4 The BOS arrangement

A simple BOS setup consists of an electronic camera with a high shutter speed on one side of the tunnel, a high intensity light source and an unstructured dot pattern on the opposite side. A sheet of translucent tracing paper can be used as a diffuser between the light source and the dot pattern.

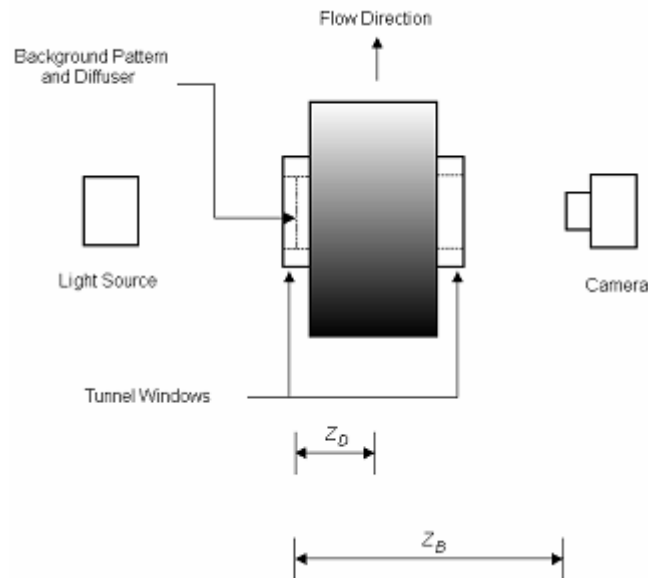


Fig. 4.11. The optical setup for BOS experiments.

A BOS system uses the camera to record two images of the pattern located behind the flow of interest. One photograph is taken when there is no flow and another with flow. The differences between the images are used to infer differences in the refractive index of the medium between the camera and the pattern. Z_D and Z_B in Fig 4.11 are the distances of the background pattern from the test section and the camera lens respectively. These distances can be varied to achieve the right focus and to adjust the sensitivity.

4.4.1 The Background mask

The background pattern is a quasi-random array of dots that is printed on transparency. It can either be placed on one side of the tunnel window or at some distance away from the test section window as shown in Fig 4.11. The background is back illuminated and a lens is used to resolve a focused image on the image plane. A Matlab[®] code, *makerounddotmask.m*, written by Professor Thomas Rösger, (given in Appendix D) was used to generate a dot pattern mask. An example is shown in Fig 4.12. This

algorithm is based on a random number generator program, which places the dots on the pattern in such a way that the dots remain separated and the autocorrelation of the features of the pattern approaches a delta function.

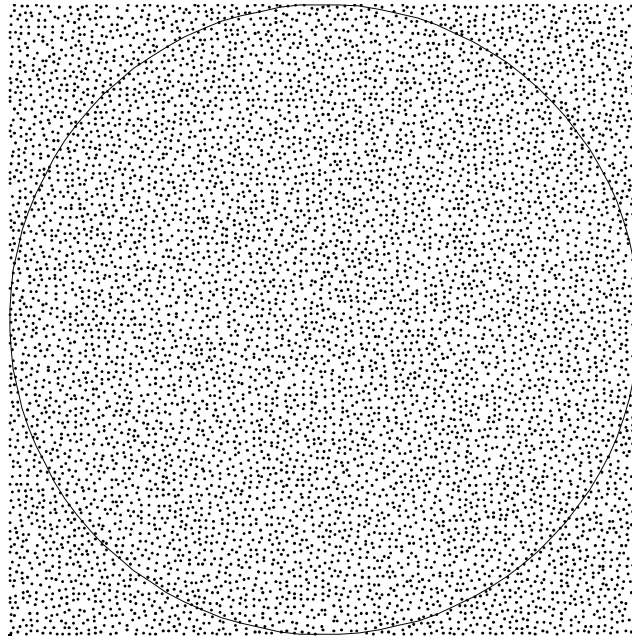


Fig. 4.12. Matlab output of randomly distributed dots of size 0.3 mm.

The random number generator produces a two dimensional array, containing in it the co-ordinates of the dots in the dot pattern. This array of dots is distributed in the pattern in such a way that no dot is placed in a region occupied a 3 x 3 pixel grid surrounding any other dots. To achieve a high contrast when the pattern is back-illuminated, white dots on a black background are desired. This can either be done by inverting the output of Fig 4.12 prior to printing or by choosing to print the negative image. Fig 4.13 is the negative image of Fig 4.12, which has been printed using the postscript driver of the Canon iR5020 laser printer and digitally scanned. The circle corresponds to the diameter of the tunnel window. If the dot mask is to be placed away from the tunnel window, the transparency has to be inserted in between two glass plates, supported by a stand and a tripod.

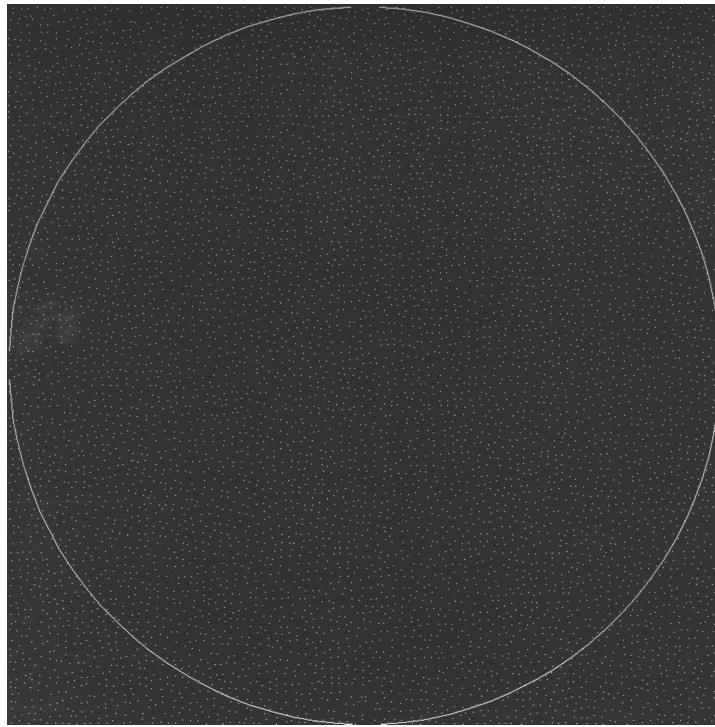


Fig. 4.13. Negative image of Fig 4.10, printed on transparency.

4.4.2 Digital Image recording

The fast development of camera systems has brought about the attractive methods for particle image recordings using solid-state imaging devices such as the CCD (charged coupled devices). This sensor converts light, i.e. photons, into electric charge (electrons) via the photoelectric effect. The CCD chip is a silicon electronic component that is segmented into an array of individual light-sensitive cells or photosites. Each photosite is one element of the whole image, which is usually referred to as a pixel. The size of a pixel of the CCD camera used for the BOS experiments in this thesis was of the order of $10 \times 10 \mu\text{m}^2$. CCD cameras have an analog to digital convertor electronic circuit to convert the voltage generated at a photosite to an integer value. The value depends on the amount of light incident on the photosite during the exposure time. The value at each photosite is stored in an array of $(n \times m)$ locations, where $(n \times m)$ represents the resolution of the CCD chip. The image is then downloaded to a computer. Using standard image processing tools, such as Matlab image Processing toolbox or the Python numeric module NumPy, the image can be read as an $(n \times m)$ matrix containing the pixel values. This matrix is then analysed using the algorithms outlined in section 3.2.

Point Grey Research Inc manufactures the camera shown in Fig 4.14 that was used for the current BOS experiment. This camera uses a black and white version of the Sony 1/1.8" CCD sensor (model ICX274 sensor). The sensor is of the interline progressive scan type meaning that the sensor records an entire image frame at once. The sensor has a maximum resolution of 1600 x 1200 pixels. The camera uses an Analog Device AD9849AKST 12-bit A/D converter. The output signal from the camera can be of either of 8 bits per pixel (8-bpp) depth or of 16-bpp depth digital data. As the bpp increases, the number of quantisation levels for the image increases. This is important for seeing all the essential information in the finely spaced levels of the image. The camera provides an option of a large range of exposure durations depending upon the set resolution.



Fig.4.14. The Scorpion SCOR20S0 (Courtesy: Point Grey Research Inc.) Size: 50 mm X 50 mm X 40 mm Weight: 125 grams.

There is a maximum of 15 frames per second with a 1600 x 1200 resolution corresponding to 66.6 ms exposure duration for one entire frame. However more important for the present applications, the camera has an inbuilt electronic shutter that enables the user to vary the exposure and a single exposure can be taken when a trigger signal is sent to the camera. For a 15 Hz frame rate, the exposure can be set from 0.01 ms to 66.6 ms. Hence, the electronic shuttering capability allows the capturing of high speed flow images. A small shutter opening time enables the user to cut off unwanted light, such as that from flow luminosity caused by impurities in the shock tunnel flows and the high temperature of the flow. This CCD device is reliable over time and requires low maintenance compared to its mechanically shuttered counterpart. The signal to noise ratio for this particular sensor has been determined to be 50 dB or better.

4.4 The BOS arrangement

A Nikon c-mount is used to mount the zoom lens to the camera. It is desirable that the lens has a small lens aperture coupled with a short shutter exposure to enable images of high speed flows to be captured. The lens model used for the Drummond tunnel tests was made by Tokina and had a focal length ranging between 20-80 mm and a minimum aperture of $f/16$.

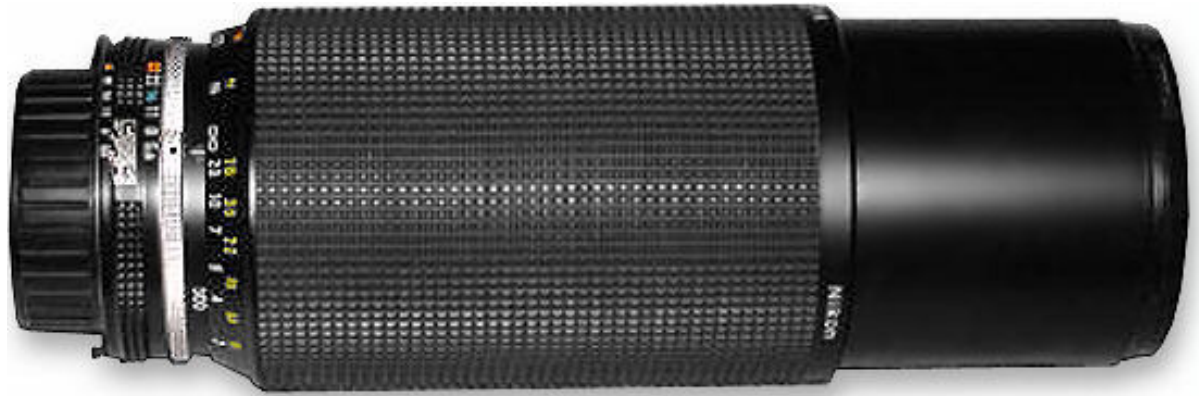


Fig. 4.15. Nikon 100-300 mm, $f/5.6-32$ Zoom lens.

For the T4 tests, a Nikon lens, shown in Fig 4.15 was used. It had a maximum focal length of 300 mm and minimum aperture of $f/32$.

4.4.3 The Background Illumination

For the BOS experiments, a high intensity light source is desirable. In this thesis, a Xenon stroboscope shown in Fig 4.16 was used to illuminate the background pattern behind the flow in the Drummond and T4 shock tunnels.



Fig. 4.16. Xenon stroboscope.

The stroboscope, model Movistrob 400, was manufactured by Bamberg & Bormann, Electronic GmbH. It can generate a maximum light intensity of 550 lux (or lumens/m²), with a pulse width of about 8 μ s. The device has an inherent delay of about 25 μ s to an external trigger.

A constant illuminated halogen lamp was also tested for the preliminary experiments performed at total enthalpies of 3 to 4 MJ/kg in the T4 shock tunnel. At this condition, the luminosity effects in the flow are low and the camera shutter can be opened for a period that allows the illumination from the constant light be fully visible. However, this type of constant lighting emits a high level of heat, which can deform the background pattern mask and diffuser sheets. The halogen lamp was therefore switched on for a short time to record the reference image and a few seconds prior to firing the tunnel, the light was switched back on.

Experimental Results

5.1 Introduction

This chapter presents the results from the Background Oriented Schlieren flow visualisation experiments undertaken in the Drummond and T4 shock tunnels. The purpose of the shots in the Drummond tunnel was to investigate the range of density gradient at low enthalpy conditions where the technique can be utilised and to test the sensitivity of the BOS system at these conditions. The feasibility of using the technique for higher enthalpy conditions, such as those in the T4 shock tunnel for flows typical of scramjet conditions, was investigated next.

The operation of the Drummond tunnel and the conditions used throughout the experimental campaign are given in section 5.2. The flow speed in the tunnel was of the order of 2 km/s in the Drummond tunnel and about 3 km/s in the T4 tunnel. The test times available for such flows were of order milliseconds. To get valid data for BOS image processing, the flow images were captured after flow establishment and within this test time. This was achieved using a fast response pulse generator to trigger the light source and the camera. The inherent delay in the pulse generator was of order nanoseconds and thus was insignificant for tests in both shock tunnels. However, for higher enthalpy tests, where luminosity was present, the lowest shutter speed mode of the camera was used and the electronic delays inherent in the camera and light source were taken into consideration.

For the experiments undertaken in the Drummond tunnel, the signal from a pressure transducer, located in the reflected shock region and upstream from the nozzle was used to trigger the delay generator (which in turn triggered the camera and the light source). The delay between when the primary shock had passed the transducer and when the flow was steady in the test section was determined using an L1d shock tube simulation.

This method of determining the delay before flow establishment can be used for experiments in other shock tunnel facilities.

Section 5.4 of this chapter focuses on the BOS system used to visualise flows around aerodynamic models in the Drummond tunnel. The methods described in Chapter 3 were adopted to analyse the reference and flow images. A conventional schlieren system, as shown in Fig. 2.8, is a line of sight flow visualisation system and the displacement vector results from the BOS system can be used to simulate different knife-edge orientations. Filled contour plots of the horizontal and vertical displacements correspond to the results achieved using vertical and horizontal knife-edge schlieren setups respectively. To the author's knowledge, this processing style has not been attempted before.

It was possible to qualitatively visualise the density gradients associated with the flow around the 20° sharp cone using this new digital schlieren technique in the Drummond tunnel. The feasibility of using this system to resolve higher density gradient regions, such as that around the Muses-C model and the 5° spherically blunted cone, was investigated next. It was also possible to compare the shock stand-off distance measured from the schlieren image of the 5° blunt cone to an empirical correlation.

In the section 5.5, the sensitivity of the BOS system for density gradient visualisation in the Drummond tunnel is investigated. The distance of the background pattern from the image plane was varied and the effect of the latter on the magnitude of the vector displacements was recorded. These vector displacements were computed using the image processing techniques described in Chapter 3.

The results of the visualisation of the flow over scramjet models mounted in the T4 test section follows in the section 5.6.

5.2 The Drummond tunnel operations and tests conditions

The Drummond tunnel operators' manual (Craddock et al., 1998) was followed to run the facility. The shock tube was first evacuated down to approximately 5 torr or less and then filled with 30 kPa of air. The solenoid-activated piercer was not used during these tests but instead, the driver tube was filled with helium until the 0.6 mm aluminium diaphragm ruptured. The burst pressure was 2.75 ± 0.05 MPa. The present condition (30kPa shock tube pressure and 2.75 MPa diaphragm burst pressure) was simulated using L1d (Jacobs, 1998). The $x-t$ diagram, plotted as contours of the logarithm of the pressure, is shown in Fig 5.1. This simulation indicates that the condition is slightly undertailored – note that the contact surface recedes slightly after shock reflection. This simulation was done to determine the time before flow establishment and the approximate test time duration.

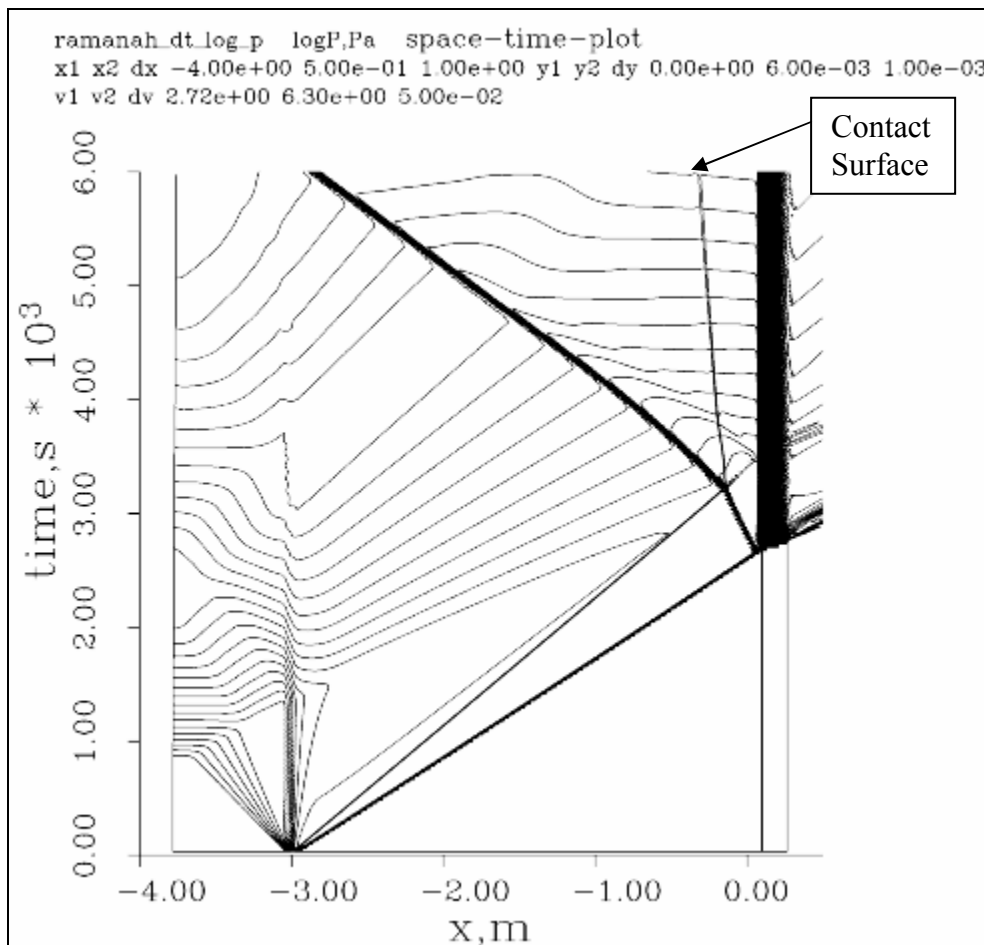


Fig. 5.1. $x-t$ plot calculated using L1d for a viscous simulation.

The pressure of the shock-heated gas pressure supplying the nozzle was measured experimentally using a PCB piezoelectric pressure transducer mounted flush to the inside wall of the tunnel and located 75 mm from the end of the shock tube. This data showed good agreement with a viscous L1d simulation for the primary and reflected shock rise times as shown in Fig. 5.2. However the experimental pressure response differed from the L1d simulation after the reflected shock passed the transducer. This was attributed to the inadequate modelling of the turbulent mixing within the interface in the L1d code. This was also observed by Buttsworth et al. (2006). The free stream conditions were obtained using the package Shock Tube and Nozzle Calculations for Equilibrium air (STN) (Krek and Jacobs, 1993). The nozzle supply pressure, determined from the pressure plot in Fig 5.2, the ambient room temperature, the nozzle area ration and the shock speed were used in this simulation. As noted earlier, a thin-film gauge transducer was mounted 220 mm upstream from the PCB. The data from the two gauges were processed to determine the shock speed used in STN.

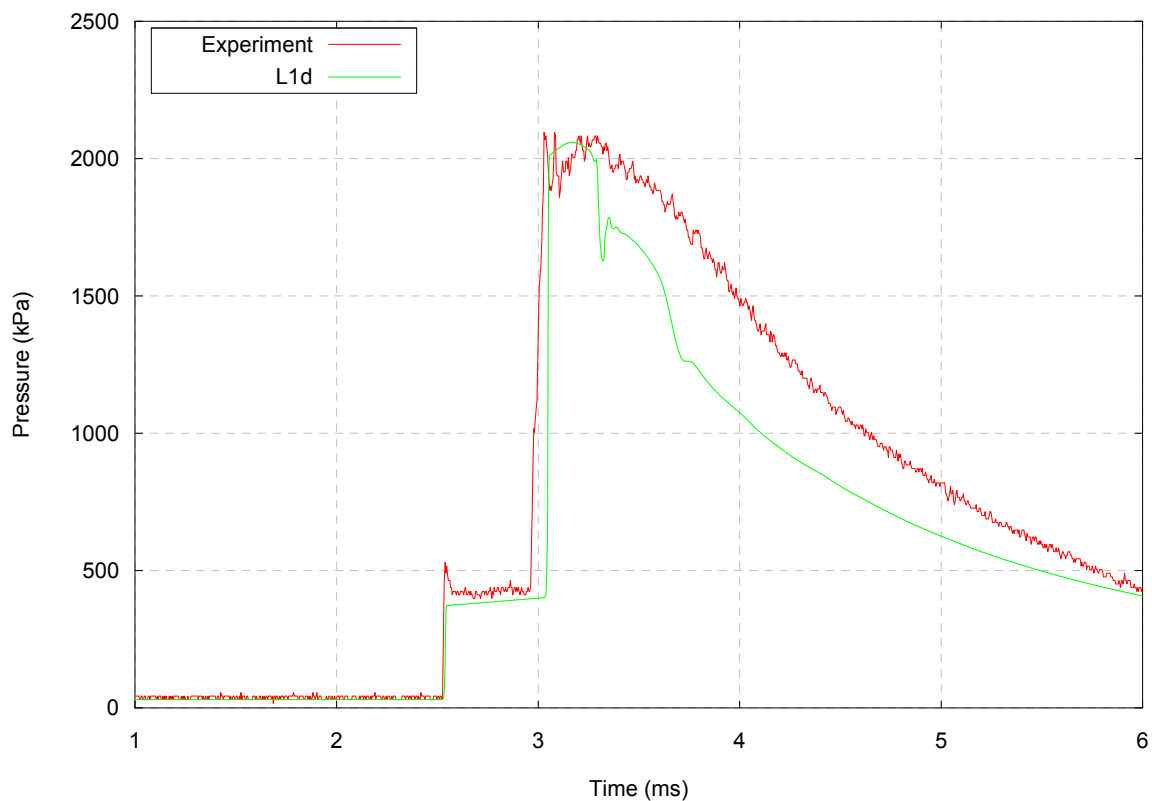


Fig. 5.2. Pressure change due to shock wave.

The STN outputs are shown in tables 5.1 and 5.2. The nozzle area ratio was 10.

5.2 The Drummond tunnel operations and tests conditions

Table 5.1. Stagnation condition at the end of the shock tube.

Parameter	Value
Pressure, p_s (experimental)	2.15 MPa
Enthalpy, h_s	1.76 MJ/kg
Density, ρ_s	4.70 kg/m ³
Speed of sound, a_s	772 m/s

Table 5.2. Free-stream conditions at nozzle exit plane.

Parameter	Value
Temperature, T_∞	453 K \pm 4.5%
Pressure, p_∞	16.9 kPa \pm 12%
Density, ρ_∞	0.130 kg/m ³ \pm 9%
Speed of sound, a_∞	426 m/s
Enthalpy, h_∞	0.450 MJ/kg
Shock speed, U_∞	1610 m/s \pm 1%
Mach Number, M_∞	3.78 \pm 2%

5.3 Triggering the camera and strobe within the test time

To obtain a valid flow image for the BOS analysis, the camera and the light source were triggered during the steady test time, when the flow was established over the model in the tunnel test section. A delay generator was used to time the trigger sequence and was externally triggered using the pressure transducer signal. The delay generator was used to set delays between when the trigger was detected and when the trigger signals would be sent to the camera and the light source. The delay generator had an inherent delay of 85 ns, while the camera and the light source had inherent delays of 25 μ s and 10 μ s respectively. The camera and light source delays were particularly important for synchronising the system when the camera shutter was used in a short exposure mode.

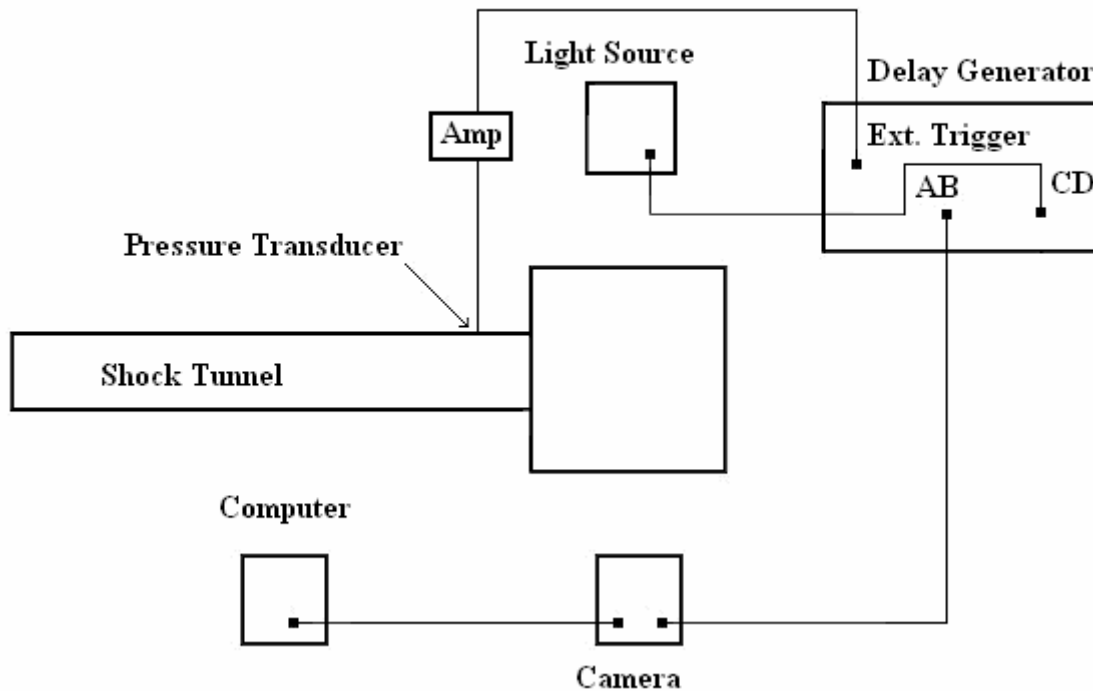


Fig. 5.3. The delay generator connections to the camera and light source.

The block diagram in Fig. 5.3 shows the connections on the devices used for the BOS experiments. The camera was linked to the computer via an IEEE-1394 cable and the *PGR Flycapture* software was used to record the reference and flow image. The settings used in the software and the steps adopted to acquire the images are detailed in Appendix B.

5.3.1 Capturing a flow image for a shutter exposure of 1.0 ms

For the Drummond tunnel experiments, a camera shutter exposure of 1.0 ms was used for all the tests. The pressure rise due to the primary shock wave at the PCB location was used to trigger the delay generator. The delay required between when the shock wave arrived at the transducer location and when the test time started was determined from the $x-t$ diagram in Fig. 5.1. The delay and available test time for this shock tube condition were about 650 μs and 1.3 ms respectively.

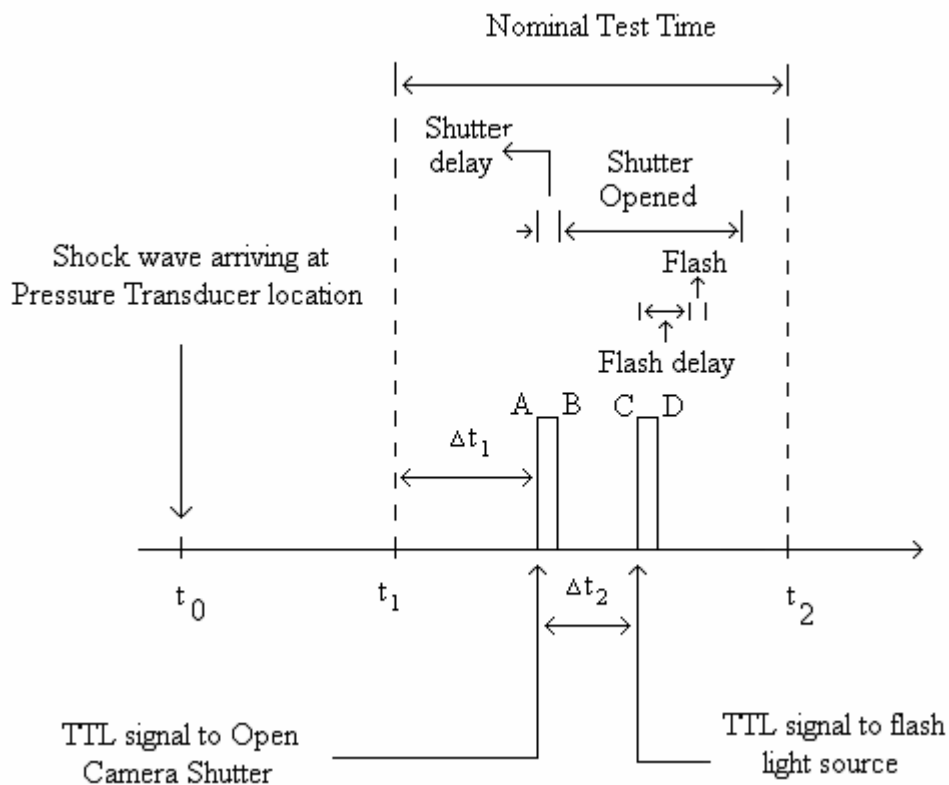


Fig. 5.4. Timing of the trigger signals for a 1.0 ms shutter exposure or above.

The camera was triggered to open its shutter just after the start of the test time and the light source was triggered to flash before the camera shutter was closed. The two TTL signals from the delay generator were timed to fall during the test time (between t_1 and t_2) as shown in Fig. 5.4. The TTL signal was set to a pulse width of 10 μs .

If A and C correspond to the times at which the TTL signals rise and B and D correspond to the times at which the signals fall, the following equations were used to time the triggering relative to the shock arrival time, t_0 .

5.3 Triggering the camera and strobe within the test time

$$A = t_0 + 650 \mu\text{s} + \Delta t_1$$

$$B = A + 10 \mu\text{s}$$

$$C = A + \Delta t_2$$

$$D = C + 10 \mu\text{s}$$

Δt_1 was set to 50 μs while Δt_2 range of values were,

$$0 \leq \Delta t_2 \leq 977 \mu\text{s}$$

for this shutter exposure mode. For smaller shutter exposure times, a different trigger synchronisation was adopted because of the inherent delays in the camera and light source.

5.3.2 Capturing a flow image for a shutter exposure of 10 μs

10 μs is the lowest shutter speed of the Scorpion camera. This setting was used during some of the T4 tests. Some luminosity in the flow at higher enthalpy conditions can be minimized using the short shutter exposure mode. The delay settings on the delay generator were adjusted so that the 8 μs light was flashed during the 10 μs shutter exposure. Because there is a 25 μs delay between the trigger signal and the flash, the light source had to be triggered before the camera was triggered. A schematic of this trigger sequence is given in Fig. 5.5. Δt_1 and Δt_2 were set to 10 and 14 μs respectively for the 10 μs camera shutter mode. The settings were,

$$A = t_0 + 2.5 \text{ ms}$$

$$B = A + 10 \mu\text{s}$$

$$C = A + 14 \mu\text{s}$$

$$D = C + 10 \mu\text{s}$$

For the experiments in the T4 shock tunnel, the signal from a stagnation probe located upstream from the nozzle was used to trigger the delay generator. The time between the pressure rise in the nozzle supply region and when steady flow was established in the test section was set to 2.5 ms in this example. This was determined from data obtained from previous shots at similar conditions.

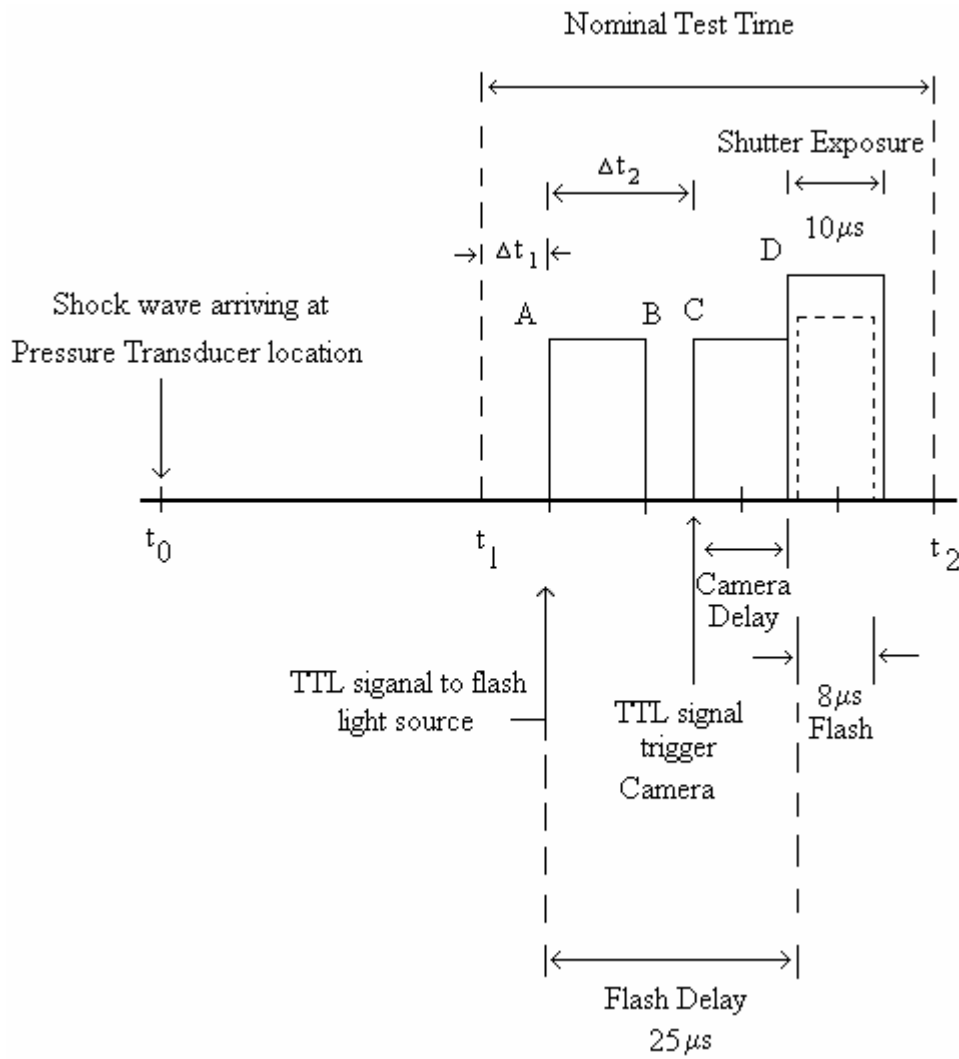


Fig. 5.5. Timing of the trigger signals for a 10 μs shutter exposure.

5.4 The BOS results in the Drummond tunnel

The results obtained using the Background Oriented Schlieren for the qualitative flow visualisation over axis-symmetrical models in the Drummond tunnel are outlined in this section.

5.4.1 Visualizing the Flow over a 20° half angle sharp cone

The BOS results for the Mach 4 flow over the 20° half-angle sharp cone are presented here. The camera was set at a distance of 560 mm from the test section and the background pattern and diffuser were fixed to the test section window. The distance from the outside of the tunnel window to the test section centreline was about 120 mm. Fig. 5.6 shows the reference and the flow images taken for a shutter exposure of 1 ms with a back illuminated dot pattern and a 20° semi-vertex angle circular cone in the foreground. The camera was focussed on the illuminated background dot pattern.

The method described in Chapter 3 to process the images was followed to extract flow information from the two images. The Python Graphical User interface (GUI) program, written specifically for this image-processing task was developed and used. The implementation of the BOS algorithms in this package is explained in Appendix A.

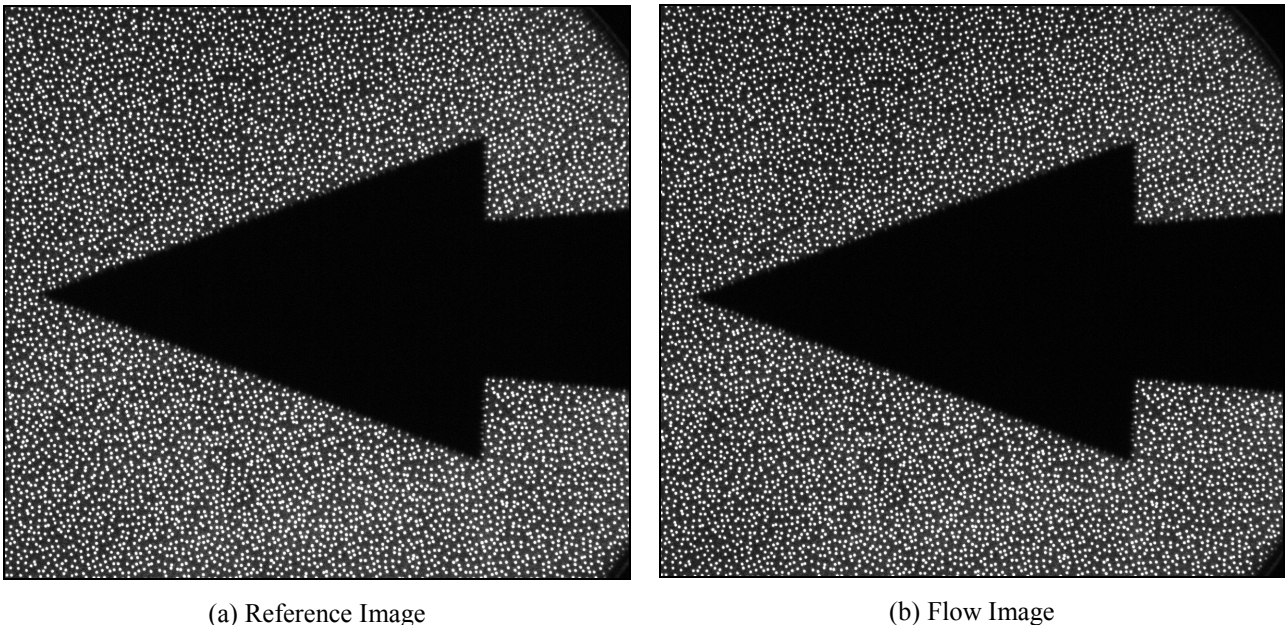


Fig. 5.6. Cone model in the Drummond Tunnel test section, camera-560 mm away from test section with background pattern on the tunnel window.

Some parameters in the image processing such as the correlation window size and the interrogation step size were varied and the effects of those on the resolution of the final results were explored.

The first step in the processing was to correct for undue displacement, caused by the vibration of the tunnel. This procedure is explained in section 3.3.1. The absolute difference between the reference and the corrected flow images, shown in Fig 5.7, can then be generated. The shock wave emanating from the tip of the cone as well as the region around the expansion corner can be seen in this image.

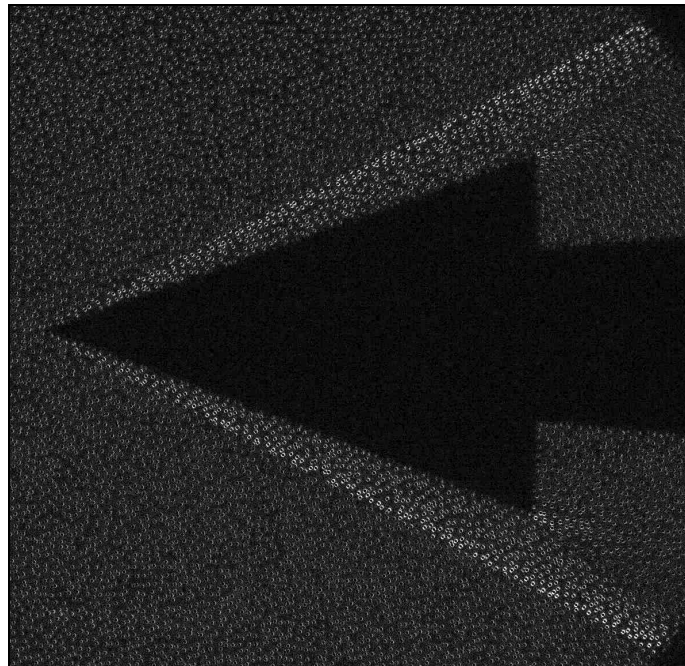


Fig. 5.7. Absolute difference between the reference and corrected flow image.

The vector displacements due to the density gradient change around the cone was evaluated next using the method described in section 3.3.2. The image in Fig. 5.8 shows the vector displacements calculated using a window search size of 32 by 32 pixels and an interrogation step size of 4 pixels. The resultant vectors, represented by arrows were plotted using the *quiver* function in the Python program. These arrows were not distinct in Fig. 5.8 because of their close proximity. However, a coarse search, using a window size of 32 by 32 and step size of 16 pixels resulted in fewer data points, hence fewer arrows as seen in Fig 5.9.

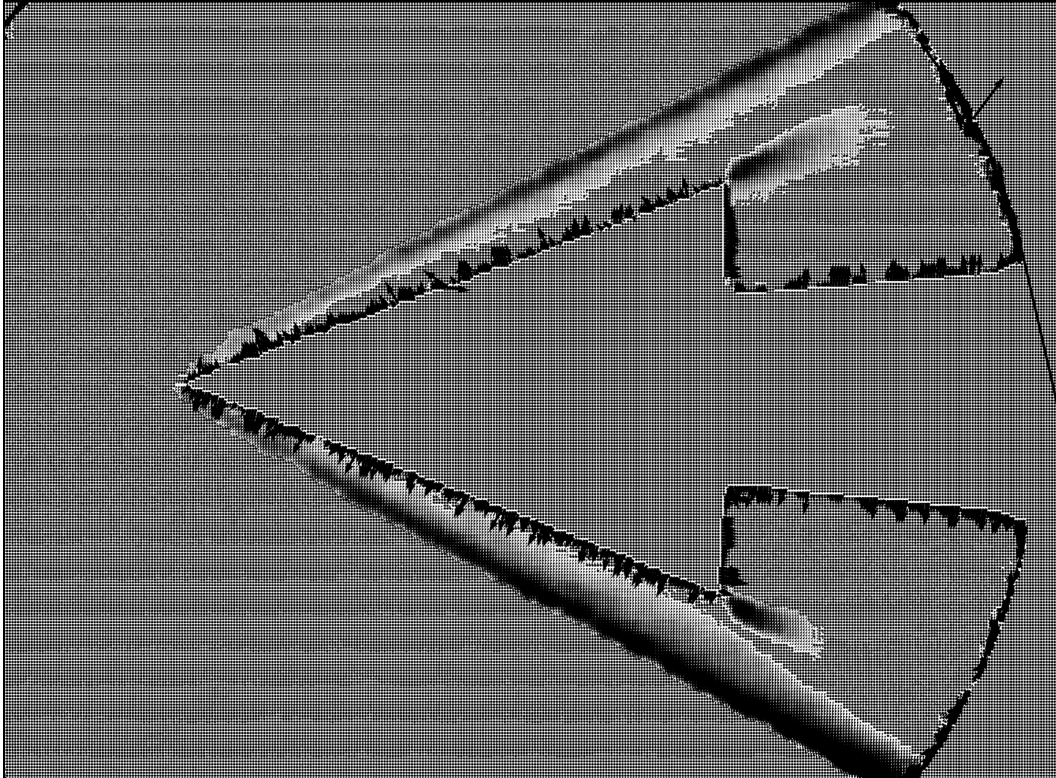


Fig. 5.8. Arrows showing density gradient vectors for a search window size = 32 x32 and step size = 4 pixels.

The erroneous arrows appearing close to the model surface in Figs 5.8 and 5.9 are due to the blur in that region. The camera lens was adjusted to focus on the dots, leaving the model slightly out of focus. The camera lens was however set to the smallest aperture (f16) to achieve the largest depth of field.

Schlieren images were generated using the component vectors obtained from the PIV processing. A filled contour plot of the horizontal and vertical displacements produced the vertical and horizontal knife-edge images, shown in Figs 5.12 and 5.13. The fine correlation search results in Fig. 5.8 were used to generate the schlieren images. A histogram representing the density gradient distributions of the vectors in the flow field was plotted to determine the levels between which to contour the vectors. The histograms representing the vector distributions of Fig. 5.8 are shown in Figs. 5.10 and 5.11.



Fig. 5.9. Arrows showing density gradient vectors for a search window size= 32 x 32 and step size = 16 pixels.

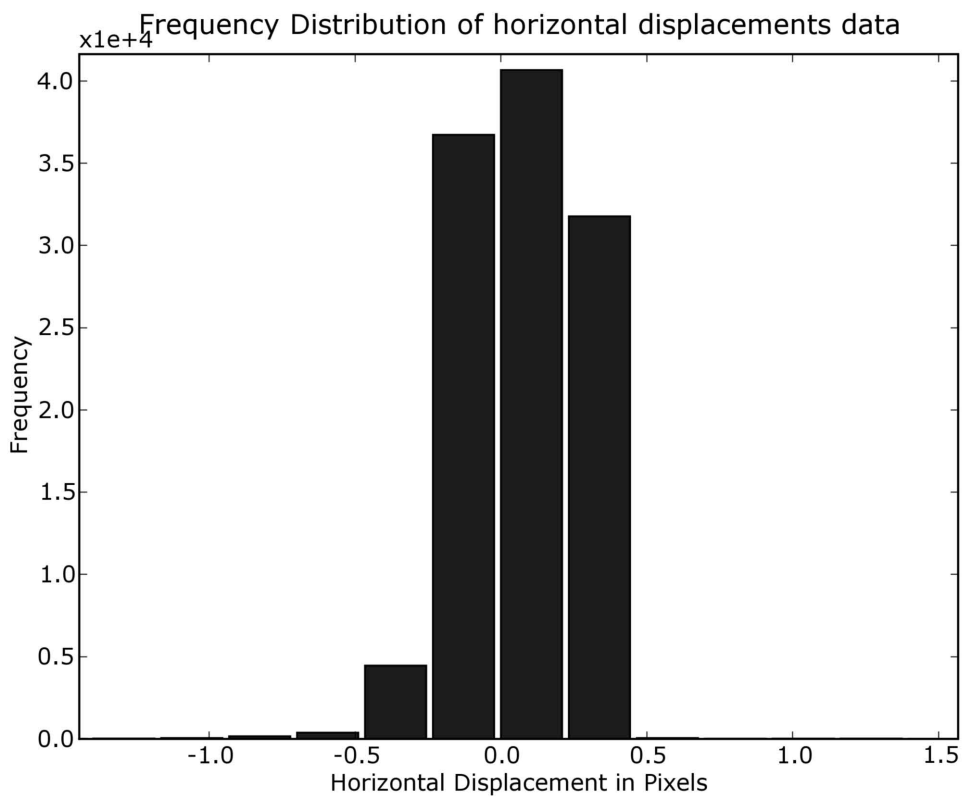


Fig. 5.10. Histogram showing the distribution of the horizontal displacement vectors.

5.4 The BOS results in the Drummond tunnel

From Fig 5.10, it can be seen that the vectors of magnitudes ranging between -1 and 0.5 pixels occur more frequently in the flow field. The vectors in that range were used to generate the vertical knife-edge plot shown in Fig. 5.11. The range of values of the vertical density gradient vectors was between -2 and 2 for this case. The corresponding schlieren image, shown in Fig 5.12, was generated between these gradient levels. Using this method, a good contrast was achieved.

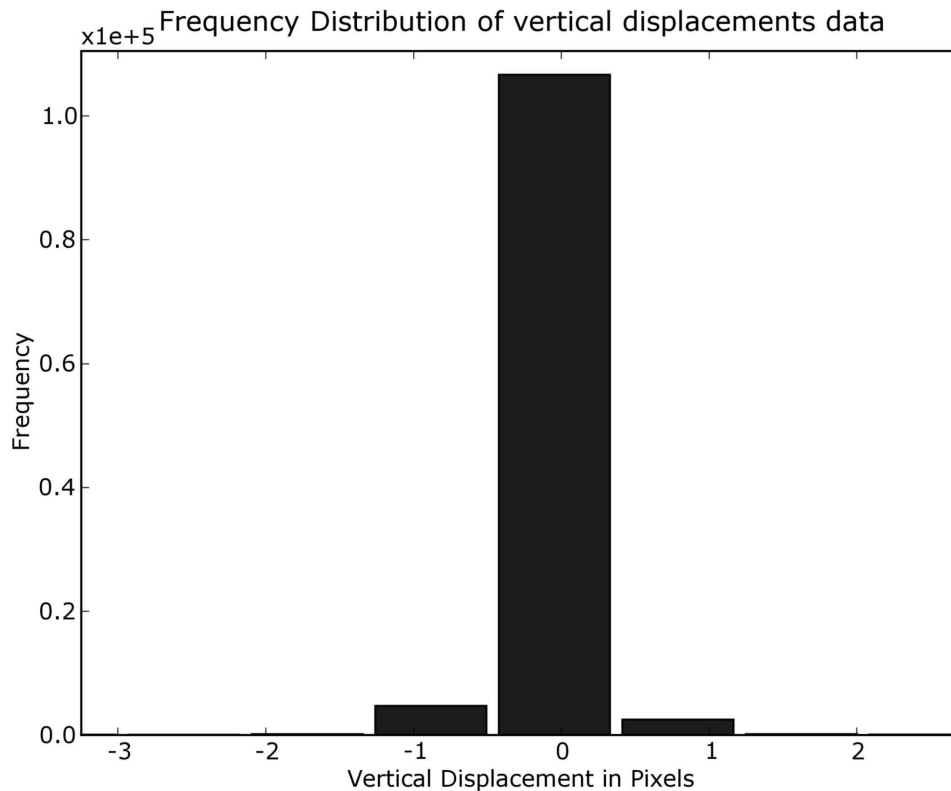


Fig. 5.11. Histogram showing the distribution of the vertical displacement vectors.

The vertical density gradients were reversed from top to bottom and hence reversed the intensity level for a horizontal knife edge case as seen in Fig .5.13. Similarly, a contour plot of the horizontal vectors resulted in the schlieren image, shown in Fig 5.12 with same intensity level on top and bottom.

The sharpness and resolution of the contour plots depends on:

- the resolution of the camera
- the size of the search window
- the size of the step by which the widow moves
- the distance between dots in the background pattern, and
- the magnitude of the displacement of the dots in the flow image.

For the present flow, the best resolution was achieved with a search window size of 32×32 and a step size of 4 pixels. From the image in Fig 5.13, the oblique shock attached to the model is clearly visible. The expansion fan emanating at the base of the cone is also seen. The shock wave appears to start upstream of the tip of the cone. This comes about because of the finite size of the search window. A smaller search window results in the shock starting closer to the tip of the cone. However, too small a search window can lead to no background dots within the window and erroneous results.

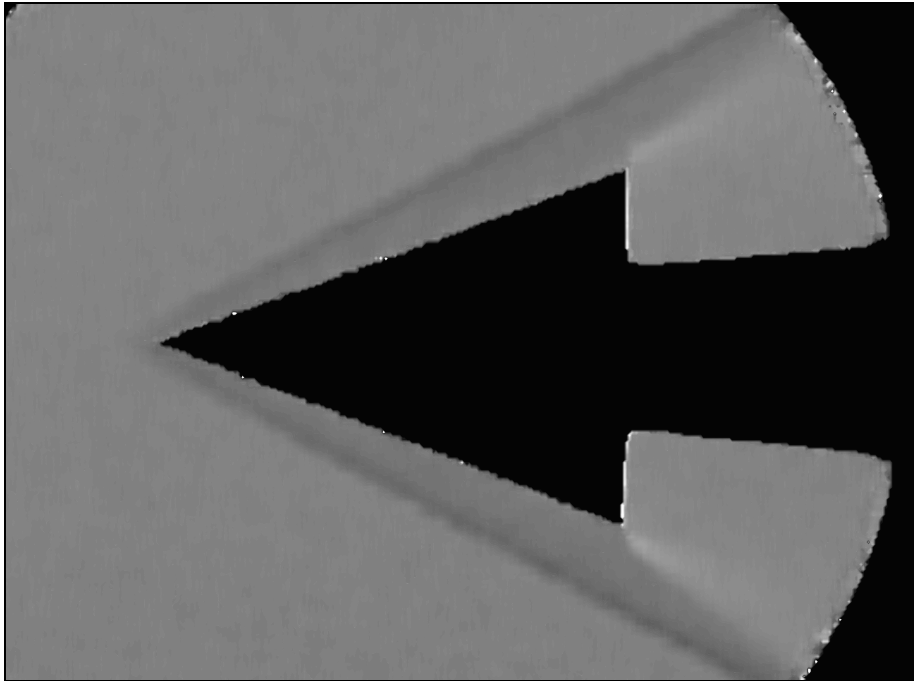


Fig. 5.12. Vertical knife-edge, window size = 32×32 , step size = 4 pixels.

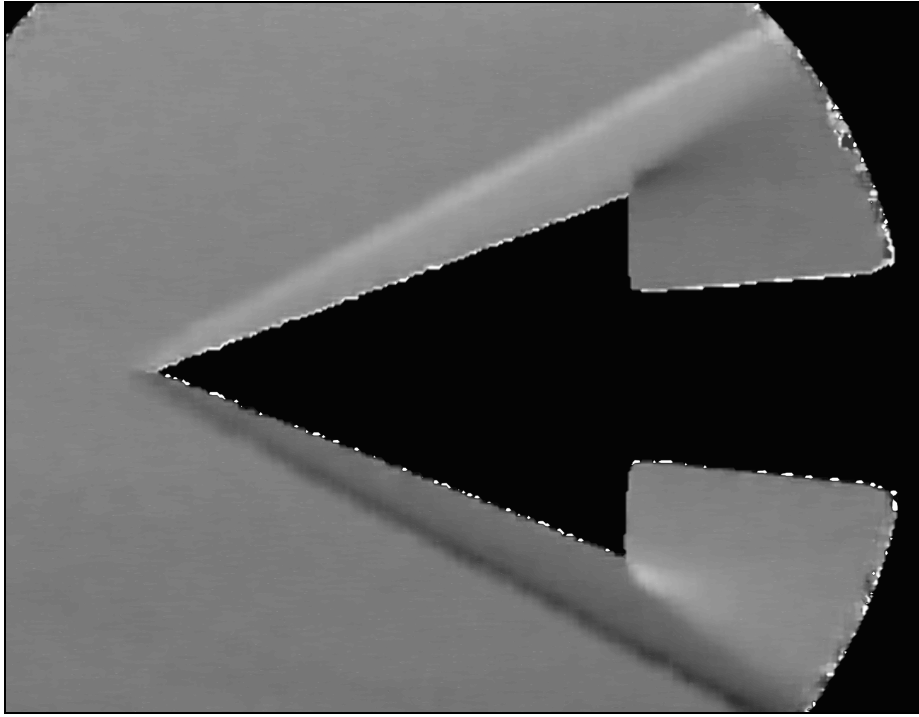


Fig. 5.13. Horizontal knife-edge, window size = 32 x 32, step size = 4 pixels.

5.4.2 Visualizing the flow over the Muses-C capsule

In this section, the BOS image processing technique developed to generate schlieren-like images was used to analyse the reference and flow images for the flow over a scaled model of the Muses-C capsule. In this test, the feasibility of using BOS to resolve the expected higher density gradient region was investigated. The model was mounted in the Drummond tunnel test section and was tested at the flow conditions given in Tables 5.1 and 5.2. The images in Fig 5.14 show the reference and a flow image taken with a camera shutter exposure of 1.0 ms. In the flow image of Fig 5.14 the disturbance caused by the bow shock wave can just be identified as a curved blurred region around the aero-shell. The absolute difference between the reference and the corrected flow image is shown in Fig 5.15. The locations of the bow shock and the expansion near the base of the capsule can easily be identified at this stage of the processing.

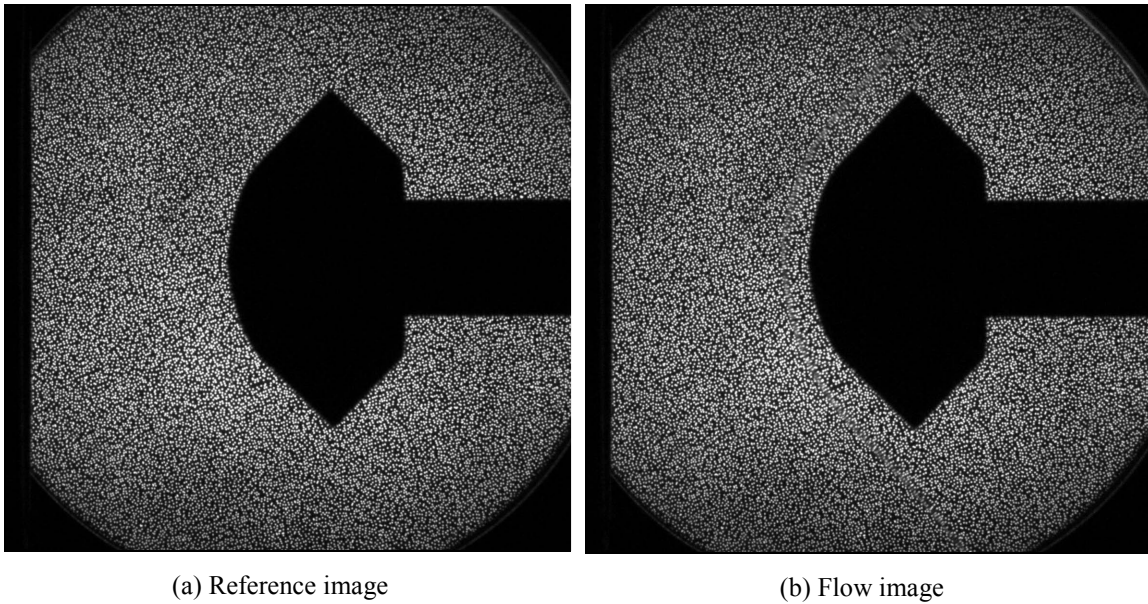


Fig. 5.14. Muses-C model mounted in the Drummond test section, camera-560 mm away from test section, background pattern attached to tunnel window.

In the processing of the images, the correlation window size was chosen such that it was larger than two times the pixel size of one dot. For the density gradient vector plots shown in Fig 5.16, a cross correlation window size of 32 pixels and a step size of 12 pixels were used. A finer cross-correlation computation was performed next using a window size of 32 pixels and a step size of 4 pixels. The corresponding vector plot is shown in Fig. 5.17.

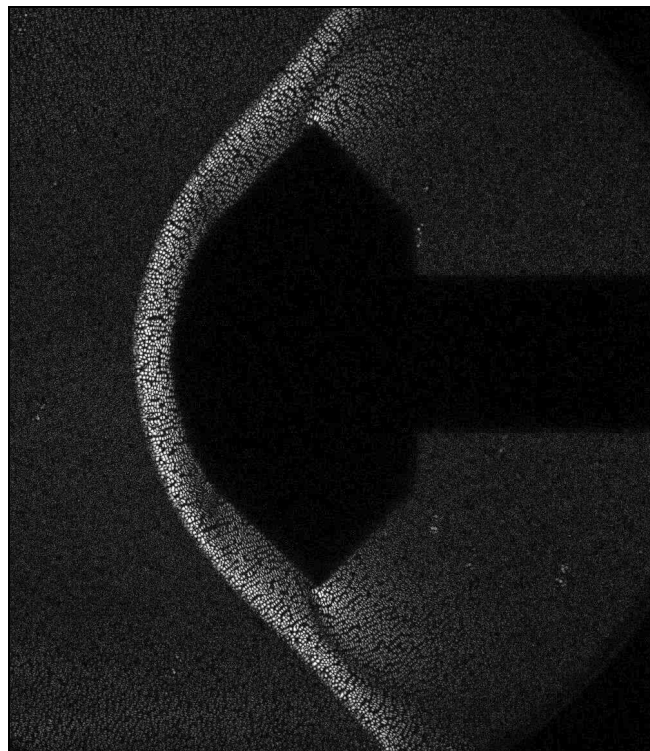


Fig. 5.15. Absolute difference image between the reference and the corrected flow image.

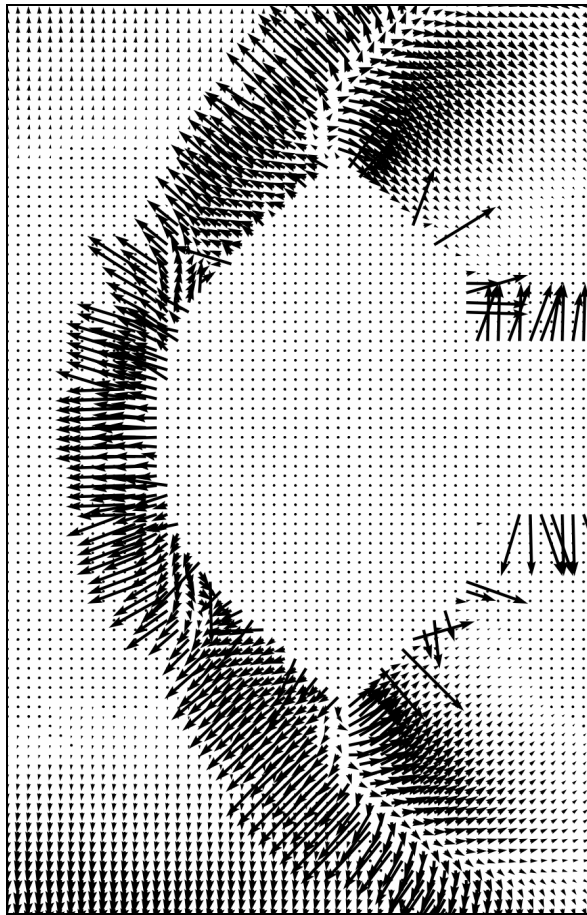


Fig. 5.16. Density gradient vectors obtained with a correlation window size of 32 pixels and a step size of 12 pixels.

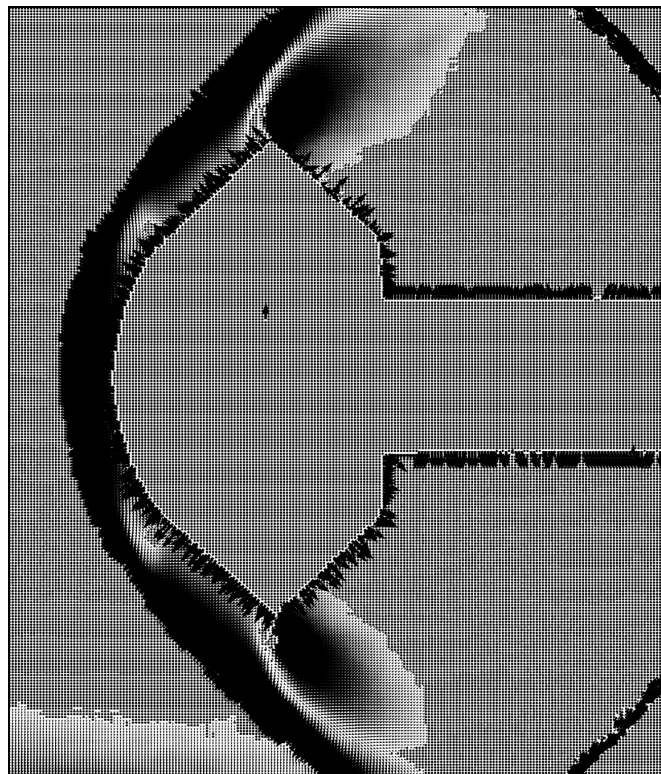


Fig. 5.17. Density gradient vectors obtained with a correlation window size of 32 pixels and step size of 4 pixels.

A similar method as employed for the flow over the cone model was employed for the Muses-C model to determine the range between which to generate contour plots. The vectors in the fine correlation computation of Fig. 5.17 were used to generate the schlieren images in Fig. 5.18 and 5.19.

The bow shock, curved around the Muses-C model is clearly visible in both schlieren images and the shock stand-off distance can be measured from the images. A thin saturated region within the shock layer can be observed in both schlieren images. This occurred because the flow image was blurred in the shock layer, as can be seen in Fig 5.20. When the size of the cross-correlation was of the order of the size of the blurred region, the cross correlation routines do not identify a dominant peak to enable the magnitude of the background displacement to be found near regions of blurring. The BOS analysis routines set the grey levels to zero in those regions and thus there is a black band near the shock in Figs 5.18 and 5.19. This effect could be reduced by increasing the size of the cross-correlation window (for example, using 64 x 64 instead of 32 x 32 pixels). However, this reduces the sharpness of the BOS image obtained.

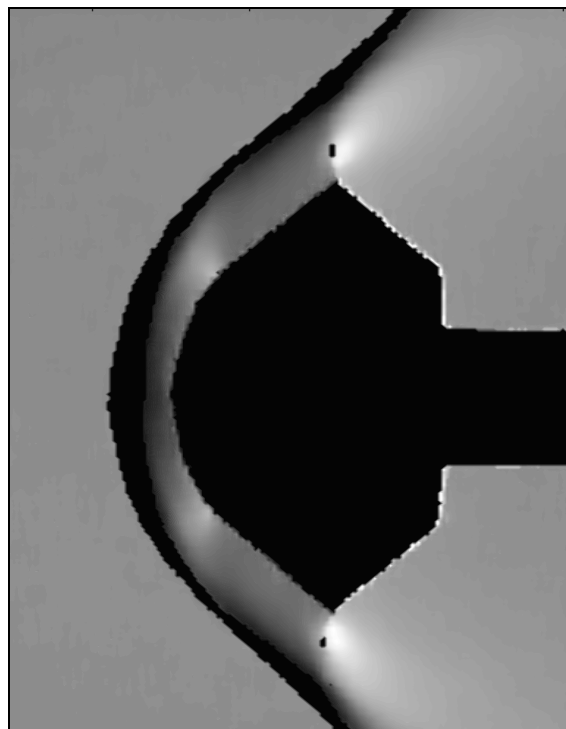


Fig. 5.18. Vertical knife-edge generated using vectors from a cross-correlation window size of 32 x 32 pixels and a step size of 4 pixels.

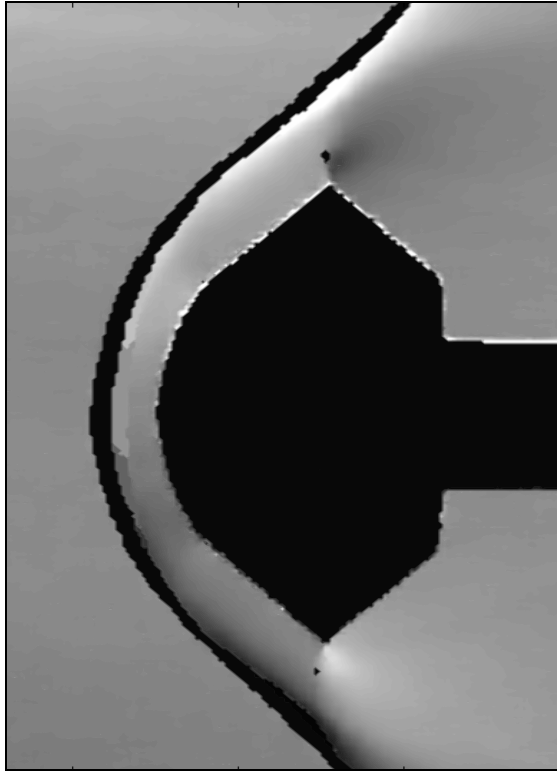


Fig. 5.19. Horizontal knife-edge generated using vectors from a cross-correlation window size of 32 x 32 pixels and a step size of 4 pixels.

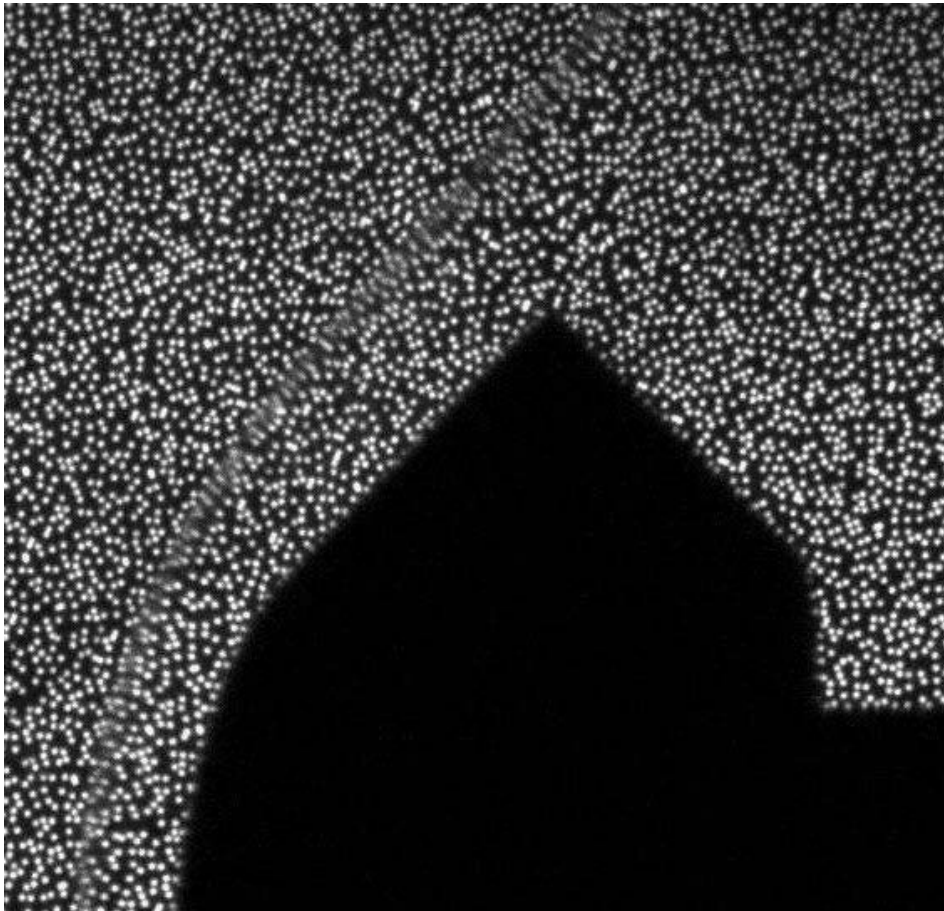


Fig. 5.20. Cropped portion of the Muses-C flow image showing thin saturated layer.

5.4.3 Visualizing the flow over a 5° blunted cone

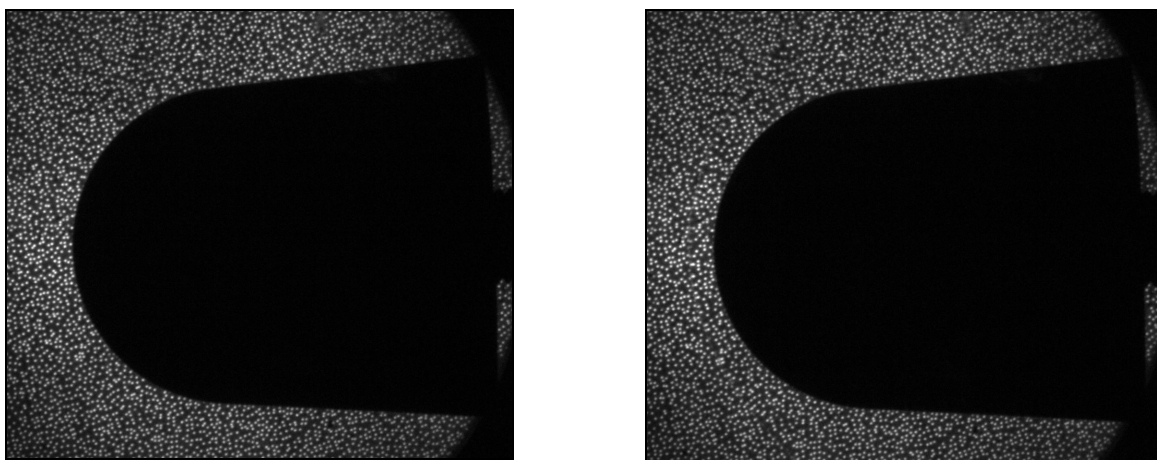
The BOS system was next tested for the flow over a 5° blunted cone in the Drummond tunnel and an attempt to compare the results to a theoretical shock stand-off distance was made.

Billig (1967) formulated a correlation for shock stand off for sphere-cone models. The correlation is,

$$\frac{\delta}{R} = 0.143 \exp[3.24 / M_\infty^2]. \quad (5.1)$$

This equation relates the shock stand-off distance on the axis of symmetry, δ , to the radius of the nose cone, R , and the free-stream Mach number, M_∞ . This stand-off distance measured from the BOS image in Fig. 5.24 was 7 mm \pm 0.5 mm. The experimental free stream Mach number was evaluated using the measured stand-off distance in equation 5.1. The Mach number was 3.6 \pm 4%. The theoretical free-stream Mach number evaluated using the STN software was used in equation 5.1 to calculate the theoretical shock stand-off distance. The theoretical shock stand-off distance was 6.82 mm and agreed with the experimental uncertainty.

The reference and flow images shown in Fig. 5.20 were used in the BOS evaluation. The absolute difference image in Fig. 5.21 clearly shows the bow shock shape curved around the sphere-cone. A 36 x 36 pixels correlation window size and a step size of 4 pixels were used to determine the density gradient vectors shown in Fig 5.23. The corresponding schlieren images were generated and are shown in Figs. 5.24 and 5.25.



(a) Reference image

(b) Flow image

Fig. 5.21. Sphere-cone mounted in the Drummond test section.

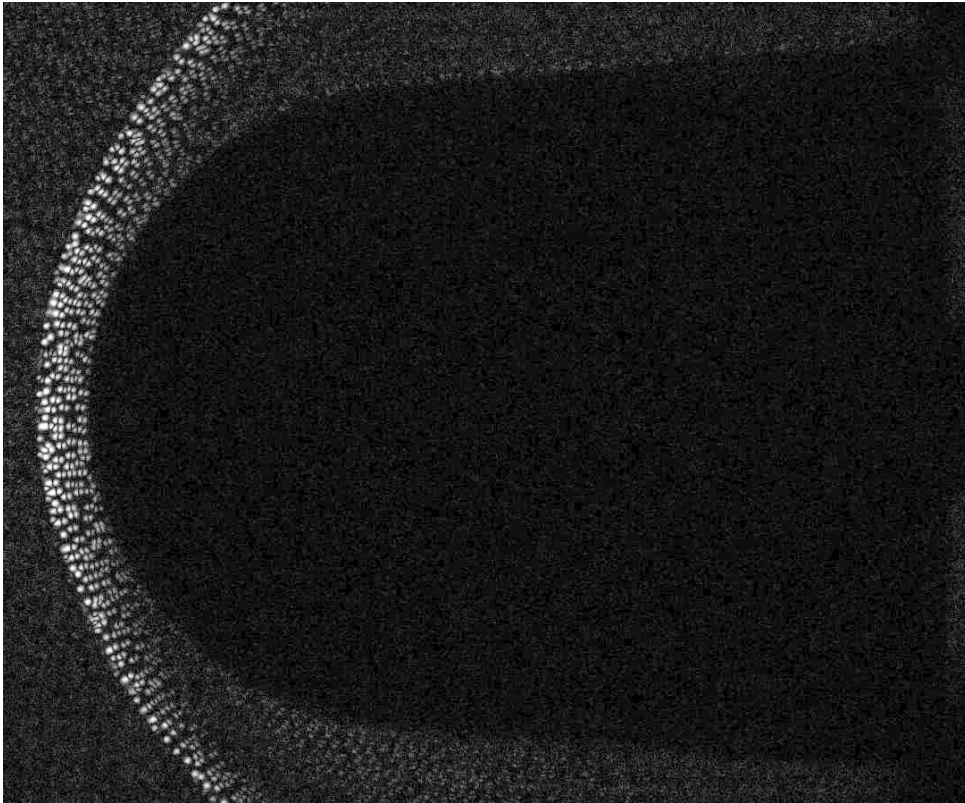


Fig. 5.22. Absolute difference between reference and flow image.

A thin, saturated region near the bow shock wave, similar to that observed for the Muses-C case, can be seen in the horizontal knife-edge and vertical knife-edge images in Figs. 5.24 and 5.25.

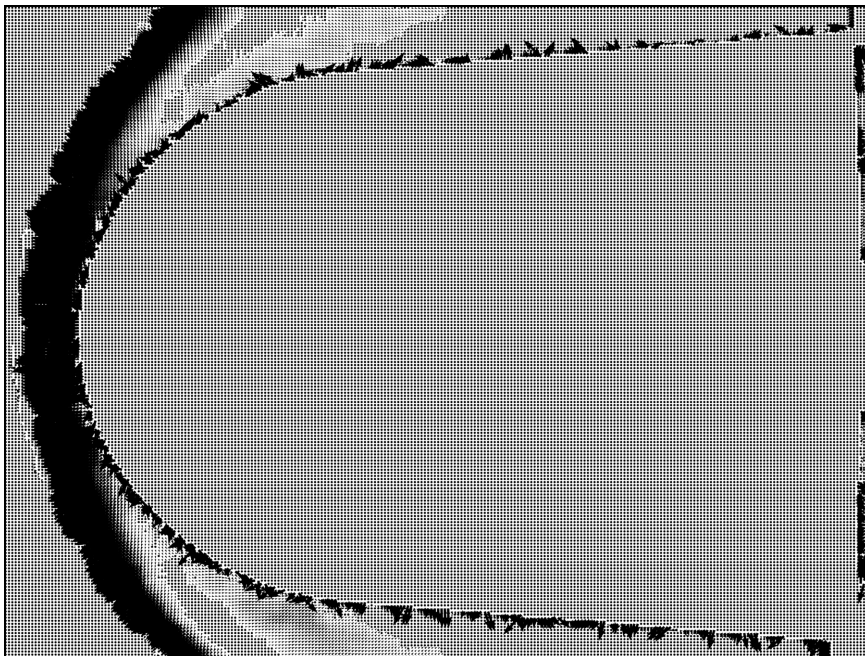


Fig.5.23. Density gradient vectors in the bow shock layer, window size 36 x 36 and step size 4 pixels.

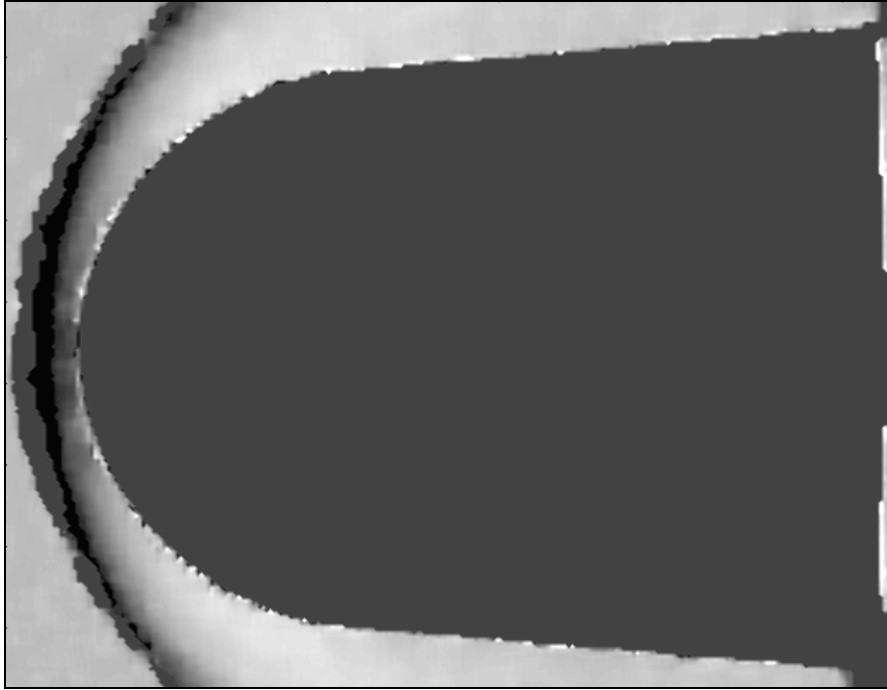


Fig.5.24. Vertical knife edge schlieren.

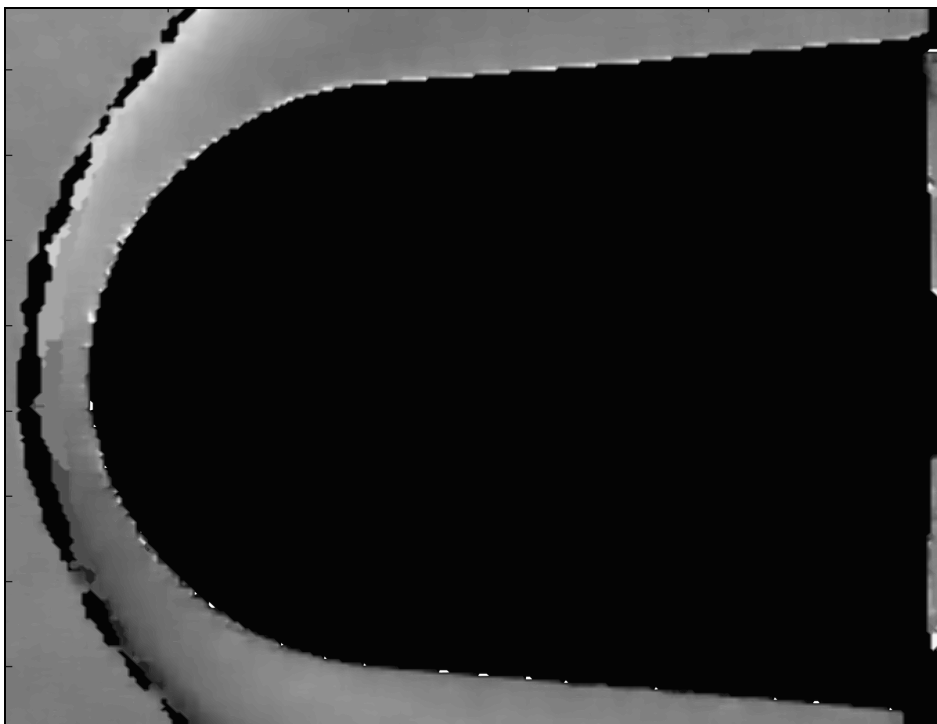


Fig.5.25. Horizontal knife edge schlieren.

5.5 The sensitivity of BOS for visualizing compressible flows

In this section, the results of the tests using the sharp cone to evaluate the sensitivity of the BOS system in the Drummond tunnel are presented. An equation relating the density gradient to the displacement at the image plane due to density gradients was formulated. This equation was used to determine which parameter to alter in the BOS optical setup to achieve a higher sensitivity.

If a 2-D flow field is assumed, the gradient of the refractive index will be constant along the optical path. With reference to Fig 2.17 (page 23), the image deflection angle, ε , can be defined as

$$\varepsilon = \frac{1}{n_0} \int_{z_D - \frac{W}{2}}^{z_D + \frac{W}{2}} \frac{\partial n}{\partial y} dz . \quad (5.2)$$

This formula is valid for small deflection angles. Because the beam traverses the medium at small angles relative to the optical axis, the length of the optical path can be taken to be equal to the width of the region with density variations, W , and the deflection angle becomes

$$\varepsilon = \frac{1}{n_0} W \frac{\partial n}{\partial y} . \quad (5.3)$$

Using the Gladstone-Dale equation and assuming that n_0 is small, the deflection angle equation reduces to

$$\varepsilon = K W \frac{\partial n}{\partial y} . \quad (5.4)$$

The width, W , can be subdivided and the gradient normal to deflected beam is evaluated at each step as shown in Fig 5.26. For n steps,

$$\varepsilon = (\varepsilon)_1 + (\varepsilon)_2 + \dots (\varepsilon)_n . \quad (5.5)$$

The PIV estimate of the pixel displacement for a particular sub-window corresponds to the beam displacement, Δy , as shown Figs 2.17 and 5.26. With the combination of the total deflection angle, ε , the optical path geometry equation (McIntyre, 2005),

$$\varepsilon = \frac{\Delta y(Z_B - f)}{Z_D f} \quad (5.6)$$

and the Gladstone-Dale relation (equation 2.4), a generic equation can be formulated to relate the density gradient to the beam displacement,

$$\left[\frac{\partial \rho}{\partial y} \right] = \frac{Z_B - f}{Z_D K f W} [\Delta y], \quad (5.7)$$

where K is the Gladstone-Dale constant and f is the focal length of the camera lens.

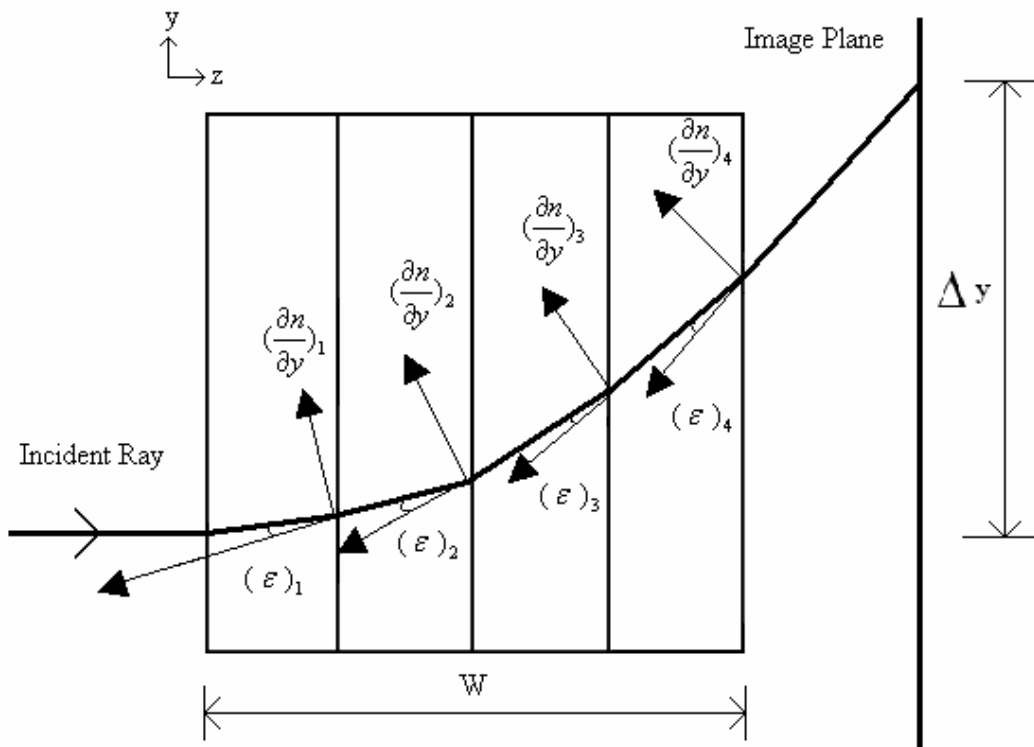


Fig.5.26. Optical path of a light beam through a constant density gradient region.

From equation 5.6, it can be seen that an increase in Δy is possible when the background pattern is moved further away from the density gradient region. The camera lens then has to be adjusted or the distance Z_B changed to ensure that the background pattern remains in focus. The sensitivity of the system is defined here as $\left[\frac{\Delta y}{\partial \rho / \partial y} \right]$. The

sensitivity depends mostly on the focal length of the lens used, the relative position of the object between camera and background and the smallest detectable shift in the image plane.

5.5 The sensitivity of BOS for visualizing compressible flows

Adjustment of the sensitivity by changing the distance Z_D and Z_B was demonstrated experimentally. Figs 5.9 and 5.27 show the density gradient vector results obtained in two experiments with the background pattern set at different distances. In Fig 5.9, the distances, Z_D and Z_B were 225 mm and 1010 mm. Z_D and Z_B were 1365 mm and 2750 mm for the higher sensitivity vector results shown in Fig 5.27. 1365 mm was the maximum distance the background pattern could be moved away from the test section and be possible to focus clearly on the pattern. The 28-80 mm focal length lens was used in the low sensitivity test and in the enhanced sensitivity case, the longer 100-300 mm focal length lens was used. The correlation window search size was 36 pixels and the interrogation step was 16 pixels for both tests.

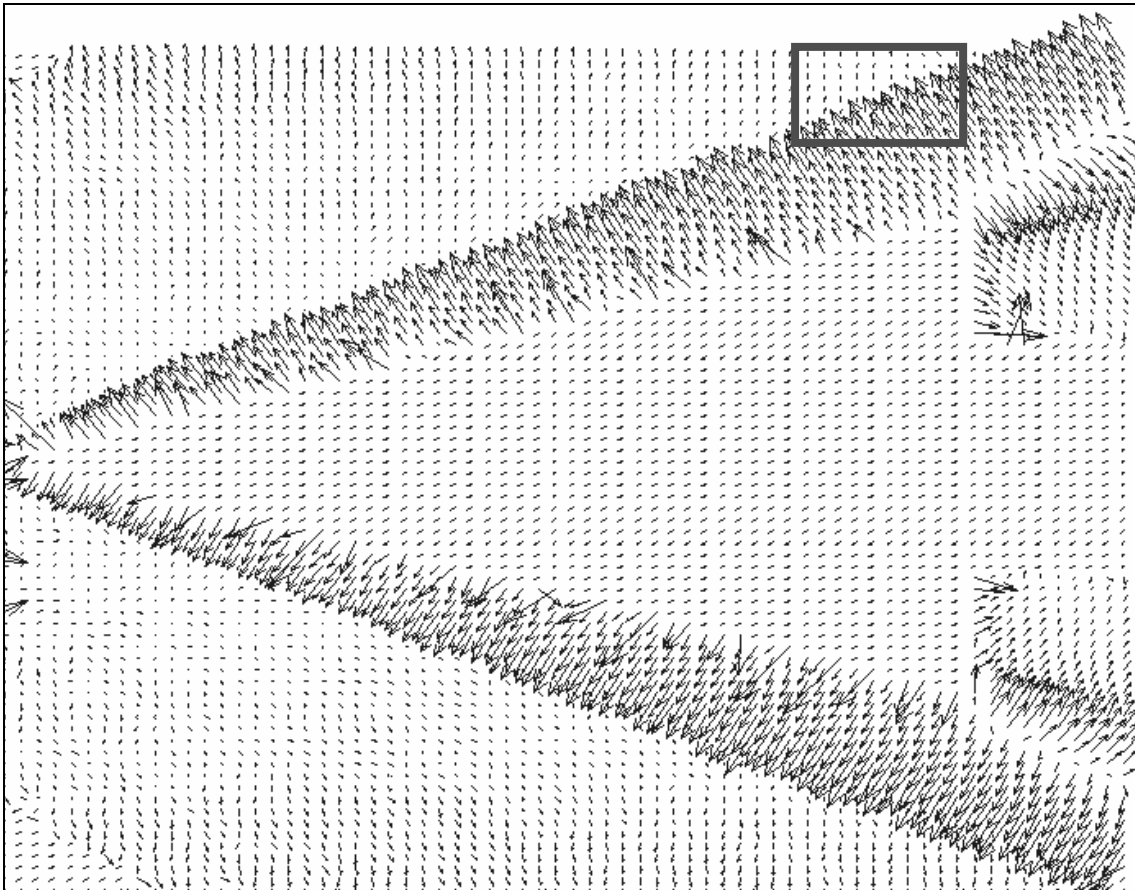
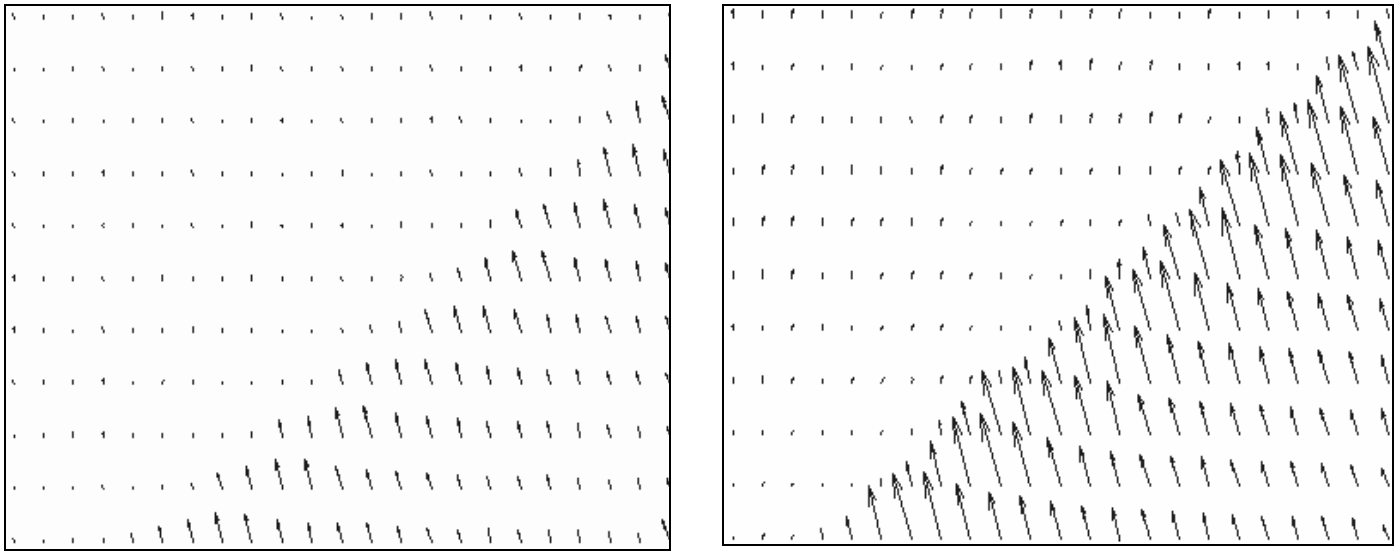


Fig. 5.27 Increased sensitivity of the BOS system.

The region shown in Fig 5.27 was selected at the same location in both vector plot results. The vectors contained in the two regions plotted on a larger scale can be seen in Fig 5.28.



(a) Low sensitivity Case

(b) High Sensitivity Case

Fig. 5.28. Increased sensitivity of the BOS system.

The average values of the vertical and horizontal displacement vectors in both cases were determined and are shown in Table 5.3.

Table 5.3. Average vector values in the selected region.

	Average Horizontal Vector Values	Average Vertical Vector Values
Low Sensitivity	-9.95×10^{-5}	2.86×10^{-4}
High Sensitivity	-2.51×10^{-4}	7.31×10^{-4}
Gain in Sensitivity	2.52	2.56

It can be seen in Table 5.3 that the sensitivity was increased by a factor of 2.5.

Equation 5.7 can be used to theoretically calculate the gain in sensitivity,

$$Gain = \frac{Z_{D_2}}{Z_{D_1}} \cdot \frac{f_2}{f_1} \cdot \left[\frac{Z_{B_1} - f_1}{Z_{B_2} - f_2} \right] \quad (5.8)$$

where the superscript 1 corresponds to the low sensitivity case while 2 corresponds to the high sensitivity case. The focal lengths of the lenses f_1 and f_2 used during the two experiments were 60 mm and 250 mm. The calculated gain in sensitivity was determined to be of a factor of 9.7. It is clearly seen that an increase in sensitivity was possible by increasing the camera and dot pattern distances from the test section while adjusting the focal length of the lens. Even accounting for experimental uncertainty, the magnitude of the gain in sensitivity determined experimentally was approximately four times less than the theoretical gain. At the time of writing this thesis, it was not possible to identify the cause of this difference.

5.6 BOS results in the T4 shock tunnel

The Background Oriented Schlieren technique applied to the T4 free-piston reflected shock tunnel is presented in this section. The BOS technique was used during the four test campaigns, outlined in section 4.3. Through these experiments, it was possible to test the BOS system to qualitatively visualise the flow over scramjet models and components of scramjets. A similar setup to that implemented in the Drummond tunnel was employed for the T4 tests. The background dots and diffuser were placed on the tunnel test section window ($Z_B = 2.6$ m) and the camera was at a distance of 2.3 m from the test section.

5.6.1 Using BOS to visualise a scramjet model intake

BOS was tested for the first time in T4 during the campaign conducted to measure the drag of a complete scramjet vehicle. For this campaign, the camera and light source were mounted on two tripods on either side of the tunnel. This setup was not very stable and this resulted in large displacement between the flow and reference images due to the movements between the no-flow and flow photographs. For the other test campaigns however, the camera and the light source were mounted on the optical tables as shown in Figs 5.29 and 5.30. This improvement in the setup minimized image displacements. With this arrangement however, it was not possible to adjust the sensitivity between shots.

Before conducting the BOS tests, a luminosity image of the flow during the test time was taken with the Point Grey Research camera. The camera shutter was set to expose for 1 ms during the 2.5 ms available test time. The image obtained was then enhanced using the *Automatic Contrast Adjustment* function in Paint Shop Pro software. The image is shown in Fig 5.31.

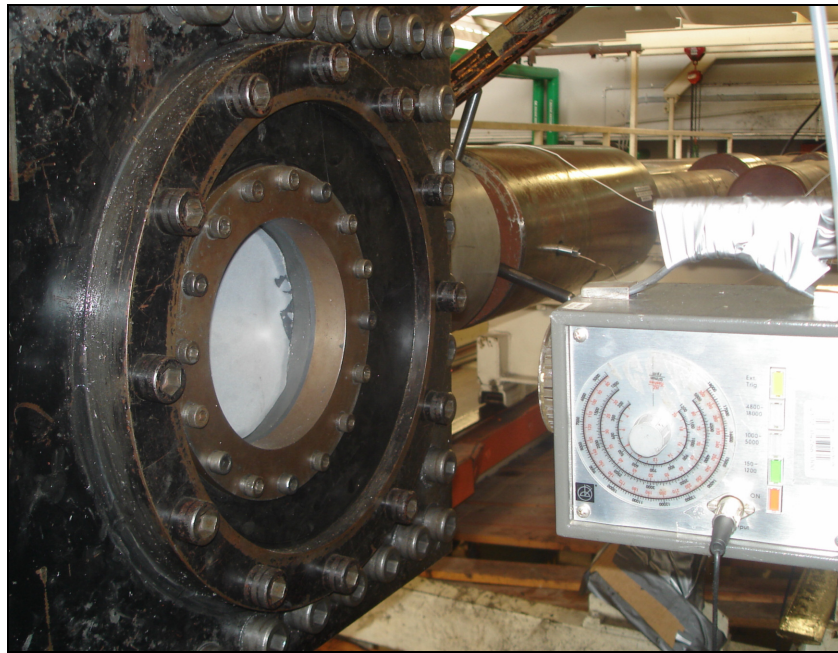


Fig. 5.29. Light source placed on one side of the tunnel and mounted on the optics table.

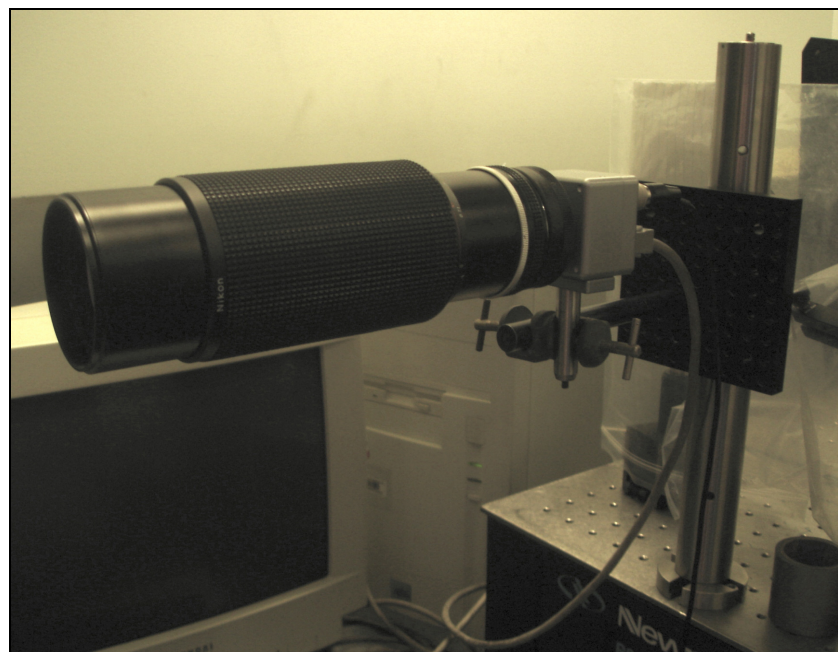


Fig. 5.30. The camera and lens mounted on the optics table next to T4 opposite to the light source.

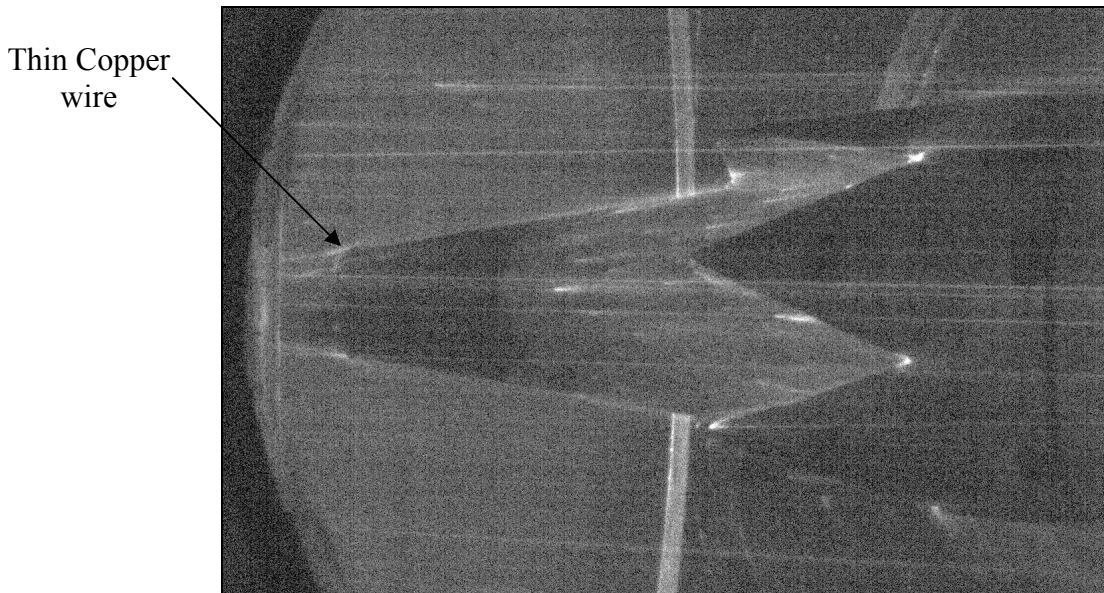


Fig. 5.31. Scramjet Model shot 8768, $p_s = 33.8$ MPa, $h_s = 2.54$ MJ/kg, $M_\infty = 8.3$, $p_\infty = 2.1$ kPa, $U_\infty = 2.2$ km/s, $T_\infty = 173$ K.

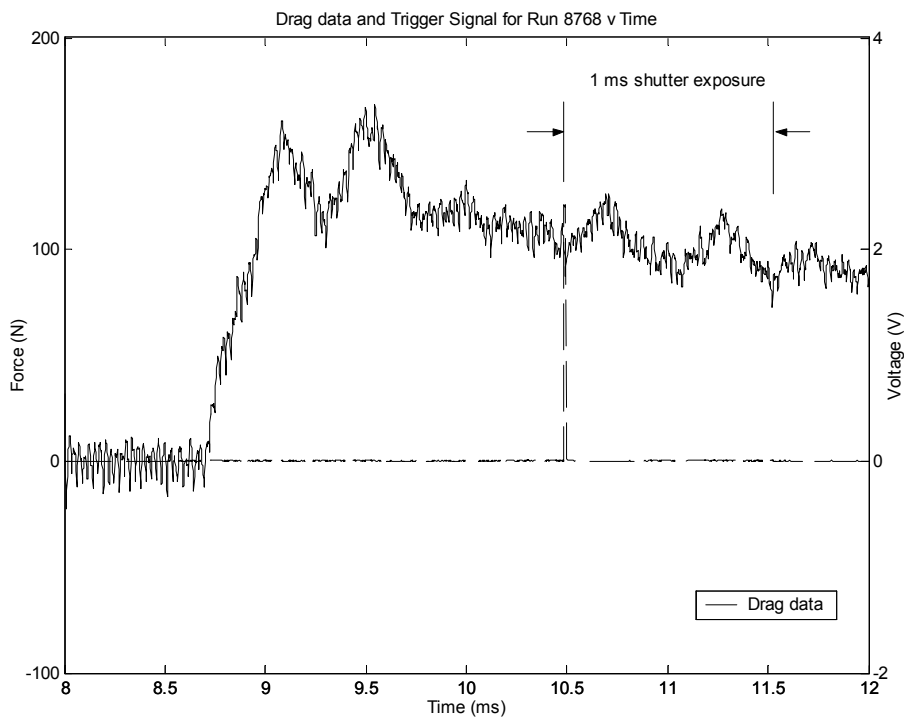


Fig. 5.32. Drag data and TTL to trigger camera.

In Fig 5.31, a thin copper wire wrapped around the conical fore-body can be seen. This was done to trip the boundary layer and to determine its effects on the measured drag force. The bright spots in the image indicate regions of high temperature. This can be seen in the crotch region of each intake. There is no evidence of flow spilling around the intakes (which would appear as large luminous regions due to low flow speeds) and

thus the result indicates that the inlet is unchoked. This ties in with the drag measurements made by Tanimizu during this shot. The delay generator was triggered from a pressure transducer in the nozzle supply region and a TTL signal 2 ms later triggered the camera. The TTL signal sent to the camera was compared to the deconvolved drag data for the experiment as shown in Fig 5.32. It can be seen that the 1 ms shutter exposure occurred during the test time for that shot. The camera trigger signal was recorded for all T4 tests and was compared to either a signal in the test section or to the stagnation pressure signal to ensure that the flow image in the BOS experiments were acquired in the test time.



Fig.5.33. Shot 8772, $p_s = 31.7$ MPa, $h_s = 6.0$ MJ/kg, $M_\infty = 7.2$, $p_\infty = 2.9$ kPa, $U_\infty = 3.2$ km/s, $T_\infty = 505$ K

Fig 5.33 shows the flow image for the T4 shot 8772. This test was done at 6.0 MJ/kg. The nozzle-supply enthalpy was 3.5 MJ/kg higher than that for shot 8768 but the camera shutter was opened for the same period of 1 ms. The light source was triggered within the shutter exposure time to illuminate the dot mask. The high temperature gases caused some luminosity at the tip of the Pitot probe and in the scramjet intake region. The brightness of this image was enhanced using the Paint Shop Pro program. It was not possible to cross correlate this image with the no-flow image and to generate schlieren images because the dots in the background were not clear enough.

Fig 5.34 shows the absolute difference between the reference and flow images for shot 8776. This shot was at a nozzle-supply enthalpy of 8.0 MJ/kg and the camera shutter exposure time was set to 30 μ s. At this shutter speed, the luminosity due to the hot gases was not seen. This result demonstrated the appropriateness of the current camera for

5.6 BOS results in the T4 shock tunnel

BOS visualisation of flows typical to scramjet conditions in T4. This was the largest image displacement that was seen during the T4 shock tunnel tests. It was due to the vibration of the camera tripod during the test. In subsequent tests, the camera was mounted on a vibration isolated table to ensure minimal movements.”

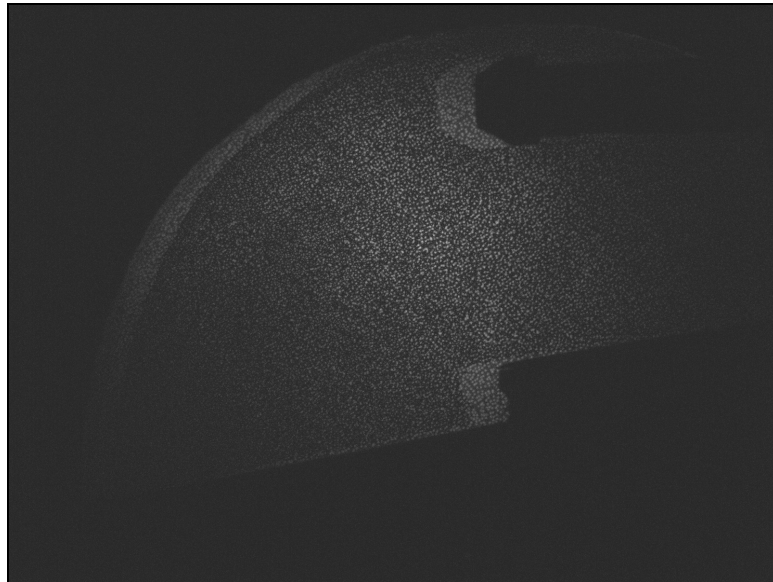
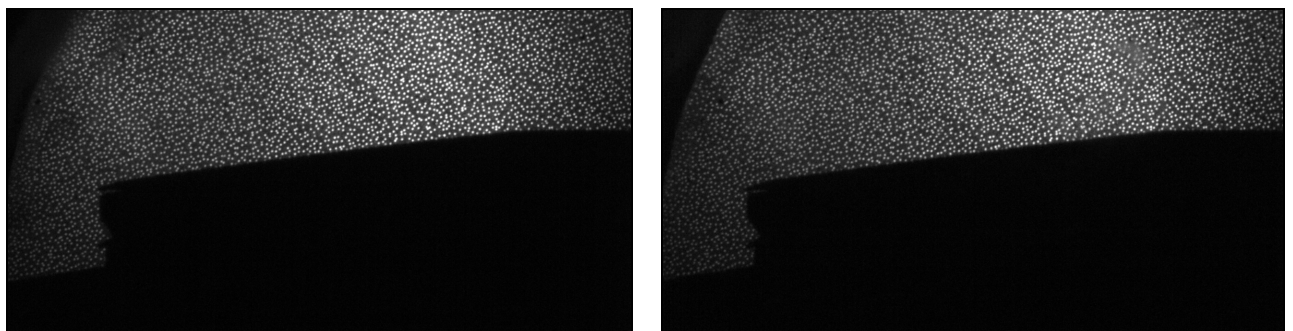


Fig.5.34. Shot 8776, $p_s = 18.7$ MPa, $h_s = 7.9$ MJ/kg, $M_\infty = 6.8$, $p_\infty = 1.9$ kPa, $U_\infty = 3.6$ km/s, $T_\infty = 707$ K.

The BOS system was setup again to visualise the intake region in shot 8770. The displacements due to vibration were not as severe as in shot 8776. The reference and flow images are shown in Fig 5.35.



(a) Reference image

(b) Flow image

Fig. 5.35. BOS system focussed at the intake region of the scaled scramjet model.

It was possible to correct for camera movements and to produce schlieren images using the image data for this shot. The aim of this test was to confirm that the intake ducts remained unchoked during the tests. A choked intake decreases the mass flow passing through the combustors and increases the drag. Fig 5.36 shows the contour plot of the

vertical displacement vectors. This result was scaled and superimposed onto the CAD model as shown in Fig 5.37.

The flow image was taken with a shutter exposure time of 1 ms for a Mach 8.2 oncoming flow at a nozzle-supply enthalpy of 2.6 MJ/kg. The forebody shock generated at the tip of the cone can be seen at the left of the image. This shock was captured within the cowl at this condition. The external compression shock from the cowl can be seen sweeping back at an angle of approximately 5° to the cowl in the BOS image. There is some evidence of a curved shock initiating at the crotch of the intake. This was attributed to the finite bluntness that occurs at this location on the model. There was no evidence of an un-start of the intakes.

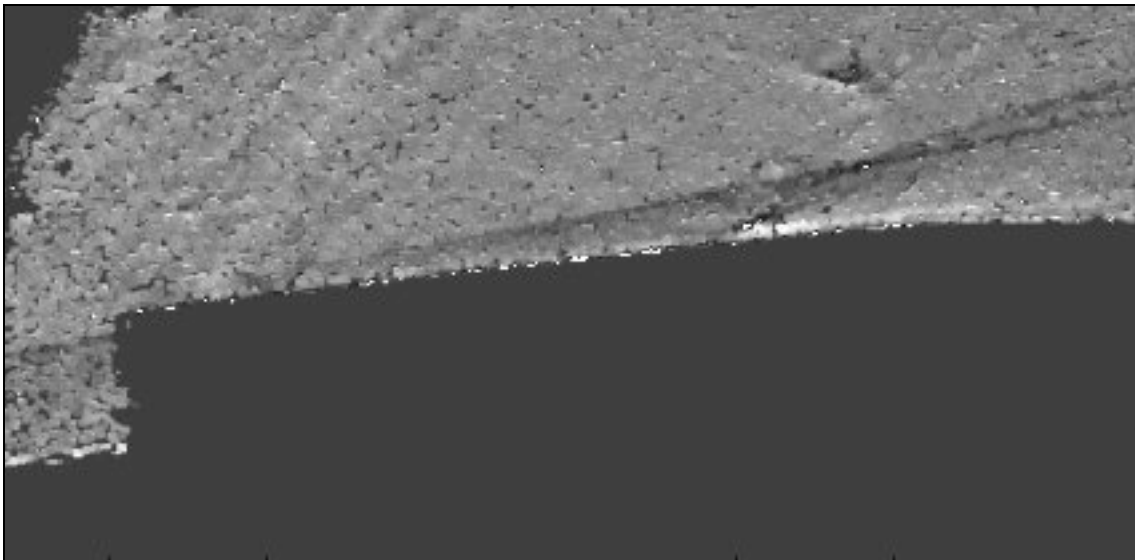


Fig. 5.36. Horizontal knife-edge schlieren image.

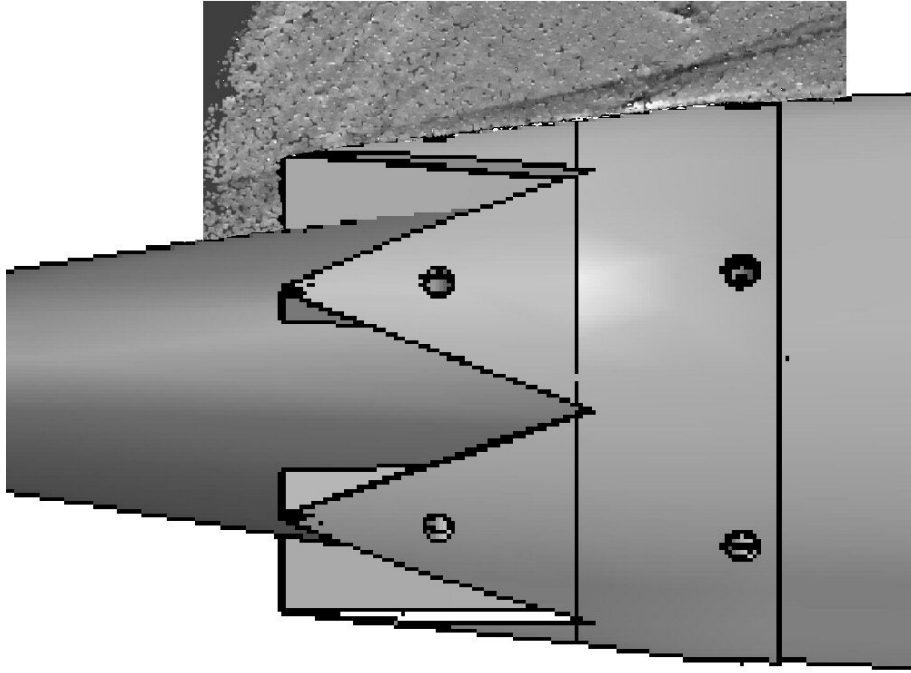


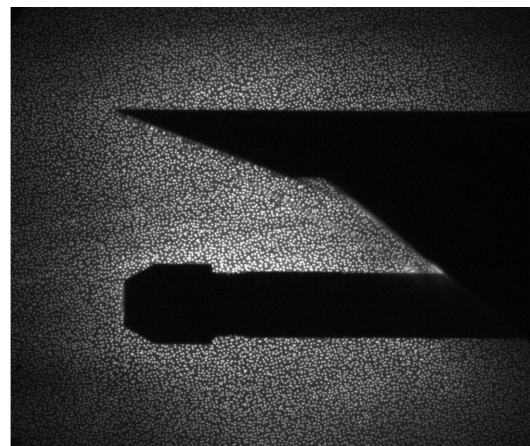
Fig. 5.37. Shot 8770, $p_s = 36.9$ MPa, $h_s = 2.6$ MJ/kg, $M_\infty = 8.2$, $p_\infty = 2.36$ kPa, $U_\infty = 2.2$ km/s, $T_\infty = 180$ K, shutter exposure = 1.0 ms.

5.6.2 Material tests results in the T4 shock tunnel

In this section, the BOS results obtained for the experiments described in section 4.3.2 are presented. Figures 5.38(a) and 5.38(b) show the reference and flow images of the flat plate of this test campaign set at an angle of 0° to the free-stream flow in the test section. The flow image in Fig. 5.38(b) was captured at a nozzle-supply enthalpy of 4.0 MJ/kg at a free-stream Mach number of 7.2



(a) Reference image



(b) Flow Image

Fig. 5.38. Shot 9058, flat plate at 0° AOA, $p_s = 21.7$ MPa, $h_s = 4.0$ MJ/kg, $M_\infty = 7.2$, $p_\infty = 2.3$ kPa, $U_\infty = 2.6$ km/s, $T_\infty = 348$ K, shutter exposure = 40 μ s.

Some distortion of the background pattern below the plate is apparent in the flow image. This comes from the high density gradients across the strong shock generated by the leading edge of the plate. Little distortion can be seen above the plate and around the Pitot probe. The pixel displacement estimated using the cross-correlation routine is shown in Fig. 5.39.



Fig. 5.39. Gradient vector image, shot 9058, search window size = 16 x 16 pixels, step size = 4 pixels.

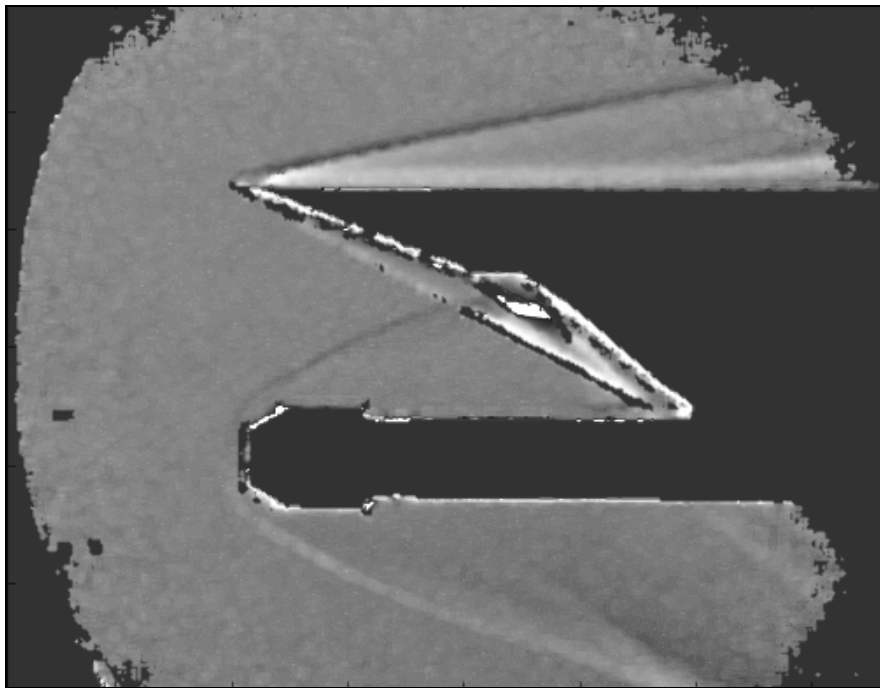


Fig. 5.40. Horizontal knife-edge schlieren.

By plotting contours of the vertical and horizontal components of the displacement vectors, the horizontal and vertical knife-edge schlieren images shown in Figs. 5.40 and 5.41 were obtained. In these images, the viscous interaction shock generated on the top surface of the plate is visible. A thin boundary layer is also seen close to the model

5.6 BOS results in the T4 shock tunnel

surface in Fig. 5.40. The strong shock wave on the under surface of the plate has caused saturation of the schlieren and parts of that shock wave appear as a dark line in Fig. 5.40 rather than a light one. The bow shock wave ahead of the Pitot probe is visible in the vertical knife-edge visualisation in Fig. 5.41. The bending of the Pitot's bow shock around the probe is clearest in Fig. 5.40 when the density gradients become more vertical. The bow shock wave around the Pitot probe can be seen interacting with the compression shock coming off the leading edge of the plate. A dark grey region can be seen in that area.

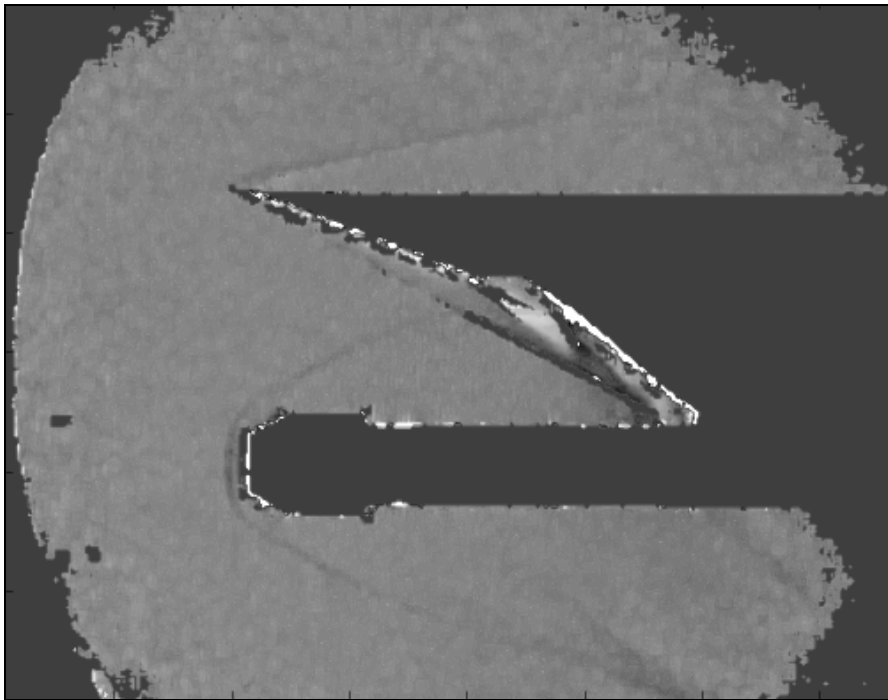


Fig. 5.41. Vertical knife-edge schlieren.

The flat plate was inclined at an angle of 10° to the oncoming flow and another BOS image was made. The reference and flow images are shown in Fig. 5.42. The SLS wedge, mounted towards the downstream end of the plate, can be seen in the top right corner in Fig. 5.42.

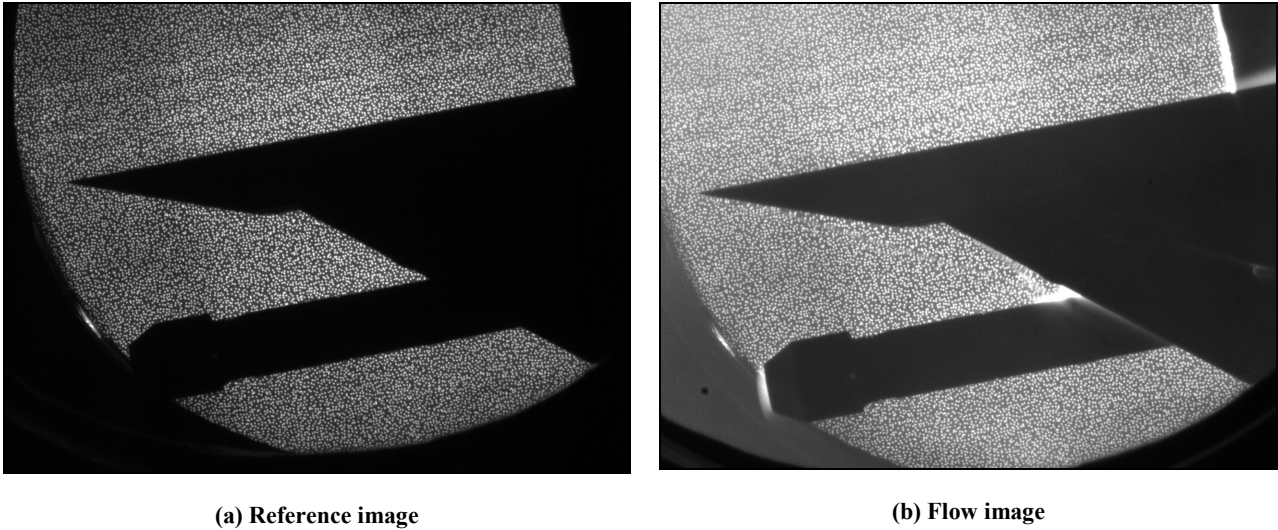


Fig. 5.42. Shot 9057, flat plate at 10° AOA, $p_s = 21.9$ MPa, $h_s = 3.5$ MJ/kg, $M_\infty = 6.7$, $p_\infty = 4.0$ kPa, $U_\infty = 2.5$ km/s, $T_\infty = 351$ K, shutter exposure= 1.07 ms.

The camera shutter exposure was set to 1.07 ms for this shot. With the longer exposure time some luminosity from the hot regions in the flow obscured the dots at the tip of the Pitot probe and near the interface between the stem of the probe and the front of the model in the flow image.

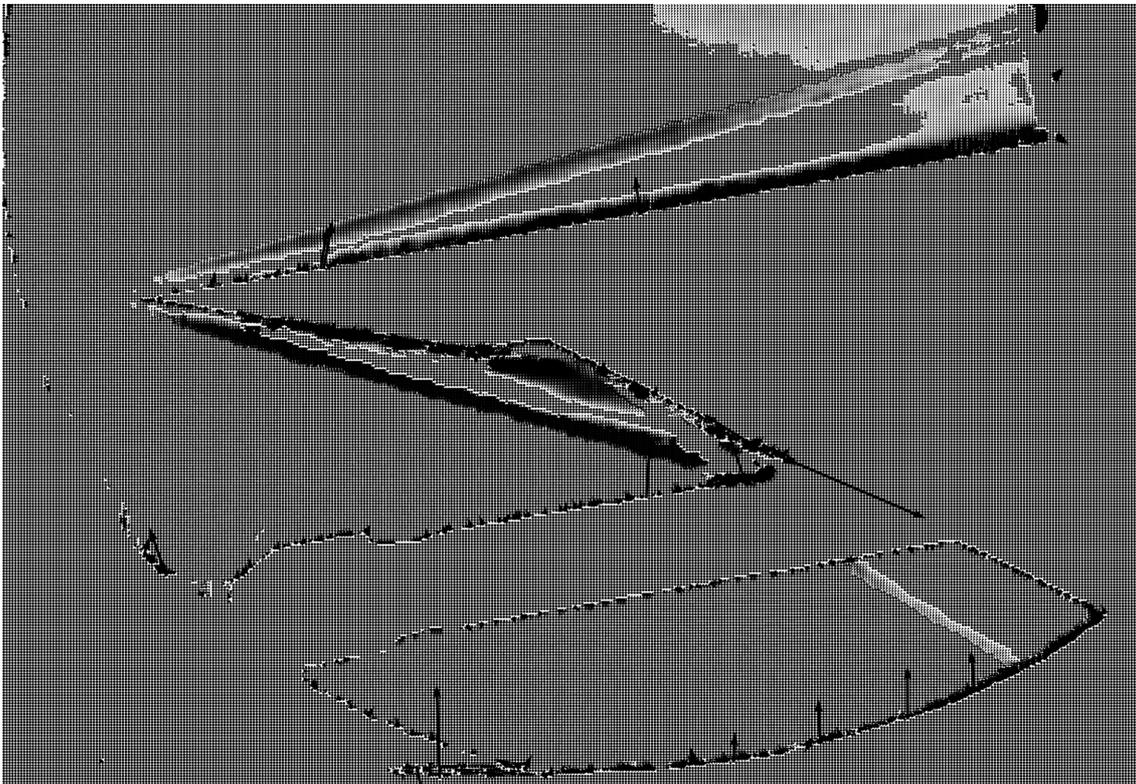


Fig. 5.43. Density gradient vectors obtained using a cross-correlation window size of 32×32 pixels and a search size of 4 pixels.

The PIV processing resulted in erroneous displacement vectors in regions of high luminosity as seen in Fig 5.43. These appear as dark spots in the horizontal knife-edge schlieren image shown in Figs 5.44. This luminosity problem was not seen for shot 9058, even though it was at a slightly higher stagnation enthalpy because the shutter exposure was about 25 times lower for shot 9058. Again, there are some regions of saturation near the shock wave from the under surface of the plate. The compression shocks on top and bottom surfaces of the plate can be clearly seen. The bow shock from the Pitot probe is again visible. The boundary layer developing on the top surface of the plate can be observed close to the model surface.

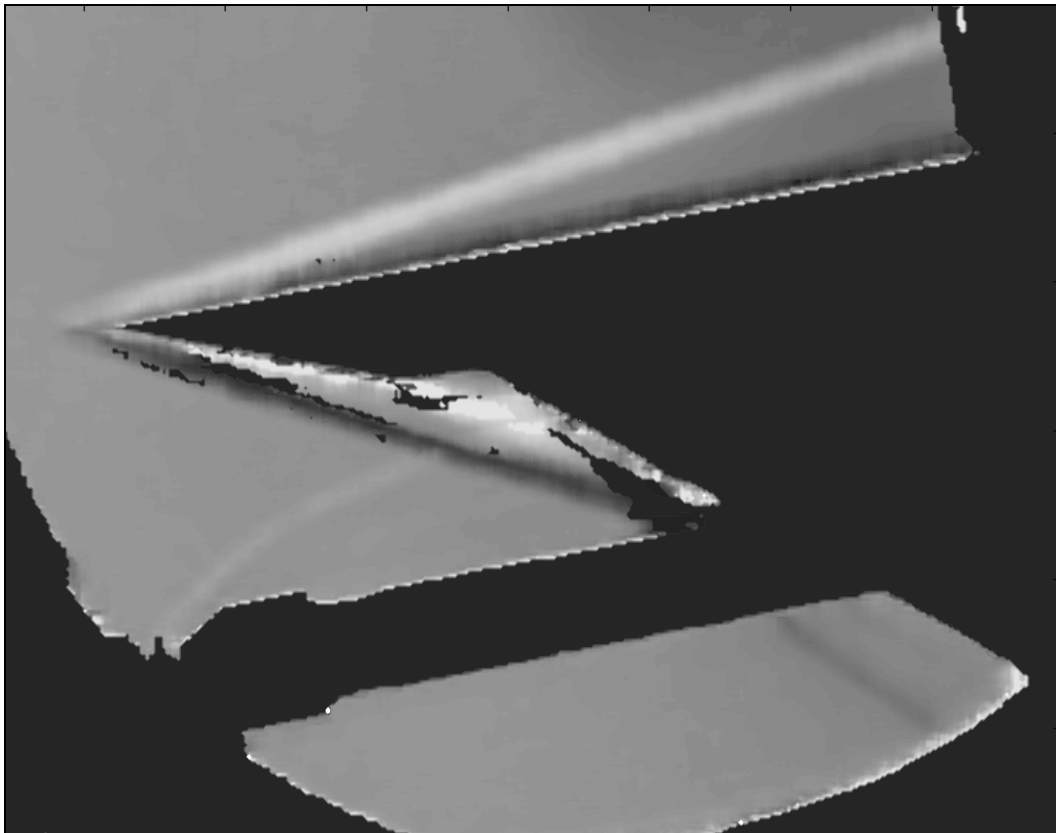
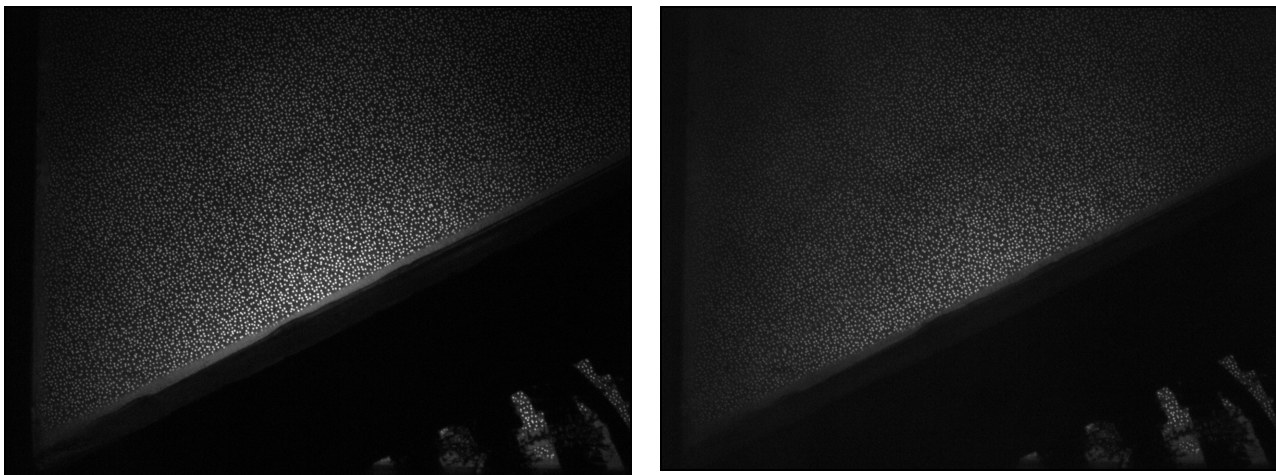


Fig. 5.44. Horizontal knife-edge schlieren image.

5.6.3 Visualizing the flow in a scramjet duct

Fig 5.45 show the reference and flow images for shot 9066 for the experimental campaign described in section 4.3.3.



(a) Reference image

(b) Flow image

Fig. 5.45. Shot 9066, $p_s = 42$ MPa, $h_s = 3.4$ MJ/kg, $M_\infty = 7.9$, $p_\infty = 3.0$ kPa, $U_\infty = 2.5$ km/s, $T_\infty = 255$ K, shutter exposure = 40 μ s.

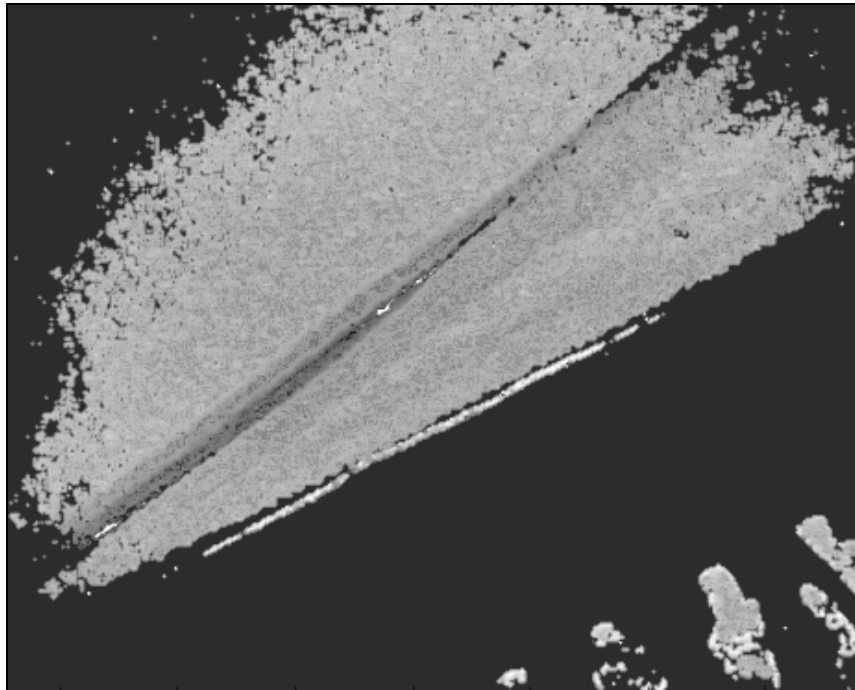


Fig. 5.46. Horizontal knife-edge BOS image.

The image shown in Fig.5.46 illustrates a horizontal knife-edge BOS image of flow in the region towards the leading edge of the 27.1° plate. It was not possible to obtain an image closer to the leading edge with the sidewalls in place because the glass inserts did not extend all the way to the leading edge of the plate (see Fig 4.8). For this shot, no fuel was injected and the compression shock from the plate can clearly be seen. It appears not to be planar. This is attributed to the shock wave interacting with the side wall boundary layers as discussed later.

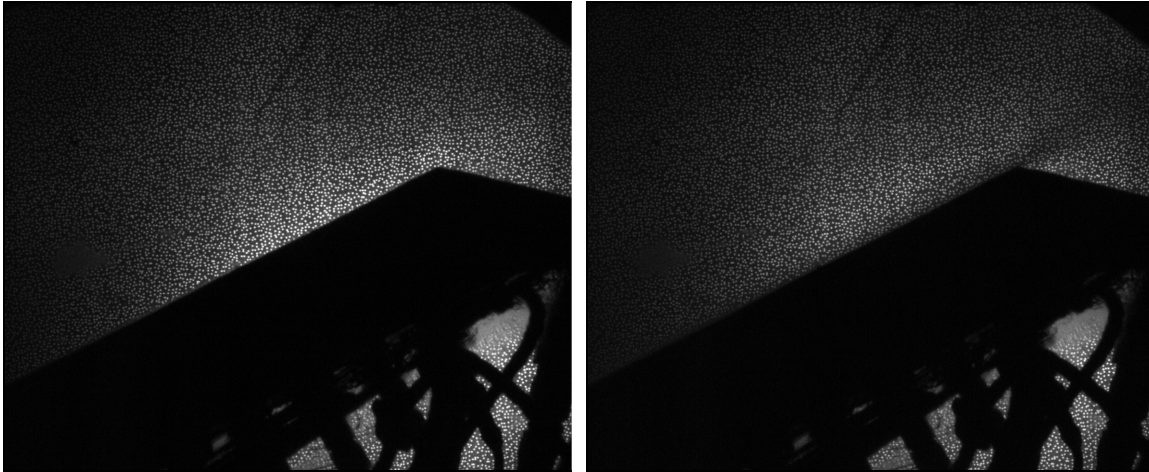


Fig. 5.47. Shot 9086, $p_s = 26.9$ MPa, $h_s = 3.8$ MJ/kg, $M_\infty = 7.4$, $p_\infty = 2.5$ kPa, $U_\infty = 2.6$ km/s, $T_\infty = 320$ K, shutter exposure = 30 μ s.

Fig 5.47 shows the reference and the flow image for shot 9086 taken during the same test campaign. The BOS system was setup to focus at the trailing edge of the model. The horizontal knife-edge BOS image is shown in Fig. 5.48. For this shot, the free-stream Mach number was 7.4 and the nozzle-supply enthalpy was 3.8 MJ/kg. This shot shows the end of the 27.1° plate and the start of the expansion surface.



Fig. 5.48. Horizontal knife-edge BOS image, shot 9086.

A holographic interferogram taken at a similar condition is shown in Fig. 5.49. This image was taken with a free-stream Mach number of 7.3 and a nozzle-supply enthalpy of 4.3 MJ/kg. In an interferogram, a change in fringe pattern can be attributed to a change in density in the flow. Air was used as test gas for these two shots and, in both cases, no fuel was injected. In both images, the oblique shock emanating from the

leading edge can be clearly seen rising away from the model surface. The strong expansion fan generated as the flow expands to the thrust surface can be seen in both visualisation images. The region between the plate and the shock wave appears to be non-uniform, which is not expected for a 2-D flow. This was not observed in other interferograms taken when the sidewalls of the model were removed (Coras and Paull, 2006), although the images with the side-walls removed were focused closer to the leading edge of the plate. These features are apparent in both the BOS and interferometric images and are attributed to the interaction of the leading edge shock wave with the boundary layers formed on the sidewalls of the model. The swept shock wave boundary layer interaction that develops on the sidewalls would be strong enough to separate the boundary layers on the sidewalls (Korgegi, 1973), and this would lead to a complex shock pattern near the interaction. No BOS images were taken with the sidewalls of the model removed.



Fig. 5.49. Flow Hologram, shot 9167, $p_s = 30.7$ MPa, $h_s = 4.3$ MJ/kg, $M_\infty = 7.3$, $p_\infty = 2.6$ kPa, $U_\infty = 2.8$ km/s, $T_\infty = 363$ K.

A series of weak, almost horizontal compression waves is seen towards the top of the BOS image in Fig. 5.48. These waves were also captured in some other BOS images, an example of which is shown in Fig. 5.50. They appeared to occur intermittently. We speculate that these emanate from near the exit of the nozzle of the tunnel and may be

associated with an unsteady separation of the nozzle boundary layer during some of the tests. However, further investigation is necessary to clarify this.

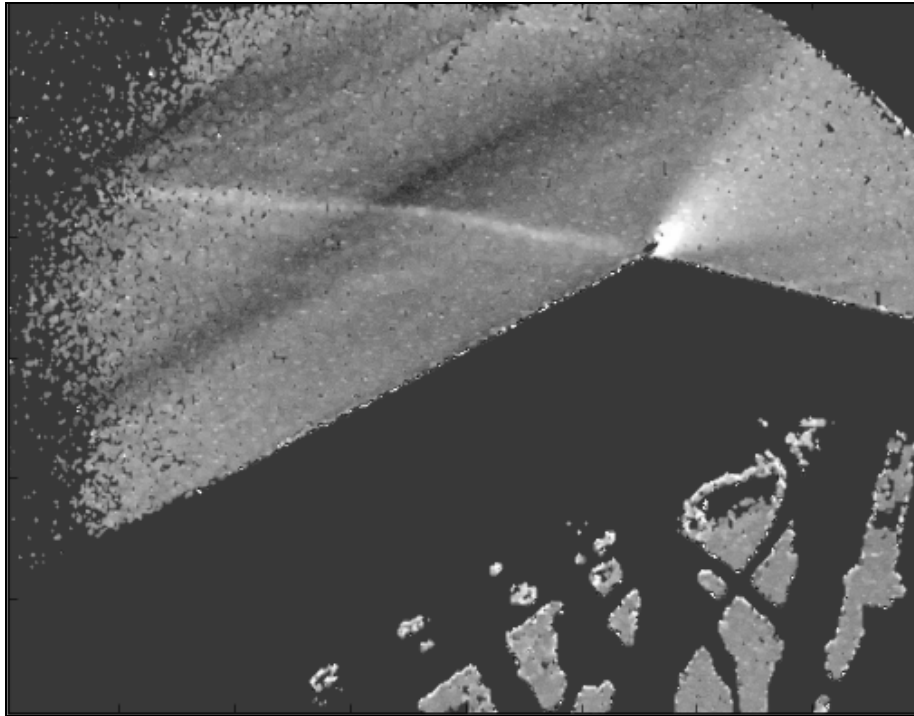


Fig. 5.50. Fuel into N_2 , injected at the leading edge, shot 9085, $p_s = 27.4$ MPa, $h_s = 3.8$ MJ/kg, $M_\infty = 7.5$, $p_\infty = 2.4$ kPa, $T_\infty = 313$ K, shutter exposure = 30 μ s.

The BOS image in Fig. 5.50 was obtained in shot 9085 in which hydrogen was injected from the holes near the leading edge of the 27.1° plate. The free-stream conditions were similar to those for shot 9086 but nitrogen was used as the test gas to suppress combustion. There is no evidence of the fuel jet at this location. When fuel was injected into a flow of air, luminosity in the combustion zone obscured the background dot pattern. An example of this is shown for shot 9077 in Fig. 5.51. The flow conditions for shot 9077 were similar to those for the nitrogen shot 9085 in Fig. 5.50 but the shutter exposure was increased from 30 to 40 μ s. It can be seen that the dots are obscured above the plate and it was not possible to compare them with the reference image dots to produce a BOS image.

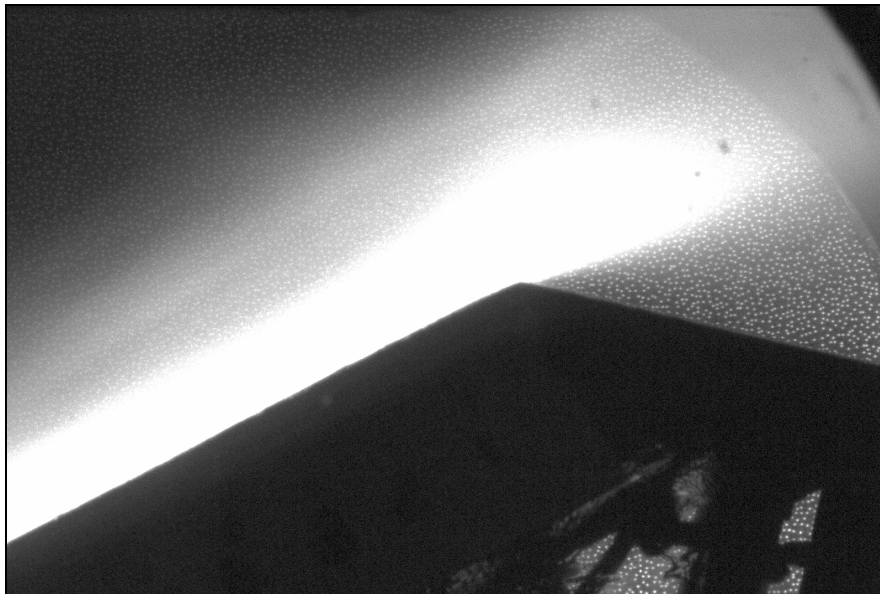


Fig. 5.51. Shot 9077 flow image, fuel injected in air at leading edge, $p_s = 21.5$ MPa, $h_s = 3.3$ MJ/kg, $M_\infty = 7.7$, $p_\infty = 1.8$ kPa, $T_\infty = 254.4$ K, shutter exposure = 40 μ s.

5.6.4 Visualizing the flow at the intake of a Mach 8 scramjet

This section reports the results for the experiments described in section 4.34. A schlieren image for shot 9214 is shown in Fig.5.52. The free-stream Mach number was 6.4 and the nozzle-supply enthalpy was 3.12 MJ/kg. A shutter exposure of 10 μ s was used for this shot. The compression shock on top of the model is clearly seen. The viscous interaction shock as well as a thin boundary layer is seen at the bottom surface of the model. Part of the curved bow shock around the Pitot probe is clearly visible.

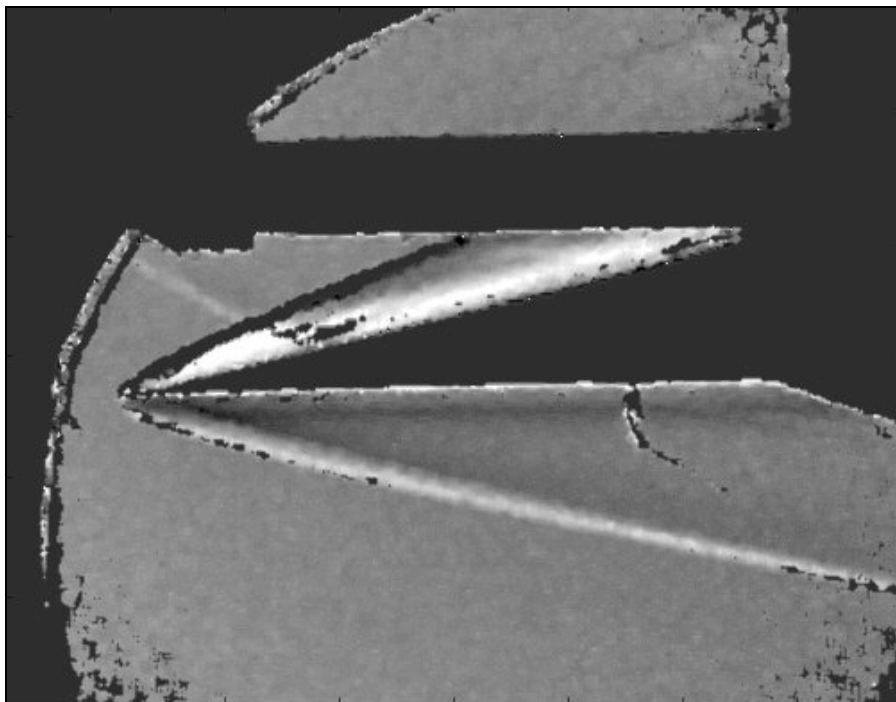


Fig. 5.52. Vertical knife edge schlieren, s9214.

5.6 BOS results in the T4 shock tunnel

In the next test, the BOS imaging technique was setup to visualise region B of the model as labelled in Fig 4.8. Fig 5.53 shows the schlieren image result obtained. The location of this shock indicates that the inlet was not choked during this test and this was confirmed by pressure measurements on the intake and combustor.

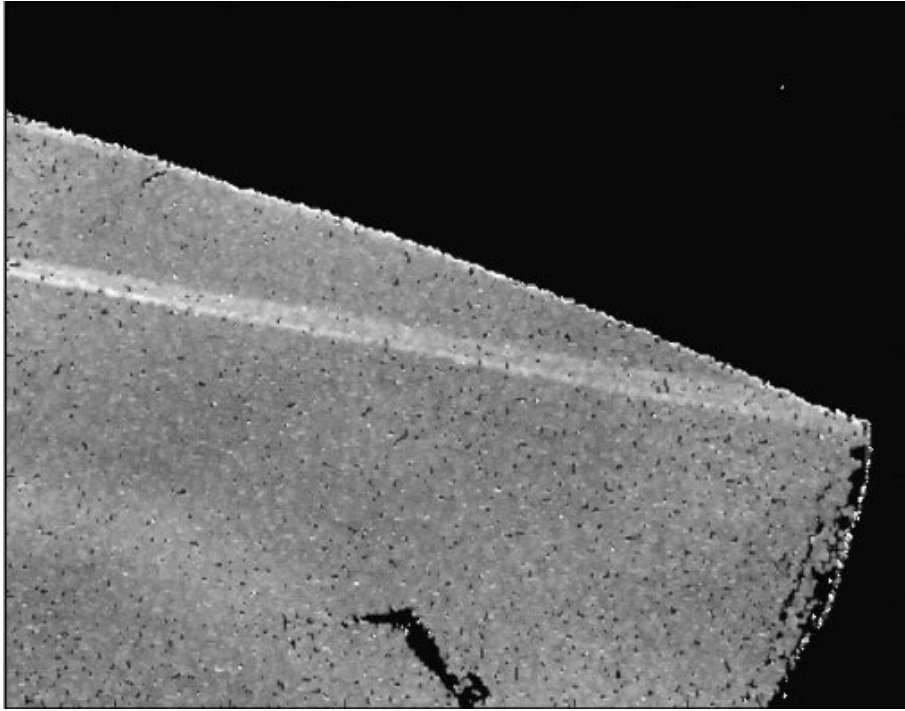


Fig. 5.53. Vertical knife-edge schlieren, s9219, $p_s = 13.5$ MPa, $h_s = 3.1$ MJ/kg, $M_\infty = 6.6$, $p_\infty = 3.5$ kPa, $T_\infty = 318$ K, $U_\infty = 2.4$ km/s, shutter exposure = 10 μ s.

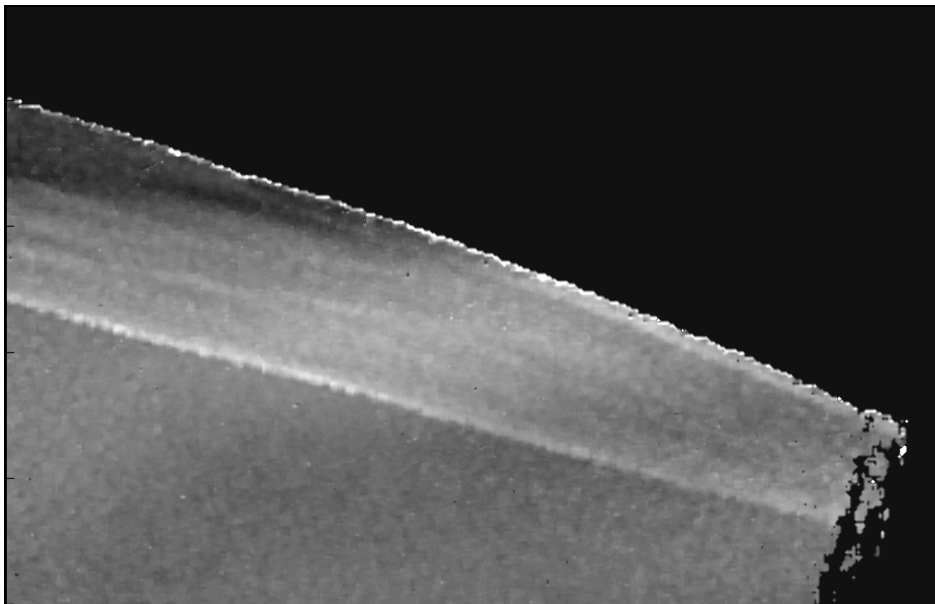


Fig. 5.54. Vertical knife-edge schlieren, s9223. , $p_s = 13.7$ MPa, $h_s = 2.34$ MJ/kg, $M_\infty = 7.0$, $p_\infty = 3.4$ kPa, $T_\infty = 215$ K, $U_\infty = 2.1$ km/s, shutter exposure = 10 μ s.

The experiment was repeated with a higher mass flow rate of fuel injected into the combustor and the schlieren resulting image is shown in Fig. 5.54. The pressures indicated that the combustor was choked for this fuel flow rate and the upstream influence of this caused the compression shock to spill away from the intake. This was confirmed by increased pressures on the intake. This shows that BOS can be useful for helping to detect phenomena such as inlet un-start.

5.6.5 Range of conditions for the BOS technique in T4

A summary of the test conditions at which the BOS system was tested is given in Table 5.4. It can be seen that the system can be used for test conditions ranging between a stagnation enthalpy of 2.6 MJ/kg to 5.9 MJ/kg. The camera shutter was set to 10 μs at the two high enthalpy cases. Enthalpies greater than 5.9 MJ/kg would result in flow luminosity, which would obscure the dot in the BOS flow image.

Table 5.4. T4 test conditions and shutter times for the BOS technique.

Shot Number	h_s (MJ/kg)	T_e (K)	Shutter Time (μs)
8770	2.6	180	1000
9057	3.5	351	1070
9058	4.0	348	40
9066	3.4	255	40
9086	3.8	320	30
9085	3.8	313	30
9219	3.1	318	10
9223	2.3	215	10
9375	5.8	641	10
9380	3.1	318	10
9417	5.8	645	10
9421	5.9	663	10

Conclusions and Recommendations

6.1 Conclusions

The Background oriented flow visualisation technique has been experimentally tested for qualitative flow visualisation for moderate and high enthalpy shock tunnel conditions.

Simulated horizontal and vertical knife-edge schlieren images can be generated. The current experiments demonstrate that the BOS technique can be applied in T4 shock tunnel tests to visualise flow features at conditions typical of scramjet operation. A range of conditions where BOS was successfully realised have been given.

The optical arrangement for the BOS images is simple. The resolution of the current BOS system is not as high as usually obtained using conventional schlieren systems but the main flow features can be visualised with few optical components with this simple arrangement.

The BOS system does allow post processing to visualise density gradients in any chosen direction. Flow luminosity, due to high temperature regions of the flow and in zones of combustion, interfered with some of the images.

6.2 Recommendations

Future work involving the background oriented schlieren technique in impulse facilities can be focused on evaluating the flow field density over the model and in the test section using the density gradient vectors. Grey or colour levels can be assigned to the density values in the schlieren image. It will then be possible to obtain a quantitative measure of the density field, which can be compared with Computational Fluid

Conclusions and Recommendations

Dynamics predictions. An introduction to the equations that can be used for this quantitative evaluation is given in Appendix A.

Further tests can be done using this technique at higher enthalpy conditions. The luminosity at these conditions can be overcome with a combination of short shutter camera opening times and a higher intensity light source.

Bibliography

Adrian, R. J., "Particle-Imaging Techniques for Experimental Fluid Mechanics," *Annual Review of Fluid Mechanics*, Vol. 23, 1991, pp. 261-304.

Austin, J. M., Jacobs, P. J., Kong, M. C., Barker, P., Littleton, B. N., and Gammie, R., "The Small Shock Tunnel Facility at UQ," Tech. Rep. 02/1997, Department of Mechanical Engineering, The University of Queensland, 1997.

Billig, F. S., "Shock-Wave Shapes Around Spherical- and Cylindrical-Nosed Bodies," *Journal of Spacecrafts and Rockets*, Vol 4, No. 6, 1967, pp. 822 - 823.

Bishop, A. I., Littleton, B. N, McIntyre, T. J., Rubinsztein-Dunlop, H., "Near-Resonant Holographic Interferometry of Hypersonic Flow," *Shock Waves*, Vol.11, No. 1, 2001, pp. 23-29.

Brigham, E. O., *The fast Fourier transform*, Prentice-Hall, 1974.

Bronstein, I. N. and Semendjajew, K. A., *Taschenbuch der Mathematik*, Vol 1, B. G. Teubner, 1991

Buttsworth, D. R., Goozée, R. J., Jacobs, P. J., "Measurement and Simulation of the Interface in a Low-Enthalpy Shock Tunnel," *14th AIAA/AHI Space Planes and Hypersonic Systems and Technologies Conference*, Canberra, Nov 2006, Paper AIAA-2006-8108.

Carlton, J. S., "Observations of Turbulent-Burst Geometry and Growth in Supersonic Flow," Tech. Note 4235, Ames Aeronautical Laboratory, Moffett Field, California, 1958.

Chen, J., Katz, J., “Elimination of Peak-Locking Error in PIV Analysis using the Correlation Mapping Method,” *Measurement Science and Technology*, Vol. 16, No. 8, 2005, pp. 1605-1618.

Christensen, K. T., “The influence of peak-locking errors on turbulence statistics computed from PIV ensembles” *Experiments in Fluids*, Vol. 36, No. 3, 2004, pp. 484–497.

Coras, S and Paull, A., “Experiments on External Combustion with Leading Edge Fuel-Injection in Hypersonic Flow,” *14th AIAA/AHI Space Planes and Hypersonic Systems and Technologies Conference*, Canberra, Nov 2006, Paper AIAA-2006-7981.

Couch, L. W., *Digital and Analog Communications Systems*, Prentice Hall, New Jersey, 2001.

Craddock, C. S., Jacobs, P.A., and Gammie, R., “Operational Instructions for the Small Shock Tunnel at UQ,” Tech. Rep. 02/1998, Department of Mechanical Engineering, The University of Queensland, 1998.

Dalziel, S. B., Hughes, G. O., and Sutherland, B. R., “Whole-Field Density Measurements by 'Synthetic Schlieren,'” *Experiments in Fluids*, Vol. 28, No. 4, 2000, pp. 322-335.

Fincham, A., and Delerce, G., “Advanced Optimization of Correlation Imaging Velocimetry Algorithms,” *Experiments in Fluids*, Vol. 29 (Suppl.), No. 7, 2000, pp S013–S022.

Fincham, A. M., and Spedding, G. R., “Low Cost, High Resolution DPIV for Measurement of Turbulent Fluid Flow,” *Experiments in Fluids*, Vol. 23, No. 6, 1997, pp. 449-462.

Gardner, T., “Upstream porthole injection in a 2-D scramjet model,” M.Sc. Dissertation, Department of Mechanical Engineering, The University of Queensland, 2000.

Goldstein, R. J., *Fluid Mechanics Measurements*, Hemisphere Publishing Corp., Washington, DC, 1983.

Gui, L., and Seiner, J. M., “An Improvement in the Nine-Point Central Difference Image Correction Method for Digital Particle Image Velocimetry Recording Evaluation,” *Measurement Science and Technology*, Vol. 15, No. 10, 2004, pp. 1958–1964.

Hornung, H. G., “Non-equilibrium Dissociating Flow over Spheres and Circular Cylinders,” *Journal of Fluid Mechanics*, Vol. 53, 1972, pp. 149-176.

Jacobs, P. A., “MB CNS: A Computer Program for the Simulation of Transient Compressible Flow,” Tech. Rep. 10/1996, Department of Mechanical Engineering, The University Of Queensland, 1996.

Jacobs, P. A., “Shock Tube Modelling with L1d,” Tech. Report 13/98, Department of Mechanical Engineering, The University of Queensland, 1998.

Jain, A. K., *Fundamentals of Digital Image Processing*, Prentice Hall, New Jersey, 1989.

Jensen, O.S., “Optical Density and Velocity Measurements in Cryogenic-Gas Flows,” Ph.D Dissertation, Institute for Fluid Dynamics, Swiss Federal Institute of Technology, Diss. ETH No. 15259, Zurich, 2003.

Kawaguchi, J., Uesugi, K.T., Fujiwara, A., Saitoh, H., “The MUSES-C, Mission Description and its Status,” *Acta Astronautica* 45(4) 397- 405 (1999)

Klinge, F., Kirmsem, T, Kompenhans,J., “Application of Quantitative Background Oriented Schlieren (BOS): Investigation of a Wing Tip Vortex in a Transonic Wind Tunnel,” *Proceedings of the PSFVIP4*, edited by J. P. Prenel and Y. Bailly, Chamonix, France, 2000.

Korgegi, R.H., "A Simple Correlation for Incipient Turbulent Boundary-Layer Separation due to a Skewed Shock Wave," *AIAA Journal*, Vol. 11, No. 11, 1973, pp. 1578-1579.

Krek, R. M., and Jacobs, P. A., "STN, Shock Tube and Nozzle Calculations for Equilibrium Air," Tech. Rep. 2/1993, Department of Mechanical Engineering, The University of Queensland, 1993

Lamar, J. E., "Flow-Visualization Techniques Used at High Speed by Configuration Aerodynamics Wind-Tunnel-Test Team," NASA TM 210848, April 2001.

Lecordier, B., Demare, D., Vervisch, L. M. J., Réveillon, J., and Trinité, M., "Estimation of the Accuracy of PIV Treatments for Turbulent Flow Studied by Direct Numerical Simulation of Multi-Phase Flow," *Measurement Science and Technology*, Vol. 12, No. 9, 2001, pp. 1382–1391.

Lordi, J. A., Mates, R. E., Moselle, J. R., "Computer Program for Numerical Simulation of Nonequilibrium Expansions of Reacting Gas Mixtures," *NASA CR-472*, 1966.

McIntosh, M. K., "Computer Program for the Numerical Calculation of Frozen and Equilibrium Conditions in Shock Tunnels," Department of Physics, Australian National University, 1968.

McIntyre, T. J., Eichmann, T. N., Hajek, K., Kovachevich, A., "Visualisation and Measurement of Flow on the Inlet of an Upstream Injected Supersonic-Combustion Ramjet," *Proceedings of the Fourth Australian Conference on Laser Diagnostics in Fluid Mechanics and Combustion*, edited by Z.T. Alwahabi, Adelaide, Australia, 2005.

McIntyre, T. J., "Personal communication," 2006.

Meier, G. E. A., "Computerized Background-Oriented Schlieren," *Experiments in Fluids*, Vol. 33, No. 1, 2002, pp. 181-187.

Melling, A., "Tracer Particles and Seeding for Particle Image Velocimetry," *Measurement Science and Technology*, Vol. 8, No. 12, 1997, pp.1406-1416.

Merzkirch, W., *Flow visualization*, New York : Academic Press, 1987.

Nelson, J.C, Vail, N.K, Barlow, J.W, Beaman, J.J, Bourell, D.L, Marcus, H.L., "Selective Laser Sintering of Polymer-Coated Silicon-Carbide Powders," *Industrial & Engineering Chemistry Research*, Vol. 34, No. 5, 1995, pp 1641,1651.

Oppenheim, A. V. and Schafer, R. W., *Digital signal processing*, Prentice-Hall, 1975.

Perlick, V., *Ray Optics, Fermat's Principle, and Applications to General Relativity*, Springer-Verlag. Berlin, 1956.

Porter, L. M., "High Enthalpy, Hypersonic Drag Measurement on Blunt Cones in an Impulse Facility," Ph.D Dissertation, Department of Mechanical Engineering, The University of Queensland, 1996.

Raffel, M., Willert, C. E., and Kompenhans, J., *Particle Image Velocimetry: A Practical Guide*, New York : Springer,1998.

Raghunath, S., Mee, D. J., Rösgen, T. and Jacobs, P. A., "Background Oriented Schlieren for Flow Visualization in Shock Tunnels", *Proceedings of the 25th International Symposium on Shock Waves*, edited by G. Jagadeesh., E. Arunan., K.P.J. Reddy., Bangalore, India, 2005.

Richard, H., and Raffel, M., "Principle and applications of the Background Oriented Schlieren (BOS) method," *Measurement Science and Technology*, Vol. 12, No. 9, 2001, pp. 1576-1585.

Rösgen, T., "Optimal Subpixel Interpolation in Particle Image Velocimetry," *Experiments in Fluids*, Vol. 35, 2003, pp. 252,256.

Sanderson, S. R., Simmons, J. M., "Drag Balance for Hypervelocity Impulse Facilities," *AIAA Journal*, Vol. 29, No. 12, 1991, pp. 2185-2191.

Settles, G. S., *Schlieren and Shadowgraph Techniques: Visualizing Phenomena in Transparent Media*, Springer-Verlag., New York, 2001.

Smits, A. J., Lim, T. T., *Flow Visualization: Techniques and Examples*, Imperial College Press, 2000.

Stalker, R. J., and Crane, K. C. A., “Driver Gas Contamination in a High-enthalpy Reflected Shock Tunnel,” *AIAA Journal*, Vol. 16, 1978, pp. 277–278.

Stalker, R. J., and Morgan, R. G., “The University Of Queensland Free Piston Shock Tunnel T4 – Initial Operation and Preliminary Calibration,” *4th National Space Engineering Symposium*, Adelaide, June 12-14, 1998

Venkatakrishnan, L., and Meier G. E. A., “Density Measurements using Background Oriented Schlieren technique,” *Experiments in Fluids*, Vol. 37, No. 2, 2004, pp. 237-247.

Wegener, M. J., Bishop, A. I., McIntyre, T.,J., Rubinsztein-Dunlop, H., Stalker, R.J. and Morgan, R. G., “Visualisation and Analysis of Bow Shocks in a Superorbital Expansion Tube”. *AIAA Journal*, Vol. 34, No. 10, 1996, pp. 2200-2202.

Weinstein, L. M., Stacy, K., Vieira., G. J., Haering, Jr., E. D, and Bowers, A. H., “Visualization and Image Processing of Aircraft Shock Wave Structures”, *First Pacific Symposium on Flow Visualization and Image Processing*, Honolulu, Hawaii, 1997.

Wereley, S. T., and Gui, L., “A Correlation-Based Central Difference Image Correction (CDIC) Method and Application in a Four-Roll Mill flow PIV Measurement,” *Experiments in Fluids*, Vol. 34, No. 1, 2003, pp. 42–51.

Westerweel, J., “Digital Particle Image Velocimetry – Theory and Application,” Ph.D Dissertation, Delft University of Technology, Netherlands, 1993.

White, F. M., *Viscous Fluid Flow*, McGraw-Hill, USA, 1991.

Quantitative Evaluation of Density Fields using BOS

A.1 Introduction

The results shown in this thesis are qualitative in nature. However, further processing of the BOS algorithms can give a quantitative representation of the flow field. This chapter outlines possible techniques that could be used to determine density using the BOS system.

A.2 Density evaluation

The evaluation of density gradient vectors from the information contained in the reference and flow images is given in Chapter 3. Integrating the field of density gradient along the optical path length can give an estimate of the density in the field. Three possible integration methods for solving the latter are proposed and explained in this section.

The problem of how a light beam is deflected through an inhomogeneous density field was investigated using geometrical optics and Fermat's principle in Perlick (2000). This principle states that the light rays travelling between two points through an inhomogeneous refractive field chose the shortest optical path length. This principle was demonstrated with,

$$\delta \int n(x, y, z) ds = 0 \tag{A.1}$$

for the refractive index $n(x, y, z)$ where s denotes the arc length along the ray (Merzkirch, 1987). Using the Gladstone-Dale equation to relate the refractive index to the density, the equivalent set of differential equations for this principle can be formed as follows,

$$\frac{d^2 x}{dz^2} = \left\{ 1 + \left(\frac{dx}{dz} \right)^2 + \left(\frac{dy}{dz} \right)^2 \right\} \left\{ \frac{1}{n} \frac{\partial \rho}{\partial x} - \frac{dx}{dz} \frac{1}{n} \frac{\partial \rho}{\partial z} \right\} \tag{A.2}$$

and

$$\frac{d^2 y}{dz^2} = \left\{ 1 + \left(\frac{dx}{dz} \right)^2 + \left(\frac{dy}{dz} \right)^2 \right\} \left\{ \frac{1}{n} \frac{\partial \rho}{\partial y} - \frac{dy}{dz} \frac{1}{n} \frac{\partial \rho}{\partial z} \right\}, \tag{A.3}$$

for a beam travelling in the z -direction and a photographic viewing plane in the x - y plane. The deviation in the z -direction is small in a compressible flow (Merzkirch,

1987), which leads to the assumption that the slopes, $\frac{dx}{dz}$ and $\frac{dy}{dz}$ are negligible. Also,

since $\frac{\partial \rho}{\partial x}$, $\frac{\partial \rho}{\partial y}$ and $\frac{\partial \rho}{\partial z}$ are of the same order of magnitude, the differential equations can

be simplified to

$$\frac{d^2x}{dz^2} = \frac{1}{n} \frac{\partial \rho}{\partial x} \quad (\text{A.4})$$

and

$$\frac{d^2y}{dz^2} = \frac{1}{n} \frac{\partial \rho}{\partial y}. \quad (\text{A.5})$$

By back tracing the light rays received by the camera (Dalziel et al., 2000), the apparent shift $(\Delta x, \Delta y)$ in the origin of the light ray becomes,

$$\Delta x = W(W + 2Z_D) \frac{1}{n_0} \frac{\partial n}{\partial x} \quad (\text{A.7})$$

and

$$\Delta y = W(W + 2Z_D) \frac{1}{n_0} \frac{\partial n}{\partial y}, \quad (\text{A.8})$$

where W is the width of the homogenous field and Z_D is the distance of the background from the field. Dalziel et al. (2000) used the shift equations 6.7 and 6.8 to measure density in a water tank. A circular and a square cylinder rotating inside the tank were tested. The shift equations can also be used for a light beam passing through a density gradient region in a compressible flow.

The two possible ways for evaluating the density from the shift equations are;

1. using a Poisson's solver with W and Z_D as constants, and
2. using a 4th Order Finite Difference scheme to solve for $\rho(x,y)$, knowing the measured gradient field, $\frac{\partial \rho}{\partial y}$ and $\frac{\partial \rho}{\partial x}$.

A.2.1 Integrating with a Poisson solver

A Poisson solver can be used with the density gradient equations re-arranged in the form,

$$\frac{\partial}{\partial x} \left(\frac{\partial \rho}{\partial x} \right) + \frac{\partial}{\partial y} \left(\frac{\partial \rho}{\partial y} \right) = \nabla^2 \rho, \quad (\text{A.10})$$

where $\frac{\partial \rho}{\partial x}$ and $\frac{\partial \rho}{\partial y}$ are the measured experimental values. Jensen (2003) showed that this can be reduced to,

$$const. \left[\frac{\partial}{\partial x} \Delta x(x, y) + \frac{\partial}{\partial y} \Delta y(x, y) \right] = b(x, y). \quad (A.11)$$

which can be rearranged in the form,

$$A \rho(x, y) = b(x, y). \quad (A.12)$$

This can be solved by discretisation and by solving the matrix equations using a least-squares technique. Multiplying both sides of the equations by the transpose of A ,

$$(A^T \cdot A) \cdot \rho = A^T \cdot b \quad (A.13)$$

and multiplying through by $(A^T \cdot A)^{-1}$ results in,

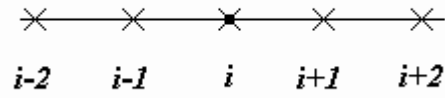
$$\rho = (A^T \cdot b) \cdot (A^T \cdot A)^{-1} \quad (A.14)$$

Using this technique to process large images requires long computing times. An improvement to the Poisson's solver however can be a finite difference approximation method. A system that can be used for this task is a fourth order scheme and is described next.

A.2.2 Finite Difference Approximation

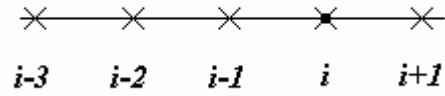
A Fourth Order scheme can be used across the five density gradient matrices that were obtained experimentally. The equations and nodes used for the different mesh-point in the gradient matrix are as follows,

(a) 4th Order Central



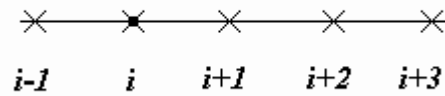
$$\frac{\partial n}{\partial x} \approx \frac{n_{i-2} - 8n_{i-1} + 8n_{i+2} - n_{i+2}}{12m_{xy}} \quad (6.15)$$

(b) 4th Order Backward (1)



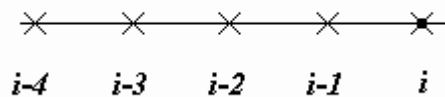
$$\frac{\partial n}{\partial x} \approx \frac{-n_{i-3} + 6n_{i-2} - 18n_{i-1} + 10n_i + 3n_{i+1}}{12m_{xy}} \quad (6.16)$$

(c) 4th Order Forward (1)



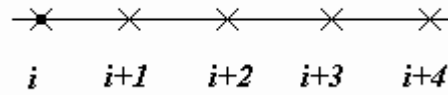
$$\frac{\partial n}{\partial x} \approx \frac{-3n_{i-1} - 10n_i + 18n_{i+1} - 6n_{i+2} + n_{i+3}}{12m_{xy}} \quad (6.17)$$

(d) 4th Order Backward (2)



$$\frac{\partial n}{\partial x} \approx \frac{3n_{i-4} - 16n_{i-3} + 36n_{i-2} - 48n_{i-1} + 25n_i}{12m_{xy}} \quad (6.18)$$

(e) 4th Order Forward (2)



$$\frac{\partial n}{\partial x} \approx \frac{-25n_i + 48n_{i+1} - 36n_{i+2} + 16n_{i+3} - 3n_{i+4}}{12m_{xy}} \quad (6.19)$$

The spacing between the mesh points is denoted by m_{xy} in pixels. The same discretised equations can be used in the y-direction. The resulting system of equation is

$$A \rho(x, y) = b(x, y). \quad (6.20)$$

These can be solved using the sparse matrix method. The non-zero elements of A are assigned to the sparse matrix and the systems of equations are solved by the least squares method.

For an axis-symmetric flow field (such as that around a cone in a uniform flow), the gradient of refractive index is not constant and an Abel-transform inversion (Klinge et al., 2000) can be performed to reconstruct the density field from the beam deflection information.

Python Implementation of the BOS Algorithms

B.1 Introduction

This section of the appendix explains the functions used for the processing of the pair of BOS images. These functions are implemented in the Python programming language, embedded in the BOSGUI program. Python programming has been chosen for this task because it is developed as an open source project, making it free for use in the university. It has an extensive collection of libraries developed for various scientific computing tasks, one of which is the Python Image Library (PIL) that is used to read and manipulate the images for BOS image processing. The routines presented here were developed from the Matlab routines written by Prof. T. Rösger and his colleagues at ETH, Zurich. The author spent six weeks in Zurich, working under the direction of Rösger, to develop the Python codes. An example of using the program to process the images shown in section 5.4.1 is given in Appendix C. Appendix D contains the Python source code contained in this program. The Matlab code used to generate a round dot pattern given in Appendix E.

B.2 The BOSGUI Program

We will start describing the development of the program by first introducing the powerful numerical packages NumPy and PIL. Then the core modules, **estimatecoarsechift**, **simplepiv**, **slidesum** and **gausspeak**, used in BOSGUI are explained.

B.2.1 The Numerical Python Package (NumPy)

The Scientific Python extensions (NumPy) is a set of extensions to the Python programming language which allows Python programmers to efficiently manipulate large sets of objects organized in grid-like fashion. These sets of objects are called arrays, and they can have any number of dimensions: one-dimensional arrays are similar to standard Python sequences; two-dimensional arrays are similar to matrices from linear algebra. Apart from the new multidimensional array type and basic array operations and manipulations, NumPy comes with a set of libraries that support Fast Fourier transforms, least square calculations and statistical evaluations.

B.2.2 The Python Imaging Library (PIL)

The Python Imaging Library (PIL) used with the Python language, allows opening, manipulating, and saving of many different image file formats. To read an image file from disk, the *open* function in the Image module is used. The example code given here was taken from the BOSGUI program. The other modules developed in this image processing exercise will be explained similarly. The reference file is a JPEG image in RGB format and is converted to black and white, 8-bit pixel format as follows;

```
import Image
refImage = Image.open('ref.jpg')
ref.convert('L')
```

At this point, the reference image, 'ref' is a greyscale image. The size of this image is the resolution of the CCD chip used to acquire the image. In this thesis, all images were recorded at a resolution of 1.92 mega pixels or 1200 pixels in the y-axis and 1600 in the x-axis. A description of how a digital image is assigned an integer value is explained in

Fig.B.1. This example uses a background pattern of horizontal black lines. Each pixel is assigned an 8-bit integer (0–255), representing the average intensity of light over the pixel. A black pixel has value zero, a white pixel has value 255, and gray values lie in between. This data is stored on a computer as a matrix of integers.

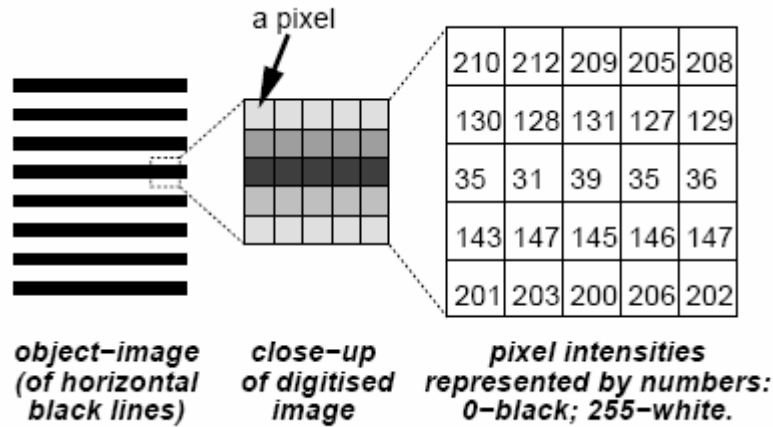


Fig B.1. Assigning values according to the pixel intensities (Jain, 1989).

In the BOSGUI program, these integer values are read and converted to numeric data using the `getdata()` attribute and are stored in a NumPy array. `getdata()` returns a flattened 1-D array that is reshaped to the array size of the image. The code used in BOSGUI is as follows;

```
import numpy
refdata = numpy.array(ref.getdata())
xsize ,ysize = refImage.numpy.size
refdata = numpy.reshape(refdata, (ysize,xsize))
```

The flow image data is extracted similarly. The next step in the BOS image processing is to crop a small region within the two images, where no disturbance is expected. The function *estimate coarse shift* is used to detect any noise in the data. This procedure is described in section 3.3.1.

B.2.3 The *Estimate coarse shift* module

A sample box with starting coordinates, (x_0, y_0) and ending at coordinates (x_1, y_1) is selected. A click of the left mouse button starts marking a sample box on the reference image and dragging with the left button held down alters the sample box dimensions.

B.2. The BOSGUI Program

Then releasing the button finalizes the sample box size. The box is restricted to a square shape to ensure a smooth cross-correlation procedure. The code used to make the square box is;

```
dx = x1 - x0
dy = y1 - y0
if dx > dy:
    dy=dx
if dy > dx:
    dx=dy
y1 = y0 + dy
x1 = x0 + dx
```

The coordinates of the sample box are;

```
sampleBox = tuple([int(x0), int(y0), int(x1), int(y1)])
```

Two boxes defined by coordinates of the sample box are cropped in both reference and flow images and the data are cross-correlated using the *correlate2d* function as follows;

```
from scipy.signal import correlate2d
corrData = correlate2d(refsmalldata, testsmalldata)
```

Fig. B.2 shows a surface plot of the correlated data. The location of the peak value on the plot relative to the centre of the sample square corresponds to the amount the dots were displaced.

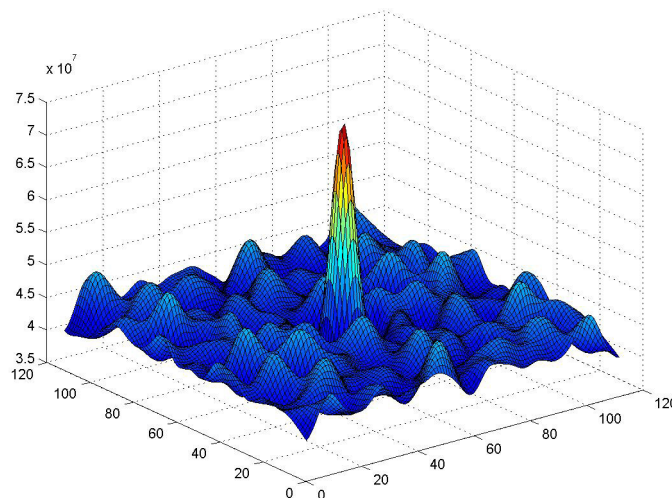


Fig. B.2. Surface plot of the correlation map.

The indices of this peak correlation value are determined and used to calculate the shifts in the vertical and horizontal directions. $ibig$ and $jbig$ are the x and y coordinates of the location of the correlation peak. The shifts are calculated as follows;

```
xshift, yshift = xsize - 1 - ibig, ysize - 1 - jbig
```

The flow image is then moved according to the number of shifted pixels detected.

```
testImage = testImage.crop(xshift, yshift, xsize, ysize)
```

The reference image and test image are at this stage corrected for noise and the next step in the processing is to determine the horizontal and vertical displacements due to density gradient between the reference and the flow image. The displacement data were corrected for noise by subtracting the mean horizontal and vertical vector values located outside the density gradient region from the original data.

B.2.4 Evaluating vector displacements

The PIV modules, ‘simplepiv’, ‘slidesum’ and ‘gausspeak’ were written to determine the displacement vectors and their position in the flow field. First, the shifted test image was converted to numeric data and the two image data were cross-correlated.

```
testdata = numpy.array(testImage.getdata())  
xsize, ysize = testImage.numpy.size  
testdata = numpy.reshape(testdata, (ysize, xsize))
```

The function ‘correlate2d’, which was used in the noise detection procedure performs slowly for the correlation of a whole image. Instead, a normalized cross-correlation employing the Fast Fourier transform functions in Python is used. This is explained in section B.2.5.

B.2.5 The ‘simplepiv’ module

This module is used to evaluate the vector displacements u , v and their position x and y in the flow field. The inputs are the search window size, w_{xy} , the maximum search size, m_{xy} and the window spacing, s_{xy} . The image data is divided into sub windows

(interrogation windows) and a normalized cross-correlation map is calculated for each window. The interrogation window is a sliding template that is moved throughout the image, the size of which is determined from the user inputs integer values. The size of the correlation map, *CSZ* is

$$CSZ = 2 * m_{xy} + 1,$$

and the size of the sliding template is

$$wsz = w_{xy} - CSZ + 1.$$

The peak value and its location on the correlation map for each sub-window are then evaluated. The start and end positions for the procedure are specified as illustrated in Fig B.3. The interrogation window is cropped from the reference and test data and the integer values, *height* and *width* are the size of the image data.

```
height, width = testdata.shape
left= 0
right= width - wxy
top= 0
bot= height - wxy

nx= -1
for xoff in r_[left:right+1:sxy]:
    nx = nx + 1
    ny = -1
    for yoff in r_[top:bot+1:sxy]:
        ny = ny + 1
        A= refdata[yoff+mxy:yoff-mxy+wxy,xoff+mxy:xoff-mxy+wxy]
        B= testdata[yoff:yoff+wxy,xoff:xoff+wxy]
```

A and B are the cropped sub-windows from the reference and the image data. The variance and the sum of all elements in the A matrix for each sub-window are then found.

```
from scipy.stats import var
sumA= sum(sum(A))
```

```
varA= var(A,axis=None)*(wsz*wsz-1)
```

The variance and sum of B were calculated using the module '*slidesum*' to return a matrix of the size of the correlation map.

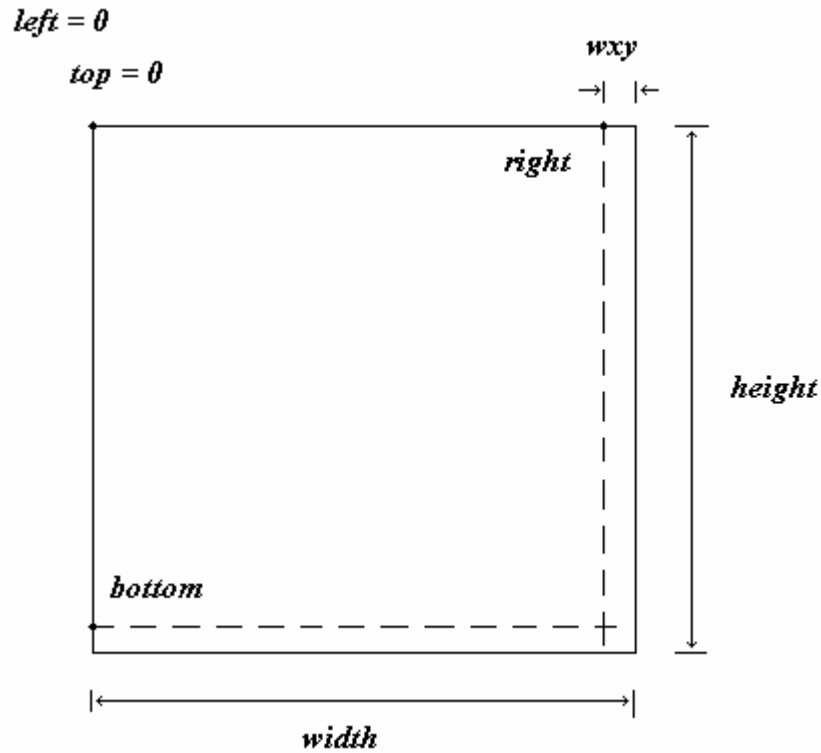


Fig. B.3. Setting the boundaries for the correlation procedure.

B.2.6 The '*slidesum*' module

The *slidesum* function cumulatively sums the input matrix B in the x and y directions and reduces it to the size of the correlation map. For this, the matrix B is padded with zeros, as seen in equation B.1. The elements are then cumulatively summed column-wise. (equation B.2). The zero padding procedure is done to ensure that the two matrices are of different sizes. If both input images are of the same size, the part of the shifted image, which contributed to the correlation data, will be smaller for large shifts.

$$bb = \begin{pmatrix} 0 & \dots & 0 & 0 \\ \vdots & \begin{pmatrix} b_{11} & \dots & b_{1nb} \\ \vdots & \ddots & \vdots \\ b_{mb1} & \dots & b_{mbnb} \end{pmatrix} \\ 0 \\ 0 \end{pmatrix}, \text{ where } B = \begin{pmatrix} b_{11} & \dots & b_{1nb} \\ \vdots & \ddots & \vdots \\ b_{mb1} & \dots & b_{mbnb} \end{pmatrix} \quad (\text{B.1})$$

$$b1 = \begin{pmatrix} 0 & 0 & 0 & \dots & 0 \\ 0 & b_{11} & b_{12} & \dots & b_{1n} \\ 0 & b_{11} + b_{21} & b_{12} + b_{22} & \dots & b_{1n} + b_{2n} \\ \vdots & \vdots & \vdots & & \vdots \\ 0 & b_{11} + b_{12} + \dots + b_{m1} & & & b_{1n} + b_{2n} + \dots + b_{mn} \end{pmatrix} \quad (B.2)$$

The Python commands for the zero padding procedure and cumulative sum procedures are;

```
nb,mb= B.shape
bb=vstack(((zeros((1,mb+1),dtype=float)),(hstack(((zeros((nb,1),dtype=float)),B))))))

b1= cumsum(bb,0)
```

b1 is then divided in two parts and the top is subtracted from the bottom as shown in equations B.3 and B.4. The number of rows of each of the sub-matrices is equal to that of the correlation map.

$$b1 = \begin{pmatrix} \left(\begin{matrix} b1_{top} \end{matrix} \right) \\ \left(\begin{matrix} b1_{bottom} \end{matrix} \right) \end{pmatrix} \quad (B.3)$$

$$b2 = \left(\left(\begin{matrix} b1_{bottom} \end{matrix} \right) - \left(\begin{matrix} b1_{top} \end{matrix} \right) \right) = \begin{pmatrix} b2_{11} & \dots & b2_{1n} \\ \vdots & \ddots & \vdots \\ b2_{csz1} & \dots & b2_{cszn} \end{pmatrix} \quad (B.4)$$

The Python commands is;

```
b2 = b1[n:wsz+1,:]-b1[0:wsz+1-n,:]
```

A similar cumulative sum is then performed on the new *b2* matrix row wise (equation B.5), then divided into two parts (equation B.6) and the left side subtracted from the right as shown in equation B.7.

$$b3 = \begin{pmatrix} b2_{11} & b2_{11} + b2_{12} & \dots & b2_{11} + b2_{12} + \dots + b2_{1n} \\ b2_{21} & b2_{21} + b2_{22} & \dots & \vdots \\ \vdots & \vdots & \ddots & \\ b2_{csz1} & b2_{csz1} + b2_{csz2} & \dots & b2_{csz1} + b2_{csz2} + \dots + b2_{cszn} \end{pmatrix} \quad (B.5)$$

$$b3 = \left(\left(\begin{pmatrix} b3_{left} \end{pmatrix} \right) \left(\begin{pmatrix} b3_{right} \end{pmatrix} \right) \right) \quad (B.6)$$

$$sumB = \left(\left(\begin{pmatrix} b3_{right} \end{pmatrix} \right) - \left(\begin{pmatrix} b3_{left} \end{pmatrix} \right) \right) \quad (B.7)$$

The corresponding Python code is;

```
b3 = cumsum(b2,1)
SumB = b3[:,m:ma+1]-b3[:,0:ma+1-m]
```

SumB is now reduced to the size of the correlation map. The function *slidesum* is again used to calculate the variance of B.

```
varB= slidesum(B**2,wsz,wsz)-(sumB**2)/(wsz*wsz)
```

The covariance of each sub-window pair is evaluated by first calculating the two-dimensional fast Fourier transforms of A and B, padded to the size of the sliding template, *wsz*. This is then used to evaluate the normalized cross-correlation map, *cmap*.

```
fft_A= fft2(A,shape=(wxy,wxy))
fft_B= fft2(B,shape=(wxy,wxy))
corrAB= real(iff2(conj(fft_A)*fft_B))
covAB = corrAB[0:CSZ,0:CSZ] - (sumB*sumA)/(wsz*wsz)
cmap= covAB/sqrt(varA*varB)
```

The maximum integer value in the cross correlation map and the *x* and *y* coordinates, *xpeak* and *ypeak* of this maximum value are calculated. The apparent pixel shift in the *x* and *y* directions relative to the sub-window centre can hence be evaluated.

A better estimation of this shift is possible by fitting a Gaussian curve to the values in the neighbourhood of the maximum peak. This ‘sub-pixel interpolation’ procedure is not possible when the peak is located at the edge in the correlation map.

B.2.7 The ‘gausspeak’ module

The description of this procedure is given in section 3.3.2.4. It was applied in this module to locate a peak intensity value on the correlation map to sub-pixel accuracy. The interpolated polynomial function used in BOSGUI is

$$p(x,y) = \exp(a + bx + cy + dx^2 + exy + fyy),$$

with constants a , b , c , d , e and f . This function describes the Gaussian curve that is fitted to values surrounding the correlated peak. The maximum position of this interpolated function is the new peak. The position of this Gaussian peak value is only used to calculate the apparent pixel shift that occurred between the two images sub windows if the condition,

$$\text{gaussian peak value} / \text{correlated peak value} < 0.98$$

and

$$\text{gaussian peak value} / \text{correlated peak value} > 2.0$$

are valid. Otherwise, the correlated peak value obtained from the cross-correlation procedure is used to find the estimate of the vector displacement. For each sub window, the horizontal displacement value is assigned to the previously initialised matrix u . The values for the vertical displacement vectors and the coordinates x and y are assigned similarly. The matrices are initialised by floating point zeros, the size of which corresponds to the number of correlated windows possible in the boundary set in Fig. B.3. The number of correlated windows in the x -direction is

$$n_x = \text{int}((\text{bot-top})/sxy) + 1,$$

and the number of correlated windows in the y -direction is

```
n_y = int((right-left)/sxy)+1.
```

The matrix initialisation is done as follows;

```
x = zeros((n_y,n_x),dtype=float)  
y = zeros((n_y,n_x),dtype=float)  
u = zeros((n_y,n_x),dtype=float)  
v = zeros((n_y,n_x),dtype=float)
```

The *quiver* function from the matplotlib module was used to display the arrows of the magnitude vector, $\sqrt{u^2 + v^2}$ at every location, (x, y) .

The next step in the evaluation consists of generating schlieren-like images to obtain a grey colour map of the gradient of the density field. The *contourf* function in the Python program is used to generate the contour plots of using the displacement vectors in each direction. The number of contour levels, *vv* and *uu* can be specified.

```
from pylab import contourf, gray  
contourf(x,y,u,uu,cmap=cm.gray)  
contourf(x,y,v,vv,cmap=cm.gray)
```

Acquiring the Images and Post-Processing using the BOSGUI Program

C.1 Introduction

A description of using the camera software to acquire the reference and the flow images is given in this section. An example of using the BOSGUI program to process the images of the sharp 20° half-angled cone follows.

C.2 Acquiring the Reference and Flow images

The devices are connected as shown in the block diagram in Fig. 5.3.

C.2.1 The Camera software settings

The scorpion PGR camera used for the results presented in this thesis can be set to a shutter exposure time ranging between 10 μ s and 66.68 ms at a frame rate of 15 Hz. The shutter exposure is set in the *Camera Control* menu in the *PGR Flycapture* software as shown in Fig C.1. The steps given next explain how to set the camera to a shutter exposure of 30 μ s.

1. In the *Format and Frame Rate* menu, select the *1600 x 1200 / 8-bit Y8* format. Select a *Frame Rate* of *15Hz*. (see Fig B.1)

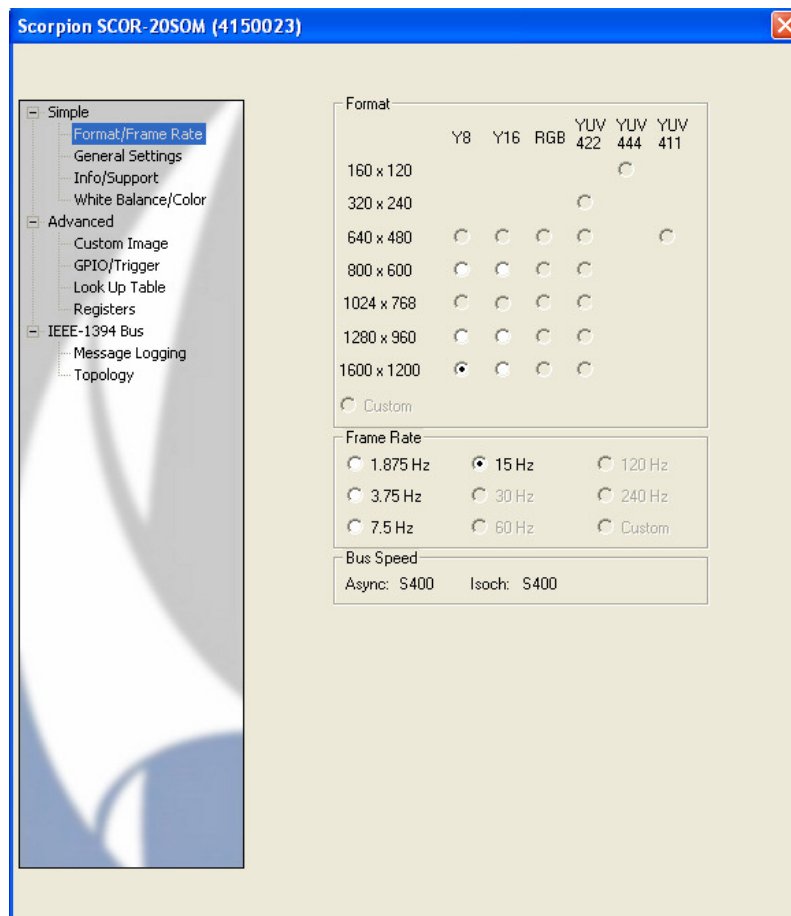


Fig. C.1. Format and frame rate settings.

Acquiring the Images and Post-Processing using the BOSGUI Program

2. In the *Trigger* menu, check Trigger Mode On/off as shown in Fig C.2. This is done to ensure the camera is on the external trigger mode and will open its shutter only when a signal is sent to it. All the other parameters in this menu are left at their default values.

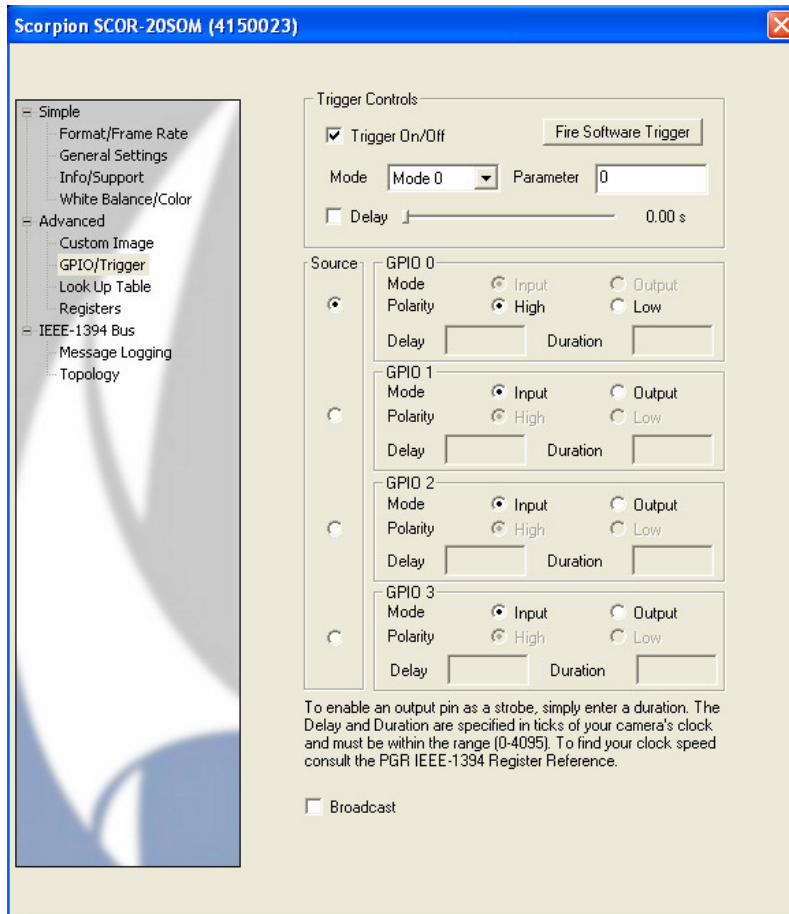


Fig C.2. Switching ON the external trigger mode.

3. In the *General Properties* menu, adjust the *shutter* speed using the slider control as shown in Fig C.3. For more granularity¹, the *Absolute mode* option can be unchecked and the keyboard used to increase or decrease the value.
4. Set the *Brightness* and *Exposure* as shown in Fig. C.3 and check the *On/Off* option. These options can be saved by clicking on the *save* button.

¹ The shutter slider control does not always have enough resolution for very fine shutter adjustments. The ABS_VAL_SHUTTER register is accessed by un-checking the *Absolute mode* feature for fine adjustments.

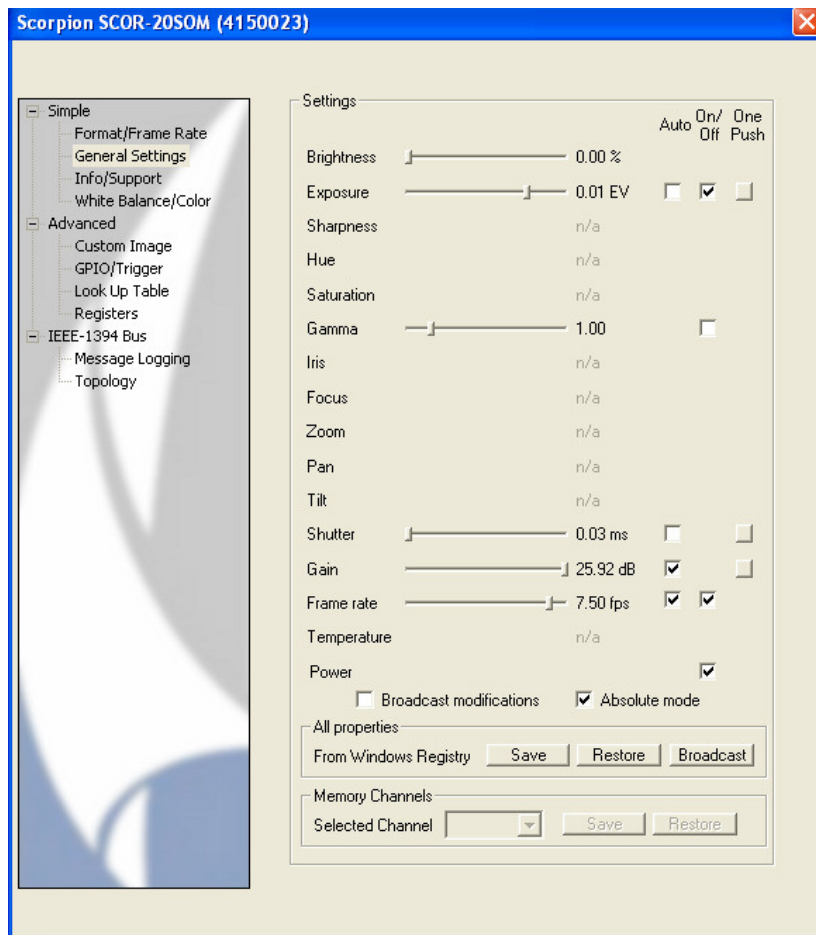


Fig. C.3. Brightness, Exposure and Shutter exposure settings.

5. In the *Registers* menu, set register *614 H* to *Value 00 00 00 00* as shown in Fig C.4. Similarly, set register *61C H* *Value 80 00 00 00*.

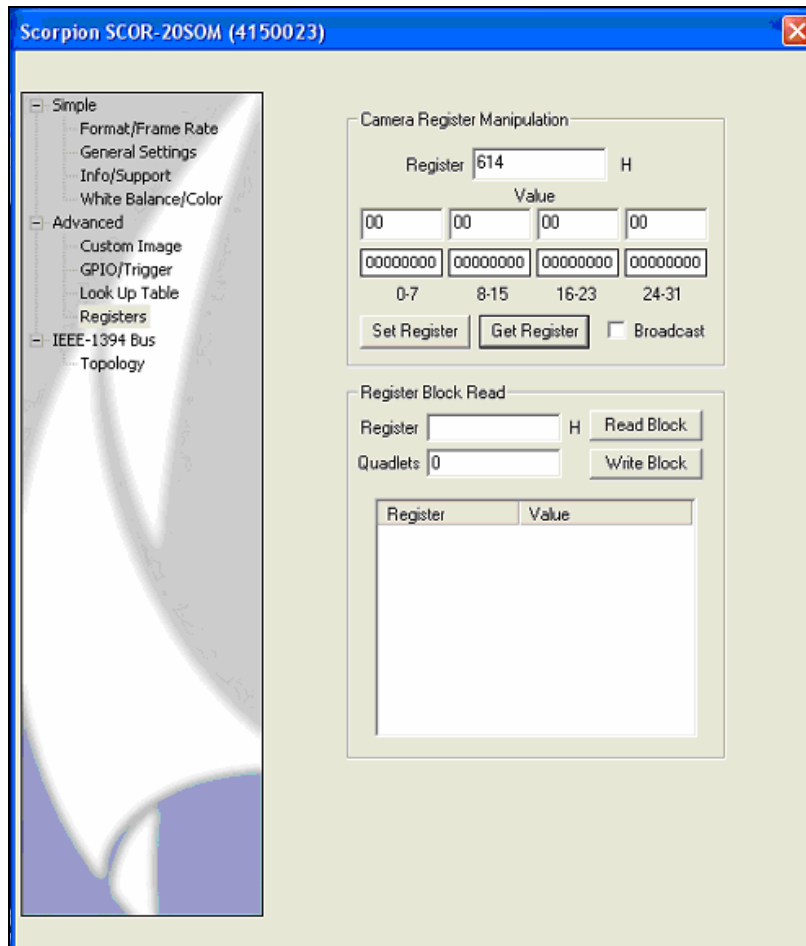


Fig. C.4. Register 614H settings.

C.2.2 The Delay/Pulse Generator settings

The manual trigger mode of the delay generator is used when recording the reference image and the external trigger is used for recording the flow image.

1. Set the trigger to *Ext* and the *Threshold Voltage* to approximately 20 % of the maximum voltage of the trigger signal.
2. Set the trigger to *+(positive)* slope to trigger the delay generator on the rising edge of the signal.
3. Select the *High Impedance (Z)* option.

C.2.3 The Reference Image

The reference image of the dot background is taken after the tunnel is evacuated and the vents to the pump are closed, just before the shock tube and reservoir are filled. The

C.2. Acquiring the Reference and Flow Images

reference image is taken only when the tunnel is pumped down, just before firing. The following guidelines should be observed to capture the reference image.

1. Section 5.3.1 and 5.3.2 can be followed to set the trigger delays.
2. Set the *Trigger* on the delay generator to *Single Shot* mode.
3. Press the *Trigger* button on the delay generator and “*Press EXC to execute*” will be seen on the display window of the delay generator.
4. Push The *EXC* button on the delay generator to send a signal to the camera and the light source.
5. Save the image in either *.ppm*, *.jpeg* or *.bmp* format

C.2.4 The Flow Image

The flow image is captured when the flow is established over the test object in the test section. The following guidelines should be observed to acquire a flow image.

1. Set the *Trigger* on the delay generator back to *Ext* after capturing the reference image to allow triggering from an external source.

Once the tunnel is fired, the trigger signal will trigger the delay generator, which will, in turn, trigger the camera and light source. The flow image can then saved in the desired format.

C.3 Using the BOSGUI program

This section describes the python implementation of the Background Oriented Schlieren image processing technique in a Graphic User Interface program, BOSGUI.

Python can be operated on various operating systems. In this thesis, the package Python Enthought Edition 1.0.0 (<http://www.enthought.com>) was installed on a Pentium 4, 3.2 GHz machine with 1.0 GB RAM running Microsoft XP. The Enthought package is available for free download from the Enthought. Inc website. Python version 2.4.3 and the packages, NumPy 0.9.9 and PIL 1.1.5 were used for the numerical calculations and TkInter for graphical user interface capabilities. These packages are included in the Python Enthought Edition 1.0.0.

The BOSGUI python file can be saved anywhere on the hard drive (preferably in the folder where the image files are saved) and double clicking on the Python icon starts the program, as shown in Fig C.5.

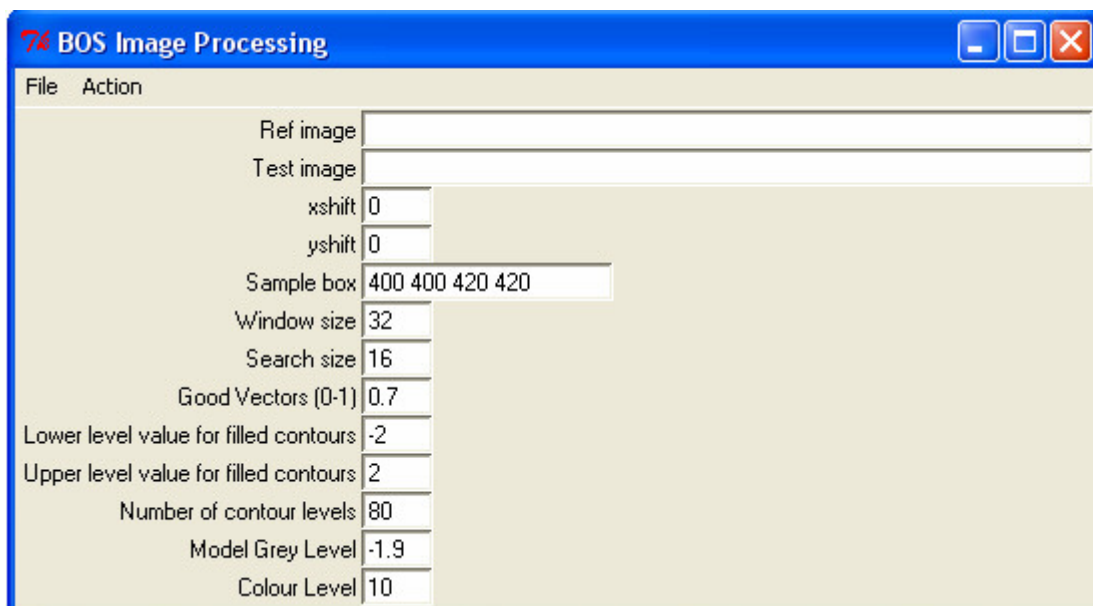
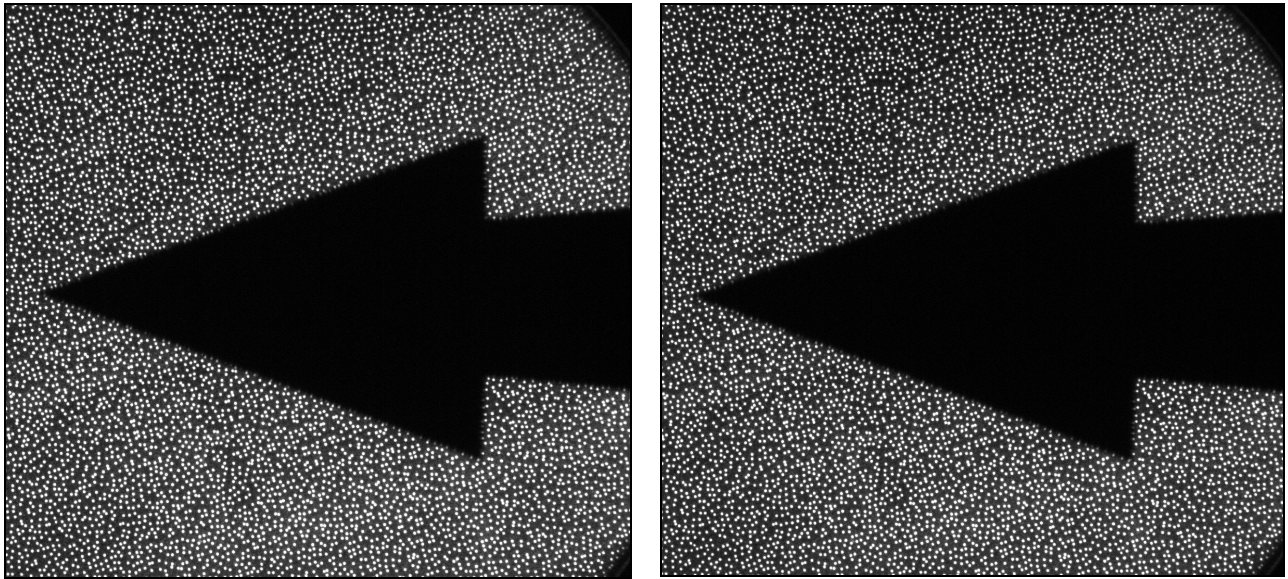


Fig. C.5. The BOS image processing program main menu.

The reference and flow image files are opened (see Fig. C.6) by clicking on the *File* menu on top window corner. By following the eight tasks found under the *Action* menu shown in Fig C.7, the two images can be processed



(a) Reference Image

(b) Flow Image

Fig. C.6. Cone model in the Drummond Tunnel test section.

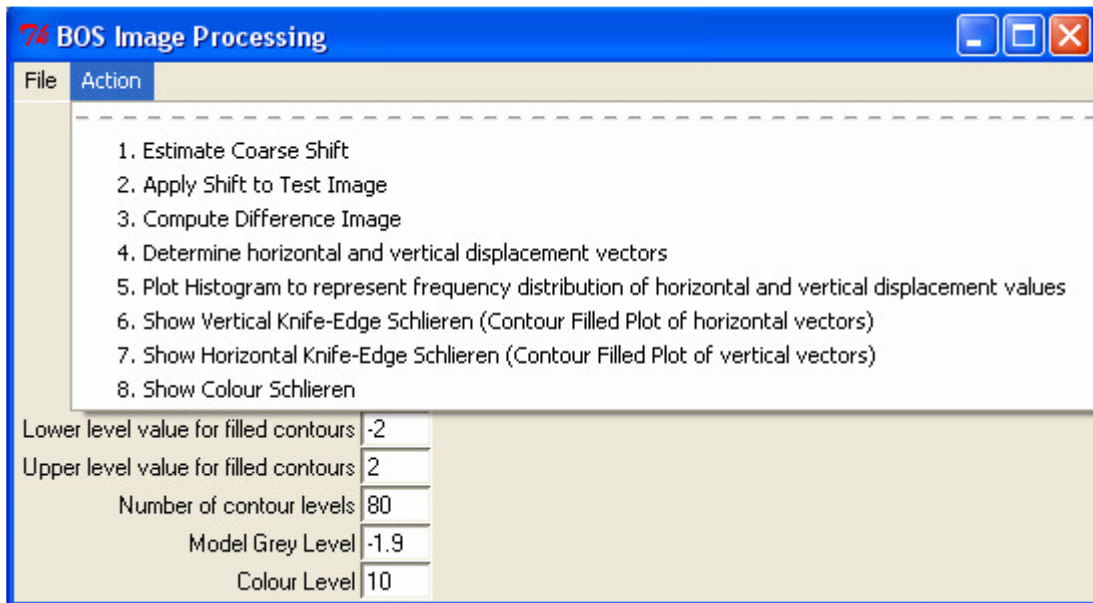


Fig. C.7. The required actions to process the two images.

C.3.1 Estimating un-due disturbances between the reference and flow images

A sample box in the reference image is interactively selected in a region outside where disturbances are not expected to occur. The two boxes shown in Figs. C.8 (a) and C.8 (b) represent the undisturbed region selected in the reference and flow images. The coordinates of the sample box are displayed on the main menu.

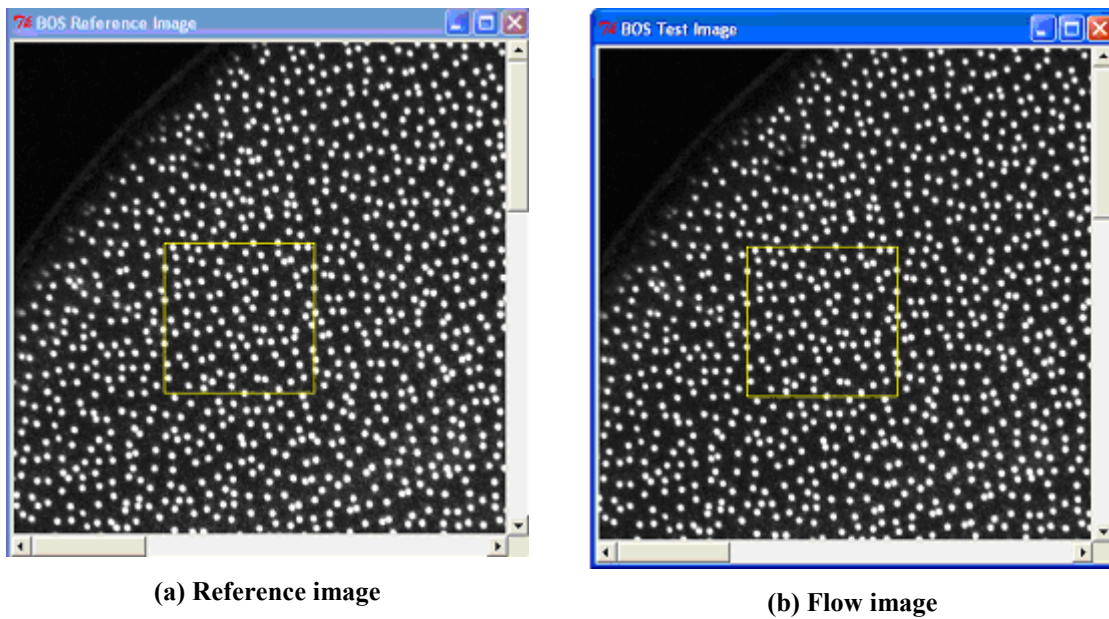


Fig. C.8. Choosing a sample box window outside in the undisturbed region.

Clicking on *Estimate Coarse Shift* option calculates the pixel shift (if any) between the two boxes. The detected $xshift$ and $yshift$ will be displayed on the main menu. Option 2 is used to shift the test image by the amount detected. These two steps can be skipped if it known that no undue shifts occurred between the two images. An absolute difference image between the reference and the corrected flow image (see Fig. C.9) can be generated next using Option 3 in the action menu. This image can be saved as a *.png* file by clicking on *Save Difference Image* in the File menu.

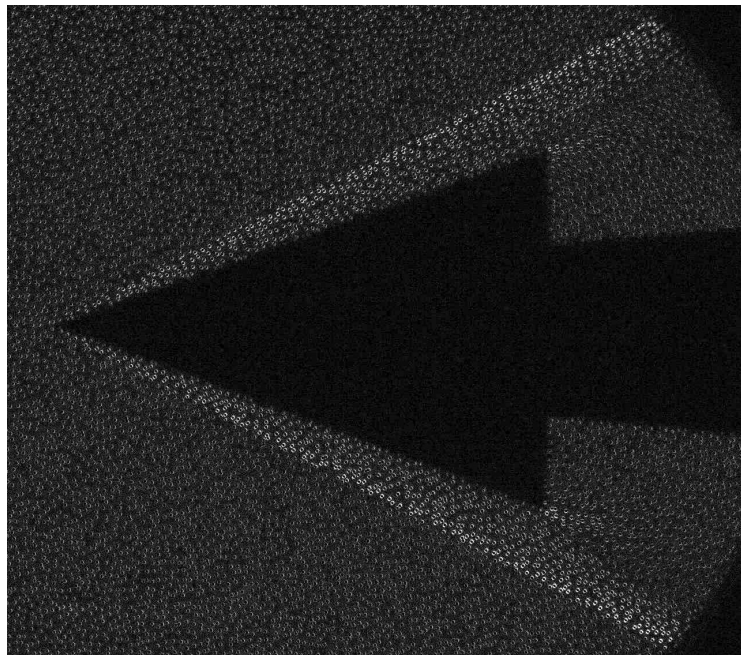


Fig. C.9. Absolute difference image between the reference and corrected flow images.

The next step in the BOS processing is to determine the horizontal and vertical displacement vectors throughout the whole image.

C.3.2 Evaluating the horizontal and vertical displacements due to density gradients

Clicking on the Action 4 in *BOSGUI Action* menu executes this procedure and plots the absolute values of the displacement vectors for each interrogation window as shown in Fig. C.10. The interrogation window size and step size default values are 32 and 16. These values can be altered on the main menu.

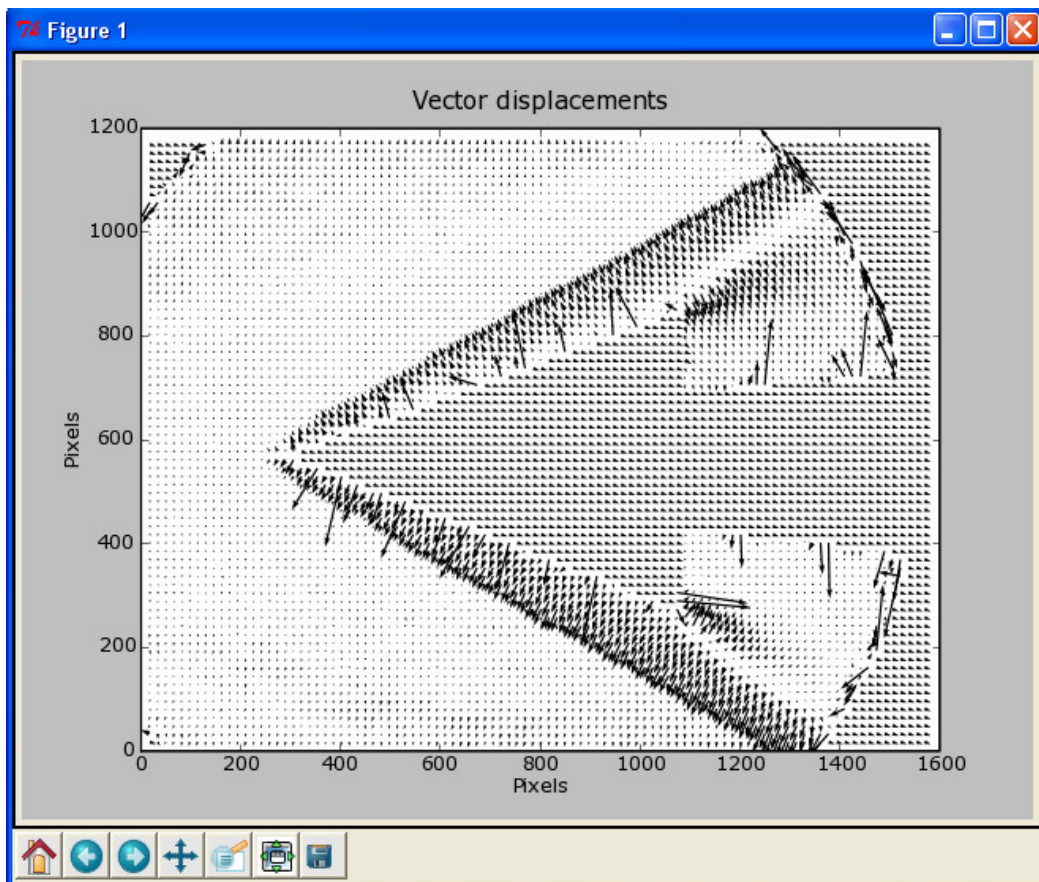


Fig. C.10. Plot of the vector displacement for an interrogation window size of 32 pixels and step size 12 pixels.

This result is then processed to obtain a dark/grey representation of the density gradient field. A histogram representing the distribution of the displacement vectors (see Fig. C.11) is generated to determine the range between which to contour the data. Clicking on task 6 and 7 in the Action menu generates the contour plots in Figs. C.12 and C.13. The model grey level is the value assigned to the erroneous vectors in the model and outside the flow field. For the horizontal schlieren case, this grey value is assigned as

C.3 Using the BOSGUI program

slightly higher than the value assigned to 'lower value for filled contours'. For the vertical schlieren case, the grey value is assigned as slightly lower than the value given to 'higher value for filled contours'. This procedure will ensure that this region appears darkest in the contour plot, resulting in a good contrast grey plot. The *Good Vectors* option in the main menu can be used to remove erroneous vectors in the flow field and the value entered has to be between zero and one.

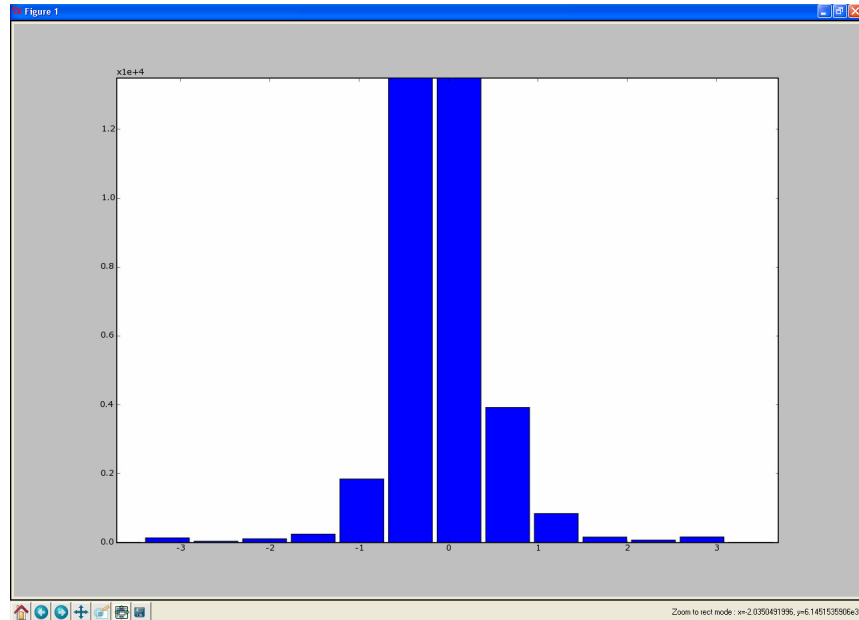


Fig. C.11. Histogram representing the distribution of vertical displacement vectors.

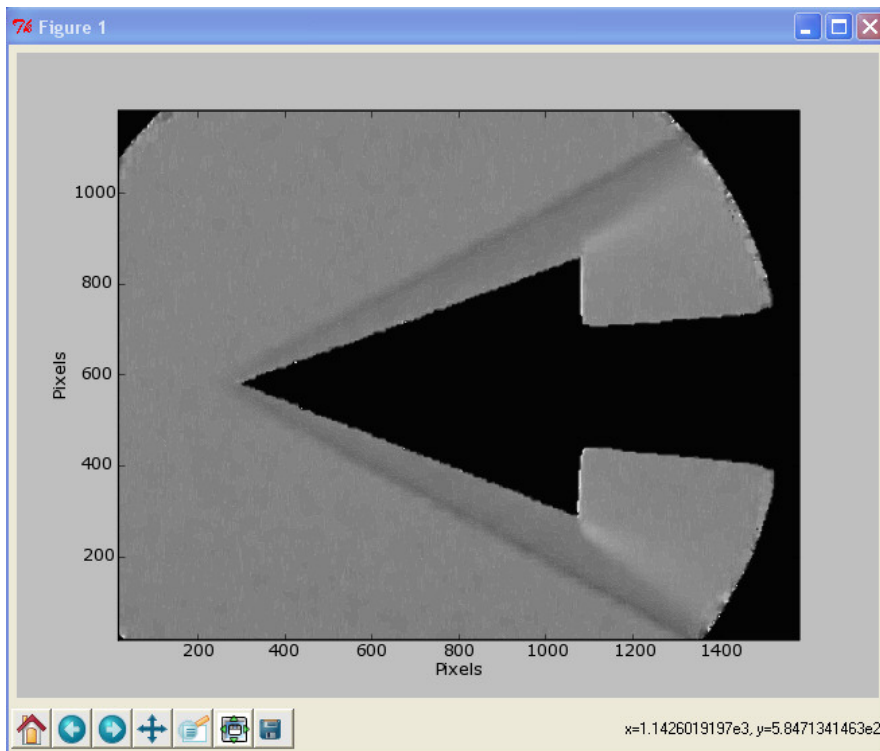


Fig.C.12. Horizontal knife-edge schlieren.

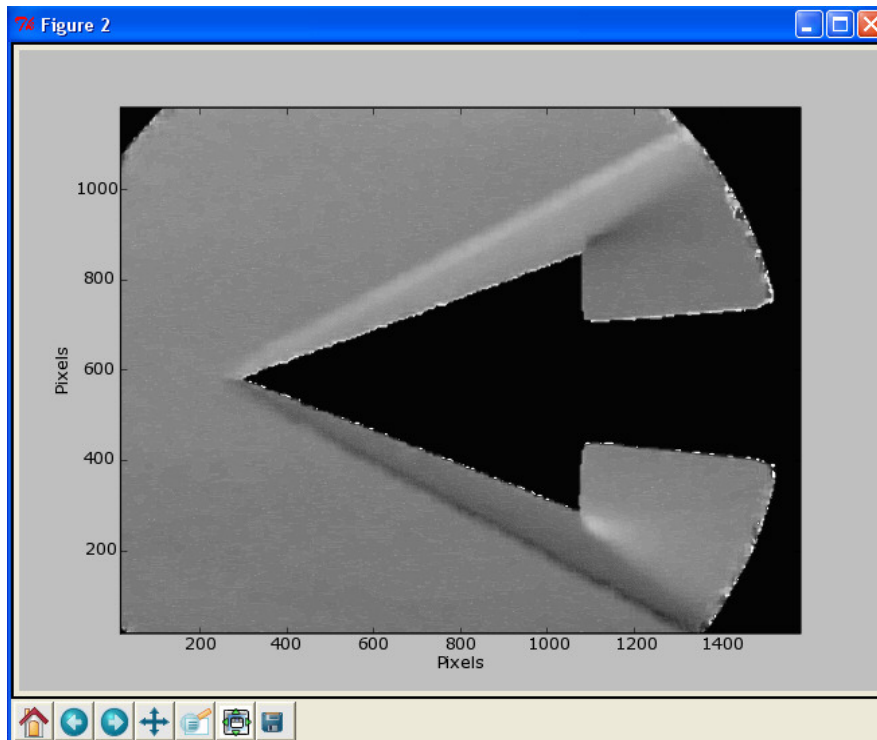


Fig.C.13. Vertical knife-edge schlieren.

Clicking on task 8 in the Action menu will generate a colour schlieren image as shown in Fig. C.14. The colour level can be adjusted on the main menu.

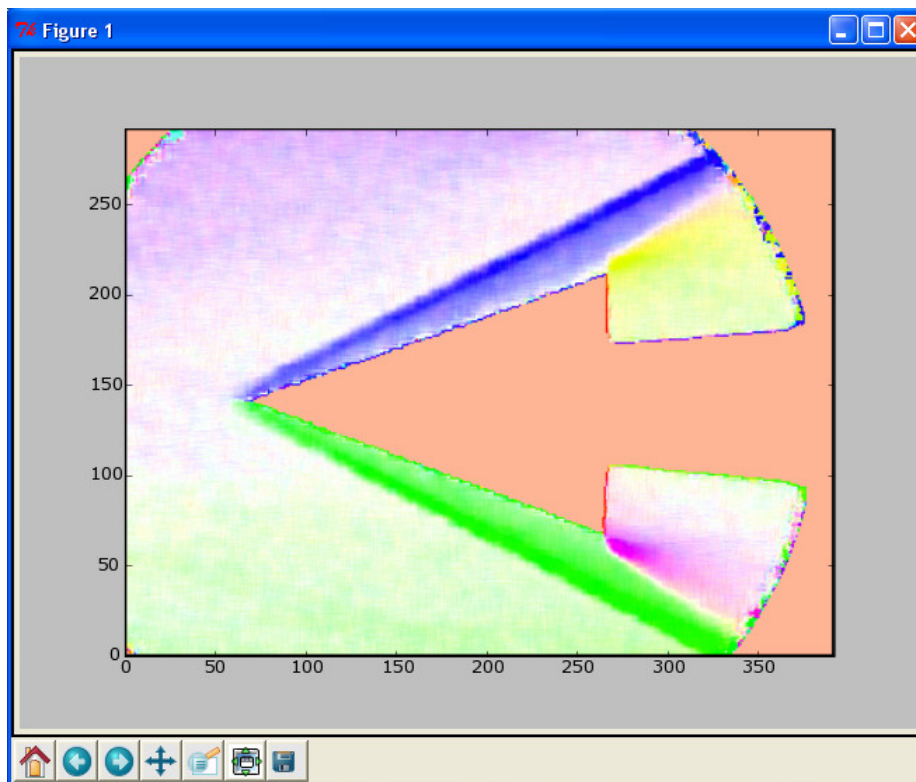


Fig.C.14. Colour Schlieren Image.

APPENDIX D

BOSGUI.py Code

```
# bosgui.py
# Starter GUI for BOS functions
#
# PJ, 17-Dec-05 starting sample
#
# Dwishen Ramanah, 12-Jan-2007 Version 1.0

import sys
import Tkinter, tkFileDialog, tkSimpleDialog, tkMessageBox
import Image, ImageTk, ImageChops, ImageOps
import Numeric
try:
    from scipy.signal.signaltools import correlate2d
    from scipy.signal.signaltools import medfilt
except:
    print "scipy did not load correctly..."
    print "To get correlation2d and medfilt functions, we need Scipy."

#-----
# Global data
refImage = None; refCanvas = None
x0 = 400; y0 = 400; x1 = 420; y1 = 420

# upper-left and lower-right coordinates of the sample box
# The numbers above suit one of Sreekanth's images.

testImage = None; testCanvas = None
diffImage = None; diffCanvas = None

#-----

def main():
    global root
    root = Tkinter.Tk()
    setupGUImenus(root)
    layoutMainWindow(root)
    root.mainloop()
    return

def layoutMainWindow(root):
    """
    The main window consists of a menubar and some labeled entry boxes.
    """
    global refFileName, testFileName
    global xshiftVar, yshiftVar, sampleBoxVar, sxyVar,
    wxyVar, lowerLevelVar, \
    upperLevelVar, numcontourVar, modelgreylevelVar, goodvectorsVar, colourlevelVar
```

```

global x0, y0, x1, y1

refFileName = Tkinter.StringVar()
testFileName = Tkinter.StringVar()
sampleBoxVar = Tkinter.StringVar()
sampleBoxVar.set("%d %d %d %d" % (x0, y0, x1, y1))

xshiftVar = Tkinter.IntVar(); xshiftVar.set(0)
yshiftVar = Tkinter.IntVar(); yshiftVar.set(0)

wxyVar = Tkinter.IntVar(); wxyVar.set(32)
sxyVar = Tkinter.IntVar(); sxyVar.set(16)

lowerLevelVar = Tkinter.DoubleVar(); lowerLevelVar.set(-2)
upperLevelVar = Tkinter.DoubleVar(); upperLevelVar.set(2)
numcontourVar = Tkinter.IntVar(); numcontourVar.set(80)
modelgreylevelVar = Tkinter.DoubleVar(); modelgreylevelVar.set(-
1.9)
goodvectorsVar = Tkinter.DoubleVar(); goodvectorsVar.set(0.7)
colourlevelVar = Tkinter.DoubleVar(); colourlevelVar.set(10)

#
root.title("BOS Image Processing")
f = Tkinter.Frame(root, borderwidth=1)
f.pack(expand=1, fill="both")
#
lab = Tkinter.Label(f, text="Ref image")
entry = Tkinter.Entry(f, width=60, textvariable=refFileName)
lab.grid(row=0, column=0, sticky='e')
entry.grid(row=0, column=1, sticky='w')
#
lab = Tkinter.Label(f, text="Test image")
entry = Tkinter.Entry(f, width=60, textvariable=testFileName)
lab.grid(row=1, column=0, sticky='e')
entry.grid(row=1, column=1, sticky='w')
#
lab = Tkinter.Label(f, text="xshift")
entry = Tkinter.Entry(f, width=5, textvariable=xshiftVar)
lab.grid(row=2, column=0, sticky='e')
entry.grid(row=2, column=1, sticky='w')
#
lab = Tkinter.Label(f, text="yshift")
entry = Tkinter.Entry(f, width=5, textvariable=yshiftVar)
lab.grid(row=3, column=0, sticky='e')
entry.grid(row=3, column=1, sticky='w')
#
lab = Tkinter.Label(f, text="Sample box")
entry = Tkinter.Entry(f, width=20, textvariable=sampleBoxVar)
lab.grid(row=4, column=0, sticky='e')
entry.grid(row=4, column=1, sticky='w')
#
lab = Tkinter.Label(f, text="Window size")
entry = Tkinter.Entry(f, width=5, textvariable=wxyVar)
lab.grid(row=5, column=0, sticky='e')
entry.grid(row=5, column=1, sticky='w')
#
lab = Tkinter.Label(f, text="Search size")
entry = Tkinter.Entry(f, width=5, textvariable=sxyVar)
lab.grid(row=6, column=0, sticky='e')
entry.grid(row=6, column=1, sticky='w')
#
lab = Tkinter.Label(f, text="Good Vectors (0-1)")
entry = Tkinter.Entry(f, width=5, textvariable=goodvectorsVar)

```

```

lab.grid(row=7, column=0, sticky='e')
entry.grid(row=7, column=1, sticky='w')
#
lab = Tkinter.Label(f, text="Lower level value for filled
contours")
entry = Tkinter.Entry(f, width=5, textvariable=lowerLevelVar)
lab.grid(row=8, column=0, sticky='e')
entry.grid(row=8, column=1, sticky='w')
#
lab = Tkinter.Label(f, text="Upper level value for filled
contours")
entry = Tkinter.Entry(f, width=5, textvariable=upperLevelVar)
lab.grid(row=9, column=0, sticky='e')
entry.grid(row=9, column=1, sticky='w')
#
lab = Tkinter.Label(f, text="Number of contour levels")
entry = Tkinter.Entry(f, width=5, textvariable=numcontourVar)
lab.grid(row=10, column=0, sticky='e')
entry.grid(row=10, column=1, sticky='w')
#
lab = Tkinter.Label(f, text="Model Grey Level")
entry = Tkinter.Entry(f, width=5, textvariable=modelgreylevelVar)
lab.grid(row=11, column=0, sticky='e')
entry.grid(row=11, column=1, sticky='w')
#
lab = Tkinter.Label(f, text="Colour Level")
entry = Tkinter.Entry(f, width=5, textvariable=colourlevelVar)
lab.grid(row=12, column=0, sticky='e')
entry.grid(row=12, column=1, sticky='w')
#
return

def setupGUImenus(root):
    "Establish the menu options and their function calls"
    menuBar = Tkinter.Menu(root)
    #
    fileMenu = Tkinter.Menu(menuBar)
    fileMenu.add_command(label="Open Reference Image",
command=openReferenceImage)
    fileMenu.add_command(label="Open Test Image",
command=openTestImage)
    fileMenu.add_command(label="Save Difference Image",
command=saveDifferenceImage)
    fileMenu.add_separator()
    fileMenu.add_command(label="Quit", command=quitDialog)
    menuBar.add_cascade(label="File", menu=fileMenu)
    #
    actionMenu = Tkinter.Menu(menuBar)
    actionMenu.add_command(label="1. Estimate Coarse Shift",
command=estimateCoarseShift)
    actionMenu.add_command(label="2. Apply Shift to Test Image",
command=shiftTestImage)
    actionMenu.add_command(label="3. Compute Difference Image",
command=showImageDifference)
    actionMenu.add_command(label="4. Determine horizontal and vertical
displacement\
vectors",
command=showVectorDisplacements)
    actionMenu.add_command(label="5. Plot Histogram to represent
frequency distribution\
of horizontal and vertical displacement values",
command=histogram_u_v)

```

```

        actionMenu.add_command(label="6. Show Vertical Knife-Edge Schlieren
(Contour\
Filled Plot of horizontal vectors)",
                               command=showContours_u)
        actionMenu.add_command(label="7. Show Horizontal Knife-Edge
Schlieren (Contour\
Filled Plot of vertical vectors)",
                               command=showContours_v)
        actionMenu.add_command(label="8. Show Colour Schlieren",
                               command=showColourSchlieren)
        menuBar.add_cascade(label="Action", menu=actionMenu)
        #
        root.config(menu=menuBar)
        return

#-----

def quitDialog():
    if tkMessageBox.askokcancel("Quit","Really quit?"):
        sys.exit()

def set_x0_y0_via_mouse(event):
    global sampleBoxVar, x0, y0, x1, y1
    canvas = event.widget
    x1 = x0 = canvas.canvasx(event.x)
    y1 = y0 = canvas.canvasy(event.y)
    sampleBoxVar.set("%d %d %d %d" % (x0, y0, x1, y1))
    canvas.delete("sample-box")
    try:
        testCanvas.delete("sample-box")
    except:
        pass
    return

def set_x1_y1_via_mouse(event):
    global sampleBoxVar, x0, y0, x1, y1
    canvas = event.widget
    x1 = canvas.canvasx(event.x)
    y1 = canvas.canvasy(event.y)
    if (x1 - x0) % 2 != 0: x1 += 1 # make even size
    if (y1 - y0) % 2 != 0: y1 += 1

    dx = x1 - x0 #make sqaure samplebox
    dy = y1 - y0
    if dx > dy: dy=dx
    if dy > dx: dx=dy
    y1 = y0 + dy
    x1 = x0 + dx

    sampleBoxVar.set("%d %d %d %d" % (x0, y0, x1, y1))
    canvas.delete("sample-box")
    canvas.create_line(x0, y0, x1, y0, x1, y1, x0, y1, x0, y0,
                      fill="yellow", tags="sample-box")
    try:
        testCanvas.delete("sample-box")
        testCanvas.create_line(x0, y0, x1, y0, x1, y1, x0, y1, x0, y0,
                              fill="yellow", tags="sample-box")
    except:
        pass # the testImage canvas may not exist
    return

def openReferenceImage():
    """

```

```

Interactive dialog to select the reference image.
"""
global refImage, refCanvas, refFileName
import os
fileName = tkFileDialog.askopenfilename()
if fileName:
    refImage = Image.open(fileName).convert('L') # to grayscale

    print "Finished reading image from file", fileName
    refCanvas = openImageWindow(refImage, 'BOS Reference \
Image-Filename: \''+os.path.basename(fileName), refCanvas)
    refFileName.set(fileName)
# We will bind a couple of mouse events to the reference canvas so
that
# we can identify the sample area used in the cross-correlation.
refCanvas.bind('<ButtonPress-1>', set_x0_y0_via_mouse) # anchor box
refCanvas.bind('<B1-Motion>', set_x1_y1_via_mouse) # draw box
refCanvas.bind('<ButtonRelease-1>', set_x1_y1_via_mouse) # draw
box, final
return

def openTestImage():
    """
    Interactive dialog to select the test image.
    """
    global testImage, testCanvas, testFileName
    import os
    fileName = tkFileDialog.askopenfilename()
    if fileName:
        testImage = Image.open(fileName).convert('L') # to grayscale
        print "Finished reading image from file", fileName
        testCanvas = openImageWindow(testImage, 'BOS Test\
Image-Filename: \''+os.path.basename(fileName), testCanvas)
        testFileName.set(fileName)
    return

def saveDifferenceImage():
    """
    Interactive dialog to select the test image.
    """
    global diffImage
    if diffImage:
        fileName = tkFileDialog.asksaveasfilename()
        if fileName:
            testImage = diffImage.save(fileName, 'JPEG')
    return

def openImageWindow(image, title, canvas):
    """
    Displays the supplied image on a scrolled canvas in a new top-level
    window.

    Returns a reference to the canvas.
    This allows the canvas to reused next time and it allows access to
    the
    cursor coordinates on the canvas.
    """
    if canvas == None:
        # The canvas does not yet exist.
        t = Tkinter.Toplevel()
        t.title(title)
        f = Tkinter.Frame(t, borderwidth=1)

```

```

        f.pack(expand=1, fill="both")
        # We want a large canvas that can be scrolled.
        # Since the Python Megawidgets version seems to be broken,
        # build our own with standard Tkinter widgets.
        scf = Tkinter.Frame(f)
        scf.pack(expand=1, fill="both")
        sh = Tkinter.Scrollbar(scf, orient=Tkinter.HORIZONTAL)
        sv = Tkinter.Scrollbar(scf)
        canvasWidth, canvasHeight = image.size
        # The screen view of the canvas with be fixed, smaller than the
image.
        canvas = Tkinter.Canvas(scf, width=800,height=800,
                                scrollregion=(0,0,canvasWidth,canvasHeight))
        canvas.grid(row=0, column=0, sticky="nsew")
        sv.grid(row=0, column=1, sticky="ns")
        sh.grid(row=1, column=0, sticky="ew")
        sv.config(command=canvas.yview)
        sh.config(command=canvas.xview)
        canvas.config(yscrollcommand=sv.set, xscrollcommand=sh.set)
        # Put the image onto the canvas.
        canvas.im = ImageTk.PhotoImage(image)
        # this c.im reference lasts as long as the canvas
        canvas.create_image(0, 0, image=canvas.im, anchor="nw")
        return canvas

def locateMaximum(mat):

    rowsize, colsize = mat.shape
    biggest = 0; ibig = 0; jbig = 0
    for i in range(rowsize):
        for j in range(colsize):
            if mat[i,j] > biggest:
                biggest = mat[i,j]
                ibig = i; jbig = j

    return jbig, ibig, biggest

def ind2sub(row,col,ind):
    """ Converts row,col indices into one index for .flat """
    i = ind/col
    j = ind - i* col
    return i,j

def gausspeak(cmap,start):
    from scipy.stats import tvar as var
    from scipy.stats.distributions import norm
    from scipy import cumsum,log,exp,zeros,r_,dot,transpose,array
    from scipy import linalg,nan

    # (pseudo-)Gaussian peak fit:  $p(x,y) = \exp(a + b*x + c*y + d*x*x + e*x*y + f*y*y)$ 
    global QMAT
    rhs = zeros((9), dtype=float)
    ind= 0
    for j in r_[-1:2]:
        for i in r_[-1:2]:
            rhs[ind] = log(max(cmap[start[1]+j,start[0]+i],1e-12))
            ind = ind + 1
    if var(rhs) == 0:

        #right hand side was clipped everywhere: no good
        peak= 0

```

```

    shift= array([0,0])
    ok= -1

#solve normal equations for least squares problem
qr= dot (transpose(QMAT), transpose(rhs))
coeffs= linalg.solve(QQ,qr)

#unpack solution vector; find peak position from zero derivative
mmat= array([[2*coeffs[3],coeffs[4]],[coeffs[4],2*coeffs[5]])
mrhs= array([[ -coeffs[1]],[ -coeffs[2]])
qvec= transpose(linalg.solve(mmat,mrhs)) #qvec = (mmat\mrhs)'
if norm(qvec) > 1 :
#interpolated displacement is too large: no good
    peak= 0
    shift= array([0,0])
    ok= -1
ok= 1
shift= qvec + start
qvec = transpose(qvec)
peak= exp(coeffs[0] + coeffs[1]*qvec[0] + coeffs[2]*qvec[1]\ +
coeffs[3]*qvec[0]*qvec[0]\
    + coeffs[4]*qvec[0]*qvec[1] + coeffs[5]*qvec[1]*qvec[1])
return peak,shift,ok

def slidesum(a,n,m):
    from scipy import hstack,vstack,cumsum,zeros,r_,array
    #sliding window summation; averaging window size is [n,m]
    na,ma= a.shape
    aa=
vstack(((zeros((1,ma+1), dtype=float)), (hstack(((zeros((na,1), dtype=floa
t)),a))))))
    a1= cumsum(aa,0)
    a2 = a1[n:na+1,:]-a1[0:na+1-n,:]
    a3 = cumsum(a2,1)
    ss = a3[:,m:ma+1]-a3[:,0:ma+1-m]
    return ss

def simplepiv(I1,I2,wxy,mxy,sxy):
    from scipy.stats import var
    from scipy.signal.signaltools import correlate2d
    from scipy import
shape,reshape,zeros,r_,dot,transpose,real,conj,sqrt
    from scipy.fftpack import fft2,ifft2
    global QMAT, QQ
    import numpy

#convert Image to numeric arrays
I1data = numpy.array(I1.getdata())
I2data = numpy.array(I2.getdata())
xsize ,ysize = I1.size
I1data = reshape(I1data,(ysize,xsize))
I2data = reshape(I2data,(ysize,xsize))

QMAT = numpy.array([[1,-1,-1,1,1,1],[1,0,-1,0,0,1],[1,1,-1,1,-1,1],
                    [1,-1,0,1,0,0],[1,0,0,0,0,0],[1,1,0,1,0,0],
                    [1,-1,1,1,-1,1],[1,0,1,0,0,1],[1,1,1,1,1,1]])
QQ = dot (transpose(QMAT),QMAT)

#-----
-----

if I1data.shape != I2data.shape:

```

```

    print "Images should be same size ..."
if wxy < 1:
    print "Wrong window size wxy ..."
if mxy < 1:
    print "Search range mxy too small ..."
if 2*mxy >= wxy:
    print "Search range mxy too large ..."
if sxy < 1:
    print "Wrong window spacing sxy ..."
height,width = I1data.shape
#start and end coordinates for interrogation
left= 0
right= width - wxy
top= 0
bot= height - wxy
print top, bot, left, right, sxy
# size of correlation map, always odd
CSZ= 2*mxy +1
#size of sliding template
wsz= wxy-CSZ+1

x = zeros((int((bot-top)/sxy)+1,int((right-
left)/sxy)+1),dtype=float)
y = zeros((int((bot-top)/sxy)+1,int((right-
left)/sxy)+1),dtype=float)
u = zeros((int((bot-top)/sxy)+1,int((right-
left)/sxy)+1),dtype=float)
v = zeros((int((bot-top)/sxy)+1,int((right-
left)/sxy)+1),dtype=float)
cor = zeros((int((bot-top)/sxy)+1,int((right-
left)/sxy)+1),dtype=float)
vld = zeros((int((bot-top)/sxy)+1,int((right-
left)/sxy)+1),dtype=float)

nx= -1
for xoff in r_[left:right+1:sxy]:
    nx = nx +1
    ny = -1
    for yoff in r_[top:bot+1:sxy]:
        ny = ny + 1

A= I1data[yoff+mxy:yoff-mxy+wxy,xoff+mxy:xoff-mxy+wxy]
B= I2data[yoff:yoff+wxy,xoff:xoff+wxy]
sumA= sum(sum(A))
varA= var(A,axis=None)*(wsz*wsz-1)
sumB= slidesum(B,wsz,wsz)
varB= slidesum(B**2,wsz,wsz)-(sumB**2)/(wsz*wsz)

#compute covariance for windows
fft_A= fft2(A,shape=(wxy,wxy))
fft_B= fft2(B,shape=(wxy,wxy))
corrAB= real(iff2(conj(fft_A)*fft_B))
covAB = corrAB[0:CSZ,0:CSZ] - (sumB*sumA)/(wsz*wsz)
#compute normalized cross correlation coefficient
cmap= covAB/sqrt(varA*varB)
xpeak, ypeak, corrbig = locateMaximum(cmap)
#compute pattern shift based on correlation peak position
utemp= xpeak - mxy
vtemp= ypeak - mxy
#check for "edge peak": no sub-pixel interpolation possible
(or fast processing)

```

```

        if xpeak == 0 or xpeak == CSZ-1 or ypeak==0 or ypeak ==
        CSZ-1:
            valid= 0
        else :

            #subpixel interpolation
            peak,shift,ok = gausspeak(cmap,[xpeak,ypeak])

            if ok != 1 or peak/corrbig < 0.98 or peak/corrbig >
2.0:
                valid= 0
            else:
                valid= 1
                corrbig = peak[0]
                utemp= shift[0,0] - mxy
                vtemp= shift[0,1] - mxy

                #compute pattern shift based on correlation peak position
                x[ny,nx]= xoff + wxy/2 - 0.5
                y[ny,nx]= yoff + wxy/2 - 0.5
                u[ny,nx]= utemp
                v[ny,nx]= vtemp
                cor[ny,nx]= corrbig
                vld[ny,nx]= valid
            return x,y,u,v,cor,vld

def estimateCoarseShift():
    from scipy import floor
    global testImage, refImage, xshiftVar, yshiftVar
    global sampleBoxVar
    text = sampleBoxVar.get()
    x0, y0, x1, y1 = text.split()
    sampleBox = tuple([int(x0), int(y0), int(x1), int(y1)])
    print "sampleBox=", sampleBox
    refSmallImage = refImage.crop(sampleBox).convert('L')
    testSmallImage = testImage.crop(sampleBox).convert('L')
    # refSmallImage.show(); testSmallImage.show()
    xsize, ysize = refSmallImage.size
    # Convert to Numeric arrays and do cross correlation.
    refData = Numeric.array(refSmallImage.getdata())
    refData.shape = refSmallImage.size
    testData = Numeric.array(testSmallImage.getdata())
    testData.shape = testSmallImage.size
    try:
        # Requires Scipy.
        corrData = correlate2d(refData,testData)
        # print "corrData=", corrData
        ibig, jbig, corrbig = locateMaximum(corrData)
        # Might it be better to shift by a fraction of a pixel?
        # This is possible by doing bilinear interpolation, say.
        print "Max correlation=", corrbig, " at i=", ibig, "j=", jbig
        xshift, yshift = xsize - 1 - ibig, ysize - 1 - jbig
        # xshift, yshift = ibig - xsize/2 + 1, jbig - ysize/2 + 1
    except:
        xshift, yshift = 0, 0
    xshiftVar.set(xshift); yshiftVar.set(yshift)
    return

def shiftTestImage():
    global testImage, testCanvas
    xsize, ysize = testImage.size
    xshift = int(xshiftVar.get())

```

```

yshift = int(yshiftVar.get())
shiftedImage = testImage.crop((xshift, yshift, xsize, ysize))
testCanvas.im = ImageTk.PhotoImage(shiftedImage)
testCanvas.create_image(0, 0, image=testCanvas.im, anchor="nw")
testImage = shiftedImage
print "After shifting, new testImage size:", testImage.size
return

def showImageDifference():
    global testImage, refImage, diffImage, diffCanvas, croppedRefImage
    xsize, ysize = testImage.size
    croppedRefImage = refImage.crop((0, 0, xsize, ysize))
    diffImage = ImageChops.difference(testImage, croppedRefImage)
    diffCanvas = openImageWindow(diffImage, 'BOS Difference',
diffCanvas)
    return

def showVectorDisplacements():

    global testImage, croppedRefImage, u,
v, valid, q1, umean, vmean, x, y, sxyVar, \
    wxyVar, goodvectorsVar
    from scipy import where, compress, logical_and, median, logical_or, nan
    from pylab import
resize, transpose, quiver, title, show, find, imshow, hist, \
    figure, clf, draw, save, load, xlabel, ylabel, flipud

    mxy = 3
    wxy = int(wxyVar.get())
    sxy = int(sxyVar.get())
    goodvectors = float(goodvectorsVar.get())
    #process to find PIV-style displacements
    x, y, u, v, q1, valid = simplepiv(croppedRefImage, testImage, wxy, mxy, sxy)
    good = where(logical_and(q1 > goodvectors, valid > 0), True, False)
    umean= median(compress(good.flat, u.flat))
    vmean= median(compress(good.flat, v.flat))
    u = where(logical_or(q1 < goodvectors, valid < 0), 0, u)
    v = where(logical_or(q1 < goodvectors, valid < 0), 0, v)
    u = u-umean
    v = v-vmean
    save('vecx.out', x)
    save('vecy.out', y)
    save('vecu.out', u)
    save('vecv.out', v)
    save('vecq1.out', q1)
    save('vecvalid.out', valid)
    u = flipud(u)
    v = -flipud(v)
    quiver (x, y, u, v)
    title ('Vector displacements')
    xlabel ('Pixels')
    ylabel ('Pixels')
    show()
    return

def histogram_u_v():

    from pylab import figure, hist, title, load, xlabel, ylabel
    from scipy import where, logical_or, flipud

    u = load('vecu.out')
    v = load('vecv.out')
    u = flipud(u)

```

```

v = -flipud(v)
figure()
hist(u,100)
title ('Frequency Distribution of horizontal displacements data')
xlabel('Horizontal Displacement in Pixels')
ylabel('Frequency')
figure()
hist(v,100)
title ('Frequency Distribution of vertical displacements data')
xlabel('Vertical Displacement in Pixels')
ylabel('Frequency')

def showContours_u():

    global
    q1,valid,umean,vmean,upperLevelVar,lowerLevelVar,numcontourVar,\
        goodvectorsVar,modelgreylevelVar,lowerLevel,upperLevel,\
        numcontour,tick
    from scipy import zeros,where,logical_or,argmin,shape,ravel,nan,\
        compress,r_,flipud
    from pylab import
    imshow,clf,title,save,load,figure,contourf,cm,hold,\
        contour,xlabel,ylabel

    x = load('vecx.out')
    y = load('vecy.out')
    u = load('vecu.out')
    q1= load('vecq1.out')
    valid=load('vecvalid.out')
    modelgreylevel = float(modelgreylevelVar.get())
    goodvectors = float(goodvectorsVar.get())
    u = where(logical_or(q1 < goodvectors,valid < 0),modelgreylevel,u)
    u = flipud(u)
    lowerLevel = float(lowerLevelVar.get())
    upperLevel = float(upperLevelVar.get())
    numcontour = int(numcontourVar.get())
    tick = float(upperLevel-lowerLevel)/numcontour
    uu=r_[lowerLevel:upperLevel:tick]
    figure()
    contourf(x,y,u,uu,cmap=cm.gray)
    contourf(x,y,u,uu,cmap=cm.gray)
    xlabel('Pixels')
    ylabel('Pixels')
    return

def showContours_v():

    global umean,vmean,modelgreylevelvar,goodvectorsVar,lowerLevelVar,\
        upperLevelVar,tickvar,numcontourVar
    from scipy import
    zeros,where,logical_or,r_,argmin,shape,ravel,nan,\
        compress,flipud
    from pylab import
    imshow,clf,title,save,load,figure,contourf,cm,hold,\
        contour,xlabel,ylabel

    x = load('vecx.out')
    y = load('vecy.out')
    u = load('vecu.out')
    v = load('vecv.out')
    q1= load('vecq1.out')
    valid=load('vecvalid.out')
    modelgreylevel = float(modelgreylevelVar.get())

```

```

goodvectors = float(goodvectorsVar.get())
v = where(logical_or(q1 < goodvectors, valid < 0), modelgreylevel, v)
v = -flipud(v)
lowerLevel = float(lowerLevelVar.get())
upperLevel = float(upperLevelVar.get())
numcontour = int(numcontourVar.get())
tick = float(upperLevel-lowerLevel)/numcontour
vv=r_[lowerLevel:upperLevel:tick]
figure()
contourf(x, y, v, vv, cmap=cm.gray)
contourf(x, y, v, vv, cmap=cm.gray)
xlabel('Pixels')
ylabel('Pixels')
return

def showColourSchlieren():

    global colourlevelVar
    from scipy import arctan2, shape, r_, pi, sqrt, zeros, shape
    from pylab import contourf, quiver, load, figure, show, imshow
    from colorsys import hsv_to_rgb

    x = load('vecx.out')
    y = load('vecy.out')
    u = load('vecu.out')
    v = load('vecv.out')

    angle=arctan2(v,u)
    colourlevel = float(colourlevelVar.get())
    #convert angle to go from 0 to 2*pi.
    height, width = x.shape
    for i in r_[0:height-1]:
        for j in r_[0:width-1]:
            if angle[i,j]<0:
                angle[i,j]=2*pi+angle[i,j]

    magnitude=sqrt(u**2+v**2)
    max_magnitude= magnitude.max()

    C = zeros((int(height),int(width),int(3)),dtype=float)
    for i in r_[0:height-1]:
        for j in r_[1:width-1]:
            h=angle[i,j]/2/pi
            s=colourlevel*magnitude[i,j]/max_magnitude
            if s>1:
                s=1
            vv=1
            h,s ,vv = hsv_to_rgb(h,s,vv)
            C[i,j,0]=h
            C[i,j,1]=s
            C[i,j,2]=vv

    figure()
    imshow(C)
    show()
    return

#-----
if __name__ == '__main__':
    main()

```

makerounddotmask.m Code

```

% Professor Thomas Rösger, 2005

function makerounddotmask1 (patternsize, dotsize)
% patternsize: diameter of (round) pattern in [mm]
% dotsize: size of dots in [mm]

ngrid= round(patternsize/dotsize)
mask= uint8(zeros(ngrid,ngrid));
n= 0;
nold= -1;
k= 0;
while k < 100 & n > nold
    nold= n;
    k= k + 1;
    disp(k);
    for l=1:ngrid
        xy= rand(2,ngrid);
        xyint= round(xy*(ngrid-1))+1;
        pxy(2,n+ngrid)= NaN;
        for m=1:ngrid
            if mask(xyint(2,m),xyint(1,m)) == 0
                xt= min(max(xyint(1,m)+(-1:1:1),1),ngrid);
                yt= min(max(xyint(2,m)+(-1:1:1),1),ngrid);
                mask(yt,xt)= 1;
                n= n + 1;
                pxy(:,n)= xy(:,m);
            end
        end
    end
    disp (n);
end
figure (1);
pxy= pxy * patternsize;
ptsize= dotsize / 25.4 * 72;
plot(pxy(1,:),pxy(2:,:), 'ok', 'Markersize',ptsize, 'MarkerEdgeColor','k', '
MarkerFaceColor','k');
hold on;
for i=1:100
    xc(i)= patternsize/2 + patternsize/2*cos(2*pi*(i-1)/99);
    yc(i)= patternsize/2 + patternsize/2*sin(2*pi*(i-1)/99);
end
plot(xc,yc, 'k', 'Linewidth',0.75);
% for i=1:100
%     xc(i)= patternsize/2 + 85*cos(2*pi*(i-1)/99);
%     yc(i)= patternsize/2 + 85*sin(2*pi*(i-1)/99);
% end
% plot(xc,yc, 'k', 'Linewidth',0.75);
set(gca, 'Position', [0,0,1,1]);
axis square;

```

```
axis off;
% for i=1:ngrid
%     plot([i,i]*patternsize/ngrid,[1,ngrid]*patternsize/ngrid,'g');
%     plot([1,ngrid]*patternsize/ngrid,[i,i]*patternsize/ngrid,'b');
% end
hold off;
```